

Electronic Thesis and Dissertation Repository

10-18-2022 2:00 PM

In Vitro and In Vivo Characterization of the Metallodrug BOLD-100 as an Inhibitor of SARS-CoV-2 Replication

Daniel S. Labach, *The University of Western Ontario*

Supervisor: Barr, Stephen D., *The University of Western Ontario*

A thesis submitted in partial fulfillment of the requirements for the Master of Science degree in Microbiology and Immunology

© Daniel S. Labach 2022

Follow this and additional works at: <https://ir.lib.uwo.ca/etd>



Part of the [Virus Diseases Commons](#)

Recommended Citation

Labach, Daniel S., "In Vitro and In Vivo Characterization of the Metallodrug BOLD-100 as an Inhibitor of SARS-CoV-2 Replication" (2022). *Electronic Thesis and Dissertation Repository*. 8940.
<https://ir.lib.uwo.ca/etd/8940>

This Dissertation/Thesis is brought to you for free and open access by Scholarship@Western. It has been accepted for inclusion in Electronic Thesis and Dissertation Repository by an authorized administrator of Scholarship@Western. For more information, please contact wlsadmin@uwo.ca.

Abstract

The COVID-19 pandemic, caused by severe acute respiratory syndrome coronavirus 2 (SARS-CoV-2), has caused extensive mortality and societal disruption. BOLD-100 is a novel anticancer therapeutic being considered to treat COVID-19. We hypothesized that BOLD-100 inhibits SARS-CoV-2 replication and progression of COVID-19. Using Western blotting, quantitative RT-PCR, and cell viability assays, we determined that BOLD-100 inhibits SARS-CoV-2 replication *in vitro*. RNA sequencing analysis demonstrated that BOLD-100 inhibits virus-induced transcriptional changes in infected cells. Intravenous BOLD-100 treatment of SARS-CoV-2-infected hamsters did not significantly alter body weight, lung viral load or pathological lesions. Finally, we showed that the antiviral activity of BOLD-100 is not specific for SARS-CoV-2 and can also inhibit replication of Human Immunodeficiency Virus type 1 and Human Adenovirus type 5. This study identifies BOLD-100 as a novel antiviral agent and will inform its future preclinical development.

Keywords

SARS-CoV-2, COVID-19, BOLD-100, drug, animal model, hamster model, antiviral

Summary for Lay Audience

The COVID-19 pandemic has caused widespread illness and mortality worldwide, and threatens many more lives in the months to come. There is an urgent need to discover and test new treatments to treat patients with COVID-19. BOLD-100 is a promising new drug that was originally developed as an anticancer therapeutic, but has been shown to potently inhibit SARS-CoV-2 (the virus that causes COVID-19) in initial experiments.

In this study, we first characterized the antiviral potential of BOLD-100 against SARS-CoV-2 by measuring its ability to stop the virus from reproducing and killing infected cells. Subsequently, we determined that BOLD-100 inhibits changes in cellular gene expression that occur upon infection with SARS-CoV-2. We then established a Syrian hamster model of SARS-CoV-2 infection to test the therapeutic impact of BOLD-100 on COVID-19 in live animals. We determined the maximum tolerated dose of BOLD-100 in hamsters, in addition to the appropriate dosage of SARS-CoV-2 for infection. BOLD-100 treatment in SARS-CoV-2 infected hamsters did not significantly reduce virus replication or tissue damage in the lungs. However, further refinements to our hamster model are possible to maximize the effect of BOLD-100. Finally, we demonstrated that the antiviral activity of BOLD-100 is not specific for SARS-CoV-2, and that it additionally inhibits the replication of Human Immunodeficiency Virus 1 and Human Adenovirus type 5. In conclusion, we identified BOLD-100 as a novel antiviral therapeutic with antiviral activity against SARS-CoV-2 and additional viruses of public health concern, but with limited activity in a hamster model of COVID-19. This information will support the further development of BOLD-100, and inform future preclinical studies. Identification of new antiviral drugs will provide additional treatment options for vulnerable patients and may alleviate the burden of future pandemics.

Co-Authorship Statement

The studies and analyses described herein were performed by Daniel Labach, with the following exceptions:

The cytopathic effect protection assays described in Figure 5 were performed by Dr. Stephen Barr.

Illumina Next Gen sequencing and Gene Set Enrichment analysis was performed by David Carter (London Regional Genomics Centre).

Animal handling, drug treatment, and infections in live hamsters were performed by Heather Cadieux-Pitre, Kim Thomaes, and Nicole Hague. Embedding, sectioning and staining of hamster tissue was performed by Caroline O'Neil. All histopathological images and analyses were generated by Dr. Patti Kiser (Western University).

Acknowledgments

Firstly, I would like to thank my supervisor Dr. Stephen Barr for his guidance, support, and unfailingly calm demeanor throughout the highs and lows of my time as an undergraduate and graduate student in his lab. I am especially grateful to Steve for giving me the opportunity to work in the BSL-3 laboratory and the countless hours he spent in there to train me. I would also like to thank my advisory committee members Dr. Eric Arts and Dr. Ryan Troyer for their constructive comments and support over the course of my project.

I am greatly appreciative of Bold Therapeutics, Inc. and Mitacs for generously providing me with an Accelerate fellowship to support this research. A special thanks to Dr. Mark Bazett and Jim Pankovich from Bold Therapeutics for lending me their expertise and providing me with opportunities to learn more about their organization and the broader pharmaceutical industry.

I am grateful for the assistance provided by members of the Barr Lab in performing experiments and teaching me lab techniques, especially Ermela Papparisto, Dr. Pascaline Kohio, and Nicole Friesen. Additionally, I would like to thank Edwin Tse for his help in generating figures for RNA Sequencing analysis. I am likewise thankful for the technical expertise of David Carter and Dr. Patti Kiser, who performed RNA Sequencing and histopathological analysis respectively in this study.

A massive thank you to all the colleagues, especially those in the ImPaKT laboratory, who lent their time to assist me in my work and resolve emergencies. While there are too many to list, I would like to particularly thank Rick Gibson, Heather Cadieux-Pitre, Dr. Mariya Goncheva, Dr. Kate Parham, Yiyang Zhang, and Janice Kim.

I would like to acknowledge the financial support I received from the Canadian Institutes of Health Research through a Canada Graduate Scholarship-Masters as well as from the Department of Microbiology and Immunology at Western University through a RGE Murray Graduate Scholarship.

Finally, I am immensely grateful for the endless support I have received from family and friends, without whom this work would not have been possible.

Table of Contents

Abstract.....	ii
Summary for Lay Audience.....	iii
Co-Authorship Statement.....	iv
Acknowledgments.....	v
Table of Contents.....	vi
List of Tables.....	x
List of Figures.....	xi
List of Appendices.....	xiii
List of Abbreviations.....	xiv
1 Chapter 1: Introduction.....	1
1.1 Severe Acute Respiratory Syndrome Coronavirus 2 (SARS-CoV-2).....	1
1.1.1 Introduction & Structure.....	1
1.1.2 Genome.....	2
1.1.3 Replication Cycle.....	3
1.1.4 Variants of Concern.....	7
1.2 Coronavirus Disease 2019 (COVID-19).....	8
1.2.1 Symptoms & Transmission.....	8
1.2.2 Host Transcriptional Response.....	9
1.3 Animal Models of COVID-19.....	11
1.3.1 Mice.....	12
1.3.2 Syrian Hamsters.....	12
1.3.3 Ferrets.....	14
1.3.4 Non-Human Primates.....	14
1.4 Therapeutics for COVID-19.....	14

1.4.1	Nucleoside Analogues	14
1.4.2	Protease Inhibitors	15
1.4.3	Monoclonal Antibodies.....	16
1.5	BOLD-100	16
1.5.1	Ruthenium-based Drugs.....	17
1.5.2	Overview of BOLD-100	17
1.5.3	Properties of BOLD-100.....	18
1.5.4	Clinical Development of BOLD-100.....	19
1.5.5	Mechanistic Targets of BOLD-100	19
1.6	Rationale, Hypothesis, and Objectives	22
2	Chapter 2: Materials and Methods	24
2.1	Cell Culture.....	24
2.2	Viruses	24
2.3	Virus Propagation	25
2.3.1	SARS-CoV-2	25
2.3.2	HIV-1 AD.MDR01	25
2.3.3	HAdV-C5.....	26
2.4	BOLD-100 Preparation.....	26
2.5	SARS-CoV-2 Infections	27
2.6	Microscopy and Image Acquisition.....	27
2.7	Cell Viability Assays	27
2.7.1	CellTiter-Glo.....	27
2.7.2	Cell Counting Kit-8.....	28
2.8	Antibodies and Western Blotting.....	28
2.8.1	Primary Antibodies	28
2.8.2	Secondary Antibodies	28

2.8.3	Western Blotting	28
2.9	RNA Extraction and Quantitative RT-PCR.....	29
2.10	RNA Sequencing	30
2.11	<i>In Vivo</i> Experiments.....	31
2.11.1	Ethics Statement.....	31
2.11.2	Hamster Maintenance	31
2.11.3	BOLD-100 Dose Escalation	31
2.11.4	SARS-CoV-2 Infections and Organ Collection.....	31
2.11.5	SARS-CoV-2 Plaque Assays	32
2.11.6	Histopathological Analysis	32
2.12	HIV-1 Infections and Infectivity Assay	32
2.13	HAdV-C5 Infections and Plaque Assay	33
2.14	Statistical Analysis.....	33
3	Chapter 3: Results	35
3.1	BOLD-100 Inhibits SARS-CoV-2-induced Cytopathic Effects.....	35
3.2	BOLD-100 Cytotoxicity in 293T-ACE2 Cells	38
3.3	BOLD-100 Exhibits Dose-Dependent Inhibition of SARS-CoV-2.....	40
3.4	BOLD-100 Inhibits SARS-CoV-2 Variants of Concern	43
3.5	BOLD-100 Inhibits Changes in the Host Transcriptome Induced by SARS-CoV-2	46
3.6	Determining the Maximum Tolerated Dose of BOLD-100 in Syrian Hamsters ..	55
3.7	Establishment of a Syrian Hamster Model of COVID-19	57
3.8	Determining the Ability of BOLD-100 to Inhibit COVID-19 Progression in a Syrian Hamster Model	60
3.9	Antiviral Activity of BOLD-100 in Additional Viral Infection Models.....	67
3.9.1	BOLD-100 Inhibits HIV-1 Replication	67
3.9.2	BOLD-100 Inhibits HAdV-C5 Replication	73

4 Chapter 4: Discussion	76
References	87
Appendix A	101
Appendix B	106
Curriculum Vitae – Daniel Labach	107

List of Tables

Table 1: IC ₅₀ , CC ₅₀ , and SI values for BOLD-100 against SARS-CoV-2 variants of concern.	43
Table 2: Histopathological features detected in the lungs of Syrian hamsters infected with SARS-CoV-2 in the presence and absence of BOLD-100 treatment.	64

List of Figures

Figure 1: Structure of the SARS-CoV-2 virion and layout of the SARS-CoV-2 genome	3
Figure 2: The SARS-CoV-2 replication cycle.	6
Figure 3: Schematic of antiviral innate immune pathways that activate IFN- β transcription.	11
Figure 4: Chemical structure of BOLD-100 (sodium <i>trans</i> -[tetrachlorobis(1H-indazole)ruthenate(III)]dihydrate).	18
Figure 5: BOLD-100 inhibits SARS-CoV-2-induced cytopathic effects.	37
Figure 6: BOLD-100 cytotoxicity in 293T-ACE2 cells.	39
Figure 7: BOLD-100 inhibits intracellular accumulation of SARS-CoV-2 N protein and RNA.	42
Figure 8: BOLD-100 inhibits SARS-CoV-2 variants of concern.	45
Figure 9: Proportion of SARS-CoV-2-aligned reads following SARS-CoV-2 infection and BOLD-100 treatment.	47
Figure 10: Transcriptional profile of 293T-ACE2 cells following BOLD-100 treatment and/or SARS-CoV-2 infection.	51
Figure 11: Dotplot visualization of enriched GO terms following SARS-CoV-2 infection and/or BOLD-100 treatment in 293T-ACE2 cells.	52
Figure 12: Heat maps of differentially expressed genes following SARS-CoV-2 infection and/or BOLD-100 treatment in 293T-ACE2 cells. s.	54
Figure 13: Normal expected renal features compared to abnormal kidney, cortex, H&E 40x objective.	56
Figure 14: Establishment of a Syrian hamster model of COVID-19. s.	58

Figure 15: Viral load in lungs and trachea in hamsters treated with BOLD-100 and infected with SARS-CoV-2.	62
Figure 16: Change in weight in hamsters treated with BOLD-100 and infected with SARS-CoV-2.....	63
Figure 17: Representative lung sections from hamsters infected with SARS-CoV-2, H&E, 40x objective.	66
Figure 18: BOLD-100 inhibits production of HIV-1 viral particles in a dose-dependent manner.....	70
Figure 19: BOLD-100 inhibits replication of infectious HIV-1 in a dose-dependent manner.	72
Figure 20: Inhibition of infectious HAdV-C5 by BOLD-100..	75

List of Appendices

Appendix A: Top 30 most upregulated and downregulated genes for each treatment group in RNA Sequencing analysis.....	101
Appendix B: Copyright permissions for Figs. 1–3.	106

List of Abbreviations

α	alpha
β	beta
$^{\circ}\text{C}$	degrees Celsius
$\times g$	times gravity
μM	micromolar
μm	micrometre
ACE2	angiotensin-converting enzyme 2
ANOVA	analysis of variance
ATP	adenosine triphosphate
BOLD-100	sodium trans-[tetrachlorobis(1H-indazole)ruthenate(III)]
CBS	citrate-buffered saline
CC ₅₀	50% cytotoxic concentration
CCK8	Cell Counting Kit-8
CO ₂	carbon dioxide
COVID-19	Coronavirus disease 2019
CPE	cytopathic effects
DMEM	Dulbecco's Modified Eagle Medium
DMSO	dimethylsulfoxide
DNA	deoxyribonucleic acid
dsDNA	double-stranded DNA
E	envelope
ER	endoplasmic reticulum
FBS	fetal bovine serum
GO	Gene Ontology
GRP78	78 kDa glucose-regulated protein
h	hour
H&E	hematoxylin and eosin
HAdV-C5	human adenovirus type 5
HIV-1	Human Immunodeficiency virus 1
h.p.i	hours post-infection
HSA	human serum albumin
IC ₅₀	50% inhibitory concentration
IFN	interferon
i.n.	intranasal
i.v.	intravenous
IRF	interferon regulatory factor
kb	kilobase
kDa	kilodalton
kg	kilogram
KP1019	(indazole trans-[tetrachlorobis(1H-indazole)ruthenate(III)]
M	membrane
mAb	monoclonal antibody
mg	milligram
MOI	multiplicity of infection

M ^{pro}	main protease
mRNA	messenger RNA
MTD	maximum tolerated dose
N	nucleocapsid
NF-κB	nuclear factor kappa B
NHP	non-human primate
nm	nanometre
nM	nanomolar
NOAEL	no observed adverse effect level
nsp	nonstructural protein
ORF	open reading frame
PAGE	polyacrylamide gel electrophoresis
PAMP	pathogen-associated molecular pattern
PCR	polymerase chain reaction
PBS	phosphate-buffered saline
PBS-T	PBS with 10% Tween
PFU	plaque forming units
p.i.	post-infection
PL ^{pro}	papain-like protease
PVDF	polyvinylidene difluoride
RBD	receptor-binding domain
RdRp	RNA-dependent RNA polymerase
RLU	relative light units
RNA	ribonucleic acid
RNASeq	RNA Sequencing
ROS	reactive oxygen species
rRNA	ribosomal RNA
RTC	replication-transcription complex
RT-qPCR	quantitative real-time PCR
Ru	ruthenium
S	spike
SARS-CoV-2	Severe acute respiratory syndrome coronavirus 2
SD	standard deviation
SDS	sodium dodecyl sulfate
SEM	standard error of the mean
SI	selectivity index
TCID ₅₀	50% tissue culture infectious dose
TRS	transcription regulatory sequence
TRS-L	TRS in the 5' leader sequence
U	unit
UPR	unfolded protein response
UTR	untranslated region

1 Chapter 1: Introduction

In December 2019, an outbreak of viral pneumonia emerged in southern China and rapidly spread worldwide¹. The etiological agent of this disease was subsequently identified as a novel betacoronavirus with probable zoonotic origins. In February 2020, the novel virus was officially named “Severe acute respiratory syndrome coronavirus 2” (SARS-CoV-2), while its associated disease was designated “Coronavirus disease 2019 (COVID-19)”². Since the emergence of SARS-CoV-2, the COVID-19 pandemic has caused a staggering amount of mortality and morbidity worldwide, and continues to threaten more lives in the months to come.

1.1 Severe Acute Respiratory Syndrome Coronavirus 2 (SARS-CoV-2)

1.1.1 Introduction & Structure

SARS-CoV-2, the causative agent of COVID-19, is an enveloped RNA virus from the family *Coronaviridae* in the order *Nidovirales*³. This virus shares approximately 79% sequence homology with SARS-CoV and 50% with MERS-CoV, two related pathogenic betacoronaviruses that have caused outbreaks over the past 20 years, albeit on a much smaller scale⁴. Several other human coronaviruses (229E, NL62, OC43, and HLU1) are commonly responsible for mild seasonal respiratory disease⁵, but are more distantly related to SARS-CoV-2. Coronavirus virions exhibit a spherical morphology recognizable by club-shaped spike protein projections that extend from the envelope surface. Within the lipid envelope, the viral genome is packaged inside a helical nucleocapsid. The virion is composed of 4 main structural proteins: spike (S), nucleocapsid (N), envelope (E), and membrane (M) (Fig. 1A). The homotrimeric S protein, which is cleaved by host proteases into two subunits (S1 and S2), mediates recognition and binding of host cell surface receptors to initiate viral entry⁶. For this reason, the S protein is the major determinant of species and tissue tropism for coronaviruses⁵. The N phosphoprotein is the major constituent of the helical nucleocapsid and binds the RNA genome to form a ribonucleoprotein complex. The M protein is the

major structural protein that dictates virion shape, while the E protein is a minor structural protein with low levels of sequence conservation⁵.

1.1.2 Genome

SARS-CoV-2 possesses a linear, single-stranded positive sense RNA genome which spans approximately 30 kB in length (Fig. 1B). The genome contains 14 open reading frames (ORFs) which encode a total of 27 proteins⁷. Like other coronaviruses, the SARS-CoV-2 genome is flanked by untranslated regions (UTRs) at both the 5' and 3' ends. It is non-segmented and contains a 5' cap structure in addition to a 3' poly-A tail, allowing the genomic RNA to be used directly as a template for translation⁸. Adjacent to the 5'UTR are ORF1a and ORF1b, the two largest genes. These genes, which are together termed the “replicase gene”, are partially overlapping and separated by a –1 frameshift. When translated, these genes generate two polyproteins, designated pp1a and pp1ab, that are cleaved by the virally-encoded papain-like protease (PL^{pro}) and main protease (M^{pro}) to produce 16 nonstructural proteins (nsps) with diverse roles³. Specifically, nsps 2-16 comprise the viral replicase-transcriptase complex (RTC). Broadly speaking, the RTC encompasses both enzymes directly involved in the genome replication process—such as the RNA-dependent RNA polymerase (RdRp), helicase, ribonucleases and enzymes that facilitate capping and processing of the nascent RNA—as well as various cofactors for these processes and proteins with additional functions, including evasion of the host immune system, RNA proofreading, polyprotein processing, and generation of the replication niche within infected cells^{3,8,9}. The 3' proximal end of the genome encodes the four structural genes in addition to an array of accessory genes¹⁰⁻¹². The accessory genes are not strictly required for replication, but many play likely roles in pathogenesis and suppression of host immune defences. For instance, ORF6 blocks the nuclear translocation of STAT1 to inhibit interferon signaling¹³, while ORF7a antagonizes the host restriction factor SERINC5 by blocking its incorporation into newly assembled virions¹⁴. Though concrete functions have not been elucidated for all accessory proteins, ORF3a, ORF3b, ORF8, and ORF9c have also been experimentally shown to antagonize the host antiviral response^{11,12}. Like other coronaviruses, SARS-CoV-2 possesses a proofreading mechanism which improves replication fidelity compared to RNA viruses

lacking this ability. The proofreading 3' to 5' exonuclease (ExoN; nsp14) is able to excise nucleotides to correct mutations and plays an important role in ensuring the stability of the large viral genome^{8,9}.

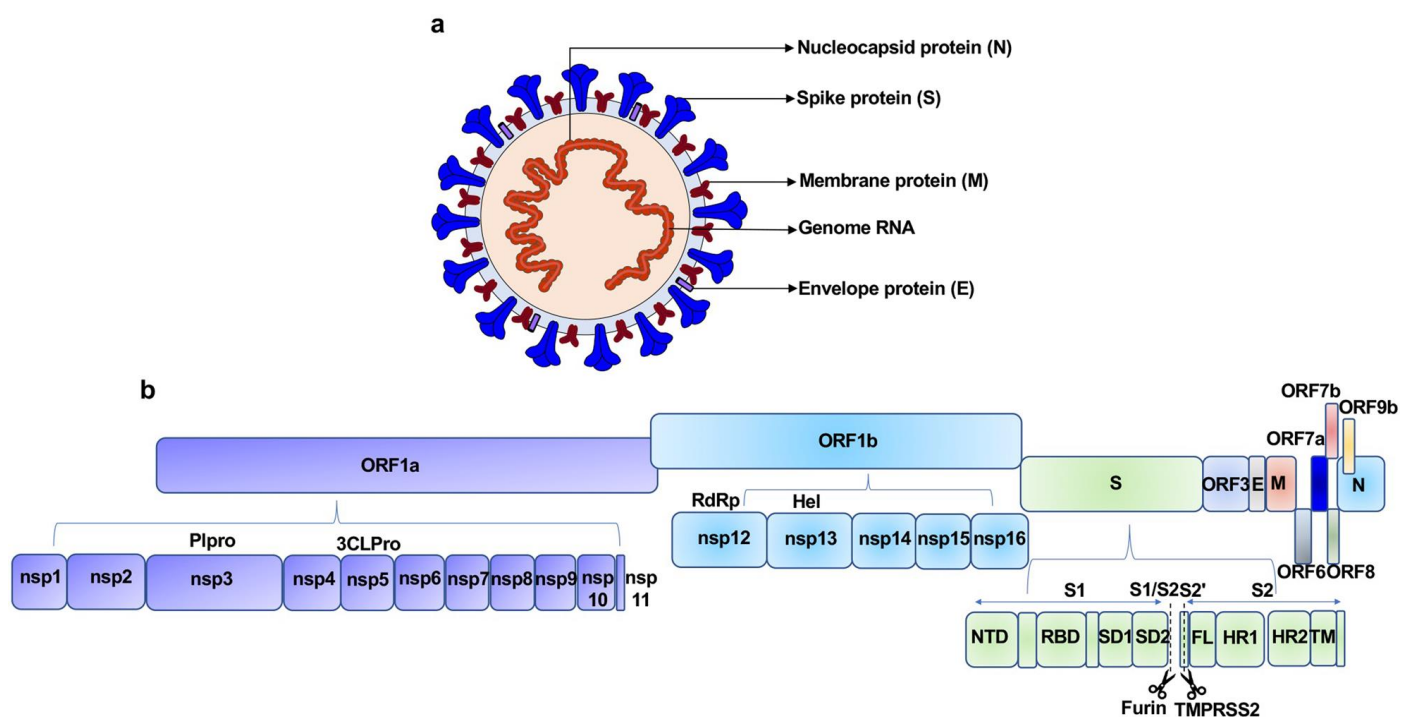


Figure 1: (A) Structure of the SARS-CoV-2 virion. (B) Layout of the SARS-CoV-2 genome. The positive-sense single-stranded RNA genome is shown in 5' to 3' orientation. ORF, open reading frame. nsp, nonstructural protein. Image retrieved from Zhang et al. (2021). *Signal Transduction and Targeted Therapy*. 6:233¹⁵.

1.1.3 Replication Cycle

SARS-CoV-2 infection is initiated by binding of viral S protein to the host receptor angiotensin-converting enzyme 2 (ACE2)⁸. Each monomer of this protein contains 2 domains—the surface-exposed S1 domain, which contains the receptor-binding domain (RBD), engages ACE2 while the S2 domain facilitates fusion of viral and cellular membranes^{8,16}. In order to interact with ACE2, the S protein must first be cleaved at the S1/S2 interface by cellular proteases. When S1 binds the ACE2 receptor, an additional cleavage site in S2 becomes exposed directly upstream of the fusion peptide; cleavage by the transmembrane serine protease TMPRSS2 at this site permits the fusion peptide to

insert into the host cell membrane to mediate fusion¹⁷. Membrane fusion can also take place at endosomal membranes, which is facilitated by cellular cathepsin proteases¹⁷. The SARS-CoV-2 S protein contains a polybasic cleavage site (PRRAR), which enables cleavage at the S1/S2 junction by the cellular protease furin during virion production^{8,18}. While this site is absent in SARS-CoV-1, equivalents are found in MERS and other pathogenic human coronaviruses¹⁹. Pre-priming of the S protein by furin-like proteases during virion production facilitates cleavage of S2 by TMPRSS2 upon attachment, thus promoting entry at the cell membrane and permitting the virus to avoid endosomal antiviral defences^{17,20}. Accordingly, though not strictly required for replication, the furin cleavage site enhances SARS-CoV-2 replication in animal models and improves entry into lung cells^{18,20–22}.

Following membrane fusion, the viral genome is released into the cytoplasm. The genomic RNA is used directly as a template for translation of the replicase gene by cytosolic ribosomes^{8,9}. The polyproteins pp1a and pp1ab are cleaved by viral proteases, liberating nsps to initiate the replication process and impair host defences^{8,9}. At this stage, nsp1—which does not form part of the RTC—acts to reduce translation of host genes to impede the production of immune factors and increase capacity for translation of viral genes. Nsp1 directly binds ribosomes, thereby blocking the channel for mRNAs to enter and undergo translation^{23–25}. Viral mRNAs are protected from nsp1 by the presence of an RNA hairpin loop structure in the leader sequence at the 5'UTR, which removes the block on the mRNA entry channel upon interaction with nsp1^{23–25}.

Notably, over the course of the viral life cycle, double-membrane organelles or “replication factories” are formed inside the host cytoplasm through the interactions of viral nsps with host membranes. These ER-derived compartments provide a protective environment for replication of genomic and subgenomic RNAs and provide an anchoring point for the RTC^{8,9}. Within this niche, viral replication intermediates are shielded from recognition by cellular immune defences^{8,9}.

For replication of the viral genome, full-length negative-sense RNA copies are first continuously synthesized by the RdRp within the RTC. These RNAs are used as

templates for the generation of new positive-sense genomes, which may be translated or incorporated into assembling virions^{8,9}. Transcription of the 3'-proximal genes encoding structural and accessory proteins proceeds by a discontinuous viral transcription process common to all coronaviruses. ORFs in this section of the genome are preceded by transcription regulatory sequences (TRS). When the RTC encounters a TRS during the synthesis of negative-sense RNA, transcription halts and is restarted at the leader section (TRS-L) located at the 5' end of the genome. Subsequently, complementary base pairing between the TRS-L and the TRS upstream of each ORF permits synthesis of the nascent negative-sense RNA to continue. The resulting RNAs are used as templates to generate a nested set of 8 positive-sense subgenomic RNAs^{8,9}.

Newly translated structural proteins assemble at the ER-to Golgi compartment and interact with viral genomic RNA to initiate the budding process. Mature virions are then released from the host cell by exocytosis and may infect other susceptible cells⁸ (Fig. 2).

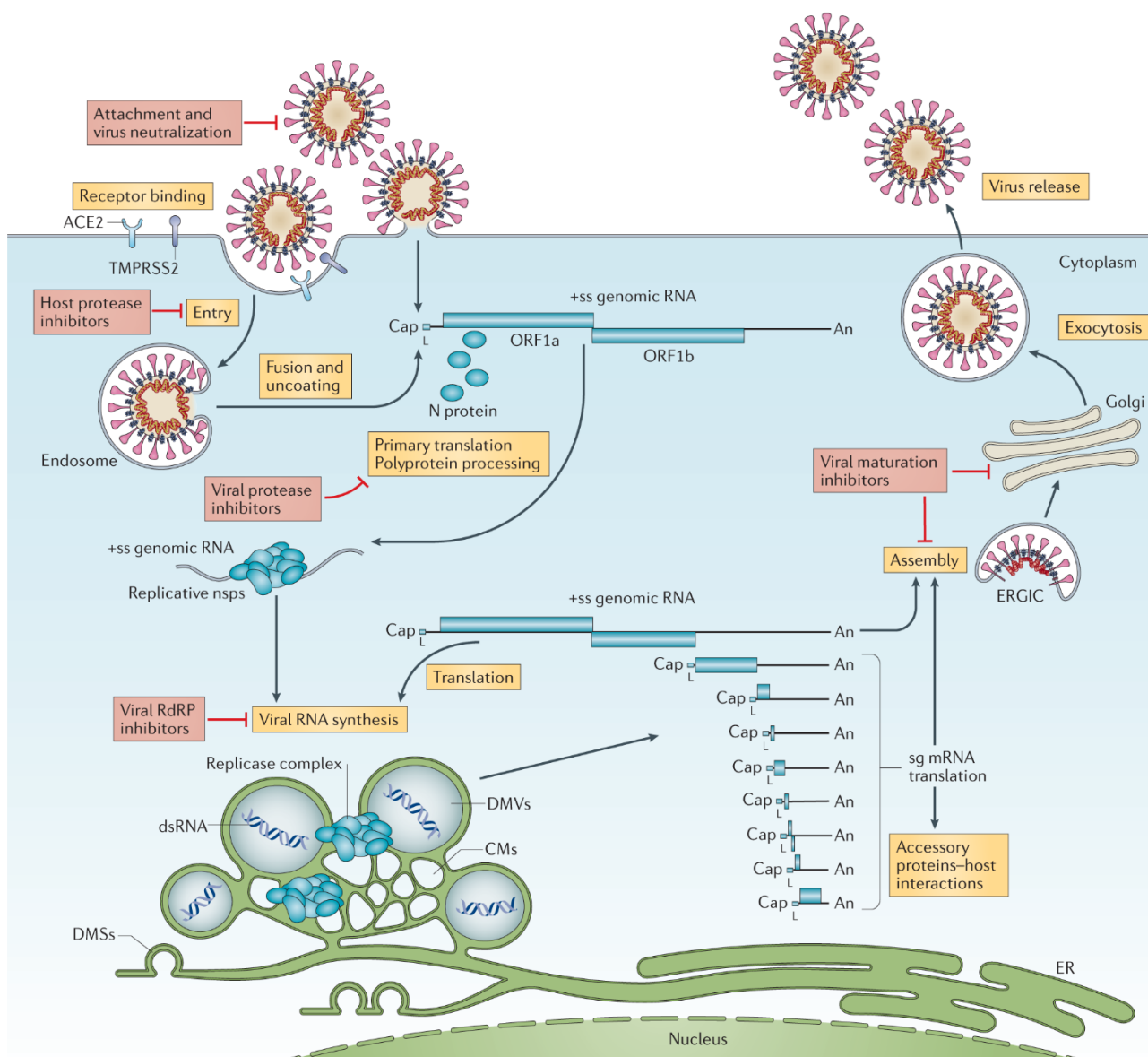


Figure 2: The SARS-CoV-2 replication cycle. The SARS-CoV-2 spike protein binds to the cellular ACE2 receptor to initiate viral entry. The viral genome is released into the cytoplasm of the infected cell following fusion at either the plasma membrane or endosomal membrane. Polyprotein translation and processing liberates nonstructural proteins to form the replication-transcription complex. Viral RNA synthesis occurs in double-membrane vesicles derived from the endoplasmic reticulum (ER). Newly translated structural proteins interact with viral genomes to assemble at the ER-to-Golgi intermediate compartment. Assembled virions exit the host cell by exocytosis. Image retrieved from V'kovski et al. (2020). *Nature Reviews Microbiology*. 19:155–170⁸.

1.1.4 Variants of Concern

The prolonged COVID-19 pandemic has seen the emergence of an assortment of SARS-CoV-2 variants. While SARS-CoV-2 possesses proofreading activity, the sheer scale of virus spread provided ample opportunities for mutation and subsequent selection. The first mutation to come to major public attention following the onset of the COVID-19 pandemic was D614G, an amino acid substitution in the S protein. Viruses with this mutation outcompeted ancestral lineages within a matter of months²⁶. D614G is associated with enhanced replicative fitness and transmissibility^{26,27}, and remains present in all variants discussed herein. In these variants, mutations may be found in several viral genes, such as S, N, M, E, ORF1ab, ORF8, and others²⁸. However, scientific discourse on variants tends to focus on mutations in the spike gene, which is responsible for viral entry and is the main target of SARS-CoV-2 vaccines and antibody-based therapies. While additional variants of concern have since been identified—most notably the omicron variant—this study involves only the alpha, beta, and delta variants. These named variants refer not only to one strain, but to broader collections of several sublineages.

1.1.4.1 Alpha Variant

The alpha variant (lineage B.1.1.7) was first reported in the United Kingdom in September of 2020. Key mutations in the S protein include N501Y—which increases affinity for ACE2 and promotes viral entry—and P618H, which is adjacent to the S1/S2 cleavage site and may promote cleavage²⁸. Additionally, amino acid deletions are found at positions 69-70 and 144 of the spike protein, which can lead in failure to detect the S gene in PCR diagnostic assays²⁹. The spike mutations underlie the variant's enhanced transmissibility compared to previous circulating strains; data from the United Kingdom showed a substantial increase in reproduction number (R_0) over earlier strains^{30,31}. R_0 refers to the number of new infections expected to be generated in a population by a single infection. Reports of illness severity were variable, with some studies showing an increased mortality risk^{32,33}, while others did not find evidence for an increase in severity³⁴. Though the alpha variant exhibited resistance to some anti-S monoclonal antibodies³⁵, its mutations did not appear to significantly impact the efficacy of S-

targeting vaccines³⁶. This variant largely ceased circulating in August 2021, when it was outpaced by the newer delta variant.

1.1.4.2 Beta Variant

The beta variant (lineage B.1.351) was first discovered in South Africa in October 2020, where it spread widely³⁷. Like the alpha variant, the beta variant contains the N501Y S mutation that enhances ACE2 binding affinity^{38,39}. Other mutations of concern in the S protein include E484K and K417N, which are also found in the RBD³⁷—such mutations underlie the variant's enhanced entry⁴⁰ and replication⁴¹ compared to the ancestral strain. Owing to these mutations, resistance to neutralizing antibodies emerged as a major concern for the beta variant, with reports of resistance to sera from vaccinated individuals and convalescent plasma^{35,42}. Moreover, this variant proved almost entirely resistant to bamlanivimab³⁵ and other monoclonal antibodies⁴³. Like the alpha variant, the beta variant ceased circulating around August 2021 when the delta variant became dominant.

1.1.4.3 Delta Variant

The delta variant (lineage B.1.617) was identified in India in May 2021—by July 2021, it would become the dominant strain worldwide. Spike mutations of interest in this variant include L452R, located in the RBD, and P681R, located near the furin cleavage site⁴⁴. In a similar fashion to other RBD and furin cleavage site-proximal mutations, these substitutions appear to enhance viral entry and S protein cleavage respectively⁴⁵. As with the beta variant, the delta variant exhibited resistance to monoclonal antibodies and convalescent sera⁴⁶, and was moreover associated with enhanced transmissibility^{47,48} and increased hospitalization risk⁴⁹. The delta variant circulated ubiquitously until approximately January 2022, when it was overtaken by the omicron variant.

1.2 Coronavirus Disease 2019 (COVID-19)

1.2.1 Symptoms & Transmission

Clinical manifestations of COVID-19 are variable, ranging from asymptomatic infection to respiratory failure and acute respiratory distress syndrome. Common symptoms include dry cough, fatigue, and fever, although a wide range of cold-like symptoms have

been observed⁵⁰. While SARS-CoV-2 is primarily a respiratory pathogen, other organs such as the kidneys^{51–53} and heart⁵⁴ are also targeted—this broad tissue tropism⁵⁵ can lead to complications such as multiple organ failure, renal failure, and arrhythmias^{50,56}. Infection can also lead to long-term complications such as persistent fatigue and shortness of breath, muscle and joint pain, and neurological difficulties^{57,58}. Symptoms generally present after an incubation period ranging from 1-14 days, although on average symptoms develop around 5 days post-infection^{59,60}. While it is difficult to precisely quantify asymptomatic cases, R_0 for SARS-CoV-2 has been estimated as approximately 2.5 for the ancestral strain⁶¹, though subsequent variants have demonstrated substantially enhanced transmissibility^{31,48}. Transmission occurs primarily by contact with respiratory secretions of infected individuals, which may involve liquid droplets or airborne aerosolized particles⁶². Overall, the COVID-19 pandemic constitutes a significant public health threat with potential for high mortality if healthcare resources are overwhelmed.

1.2.2 Host Transcriptional Response

During viral infection, recognition of viral replication intermediates by host pattern recognition receptors (PRRs) triggers a signaling cascade leading to the production of type 1 and 3 interferons (IFNs). Inflammation and IFN signaling are activated by nuclear factor kappa B (NF- κ B) and interferon regulatory factors (IRFs)—these transcription factors stimulate IFN expression (Fig. 3) to induce gene expression changes in host cells, thus generating an “antiviral state” that limits viral replication^{63,64}. Indeed, pathological features of many viruses can be attributed to the capability to antagonize and evade the IFN response⁶⁴. SARS-CoV-2 blunts the IFN response by a variety of mechanisms, such as sequestering viral RNA from cytosolic sensors, inhibiting components of IFN signaling pathways, and preventing host messenger RNAs (mRNAs) from being translated⁶⁵. In this context, Blanco-Melo *et. al.*⁶⁶ observed a limited IFN-I and IFN-III response following SARS-CoV-2 infection in human primary bronchial epithelial cells. While the majority of interferon-stimulated genes were not induced, a broader panel of chemokines and inflammatory cytokines were upregulated⁶⁶. These data were corroborated by examining the gene expression profiles in the lungs and sera of COVID-19 patients—low levels of IFN-I and -III were detected alongside robust chemokine

expression⁶⁶. However, similar studies evaluating transcriptional profiles in positive COVID-19 swabs have suggested that the IFN response is induced to a greater magnitude^{67,68}, though expression levels of interferon-stimulated genes appears to be a function of viral load⁶⁸. Interestingly, Lieberman *et. al.*⁶⁸ found that in infected human airway epithelial cells, IFN-induced genes were upregulated at 7 days post-infection, but not at 3 days post-infection. Overall, the human transcriptional response to SARS-CoV-2 infection is heterogenous and dependent on numerous factors, such as age, sex, viral load, and the timepoints post-infection at which gene expression is determined⁶⁶⁻⁶⁸.

These studies support the idea that the acute lung pathology and multi-organ failure that manifests in severe COVID-19 can largely be attributed to an imbalanced immune response. An initial dysregulation of the antiviral response, often characterized by a muted IFN signature but extensive transcription of chemokine genes, may cause unrestricted viral replication—subsequently, recruitment and stimulation of immune cells which produce Type 1 IFNs can eventually lead to extensive immune cell infiltration and inflammation^{65,66,69}. Indeed, severe COVID-19 patients exhibit higher levels of inflammatory cytokines in bronchoalveolar immune cells than do patients with moderate COVID-19⁷⁰. Furthermore, increases in inflammatory cytokines and leukoattractant chemokines early in infection are associated with the development of severe disease⁷¹. It is thus informative to consider the impact that antiviral therapeutics may have on virus-induced transcriptional changes.

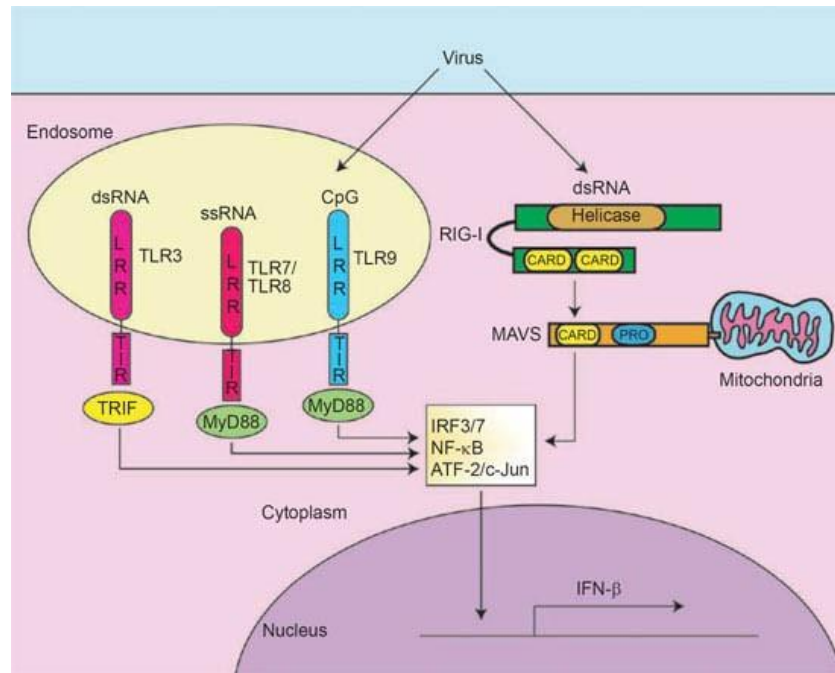


Figure 3: Schematic of antiviral innate immune pathways that activate IFN- β transcription. Following viral infection, cytoplasmic/endosomal sensors such as RIG-I and toll-like receptors recognize viral components or replication intermediates. Signaling pathways are initiated that lead to activation of transcription factors including NF- κ B and IRF3/7. These transcription factors translocate to the nucleus, where they activate transcription of various pro-inflammatory and immune-related genes, including IFN- β . Image retrieved from Seth et al. (2006). *Cell Research*. 141–147⁷².

1.3 Animal Models of COVID-19

In vitro experiments cannot fully recapitulate drug effects or clinical disease observed in human patients or live-animal models. To dissect the pathogenesis of COVID-19 and test relevant vaccines and pharmaceuticals, various animal models have been developed.

1.3.1 Mice

Mouse models of COVID-19 have been commonly used in vaccine and antiviral development⁷³. However, these models suffer from numerous complications, mainly stemming from lack of natural susceptibility to infection with SARS-CoV-2⁷⁴.

Accordingly, these models generally require the use of either mouse-adapted virus, or the exogenous expression of human ACE2 in mice. Mouse-adapted virus is generated by serial passage of SARS-CoV-2 in mouse tissue. However, such virus does not necessarily yield clinical disease comparable to a moderate disease course in humans^{75,76}. Several approaches for expression of human ACE2 in mice are available: transgenic mice can be generated that permanently express the receptor, while transient expression can also be induced by sensitizing the respiratory tract with ACE2-encoding adenoviral vectors⁷⁷. However, transgenic methods can yield an ectopic ACE2 expression pattern which can lead to viral replication and organ damage outside the respiratory tract and other tissues ordinarily implicated during infection^{78,79}.

1.3.2 Syrian Hamsters

Syrian hamsters are naturally susceptible to infection with SARS-CoV-2, requiring no modifications to the virus or exogenous ACE2 expression⁸⁰⁻⁸². Indeed, productive infection has been established in this model with inocula as low as 5 PFU⁸¹. Infection is initiated in the upper respiratory tract, with the virus subsequently spreading to the lungs⁸³. Weight loss in this model tends to be small in magnitude, and hamsters do not reach a humane endpoint by weight loss after infection⁸⁴.

While SARS-CoV-2 genomic RNA may be detected in a wide range of organs following challenge, infectious virus in immunocompetent hamsters can be recovered only from the lungs, trachea, nasal turbinates, and olfactory bulb⁸⁴. Virus replication in the lung peaks approximately between 3 and 5 days post-infection^{81,85} and declines thereafter; virus is typically cleared from the lungs by 8 days post-infection⁸². Histopathological lesions in the respiratory tract become apparent by 2 days post-infection, and persist for approximately 10-14 days post-infection. Inflammation of the bronchioles and trachea are widely reported and are typically accompanied by luminal infiltration of immune cells

and cellular debris, with possible intra-alveolar hemorrhage^{82,83,86,87}. In addition to histology, pathological features may also be determined by micro-computed tomography (microCT). Characteristic findings include ground-glass opacities that develop into consolidated lungs over time⁸⁴—these features mirror lung abnormalities observed in human patients with COVID-19 pneumonia⁸⁸. The major pathological features in the lung are mainly a consequence of immune activation and inflammation rather than direct virus-induced damage⁸³. Notably, sex and age differences in the severity of disease caused by SARS-CoV-2 in Syrian hamsters mirror what is seen in the human population, with older and male hamsters exhibiting more pronounced clinical symptoms and impeded viral clearance compared to young and female hamsters respectively⁸⁹⁻⁹¹. However, there appear to be no differences in infectious virus titers based on age⁹⁰ or sex⁸⁹.

SARS-CoV-2 infection activates IFN-I and IFN-III signaling in hamsters, which leads to the widespread production of pro-inflammatory cytokines such as IFN- γ and IL-6, and upregulation of chemokines to recruit leukocytes⁹². The transcriptional response to SARS-CoV-2 in hamsters exhibits overarching similarities to that in humans, with several key differences⁸³. While the initial inflammatory response is largely comparable between the two species, Syrian hamsters tend towards a less dysregulated immune response as disease progresses and are less likely to produce cytokine storms similar to those that drive severe disease in humans⁹³. Additionally, hamsters exhibit a lack of activation of TGF- β ⁹³, a multifunctional cytokine that provokes pulmonary fibrosis in human COVID-19 patients⁹⁴

One major limitation of the Syrian hamster model is the relative lack of molecular tools, such as antibodies, that are available for use with hamsters when compared to more common laboratory animals such as mice. This scarcity underlies the common use of transcriptome-based tools, such as quantitative PCR and RNA Sequencing, to evaluate levels of relevant immune markers in hamsters following infection. Overall, the hamster model strikes a balance between cost-effectiveness and recapitulation of human COVID-19 disease phenotypes⁸⁴.

1.3.3 Ferrets

Ferret models have seen widespread usage in COVID-19 research since the beginning of the pandemic, despite their elevated cost compared to other small-animal models^{20,66,95}. Like hamsters, ferrets are naturally susceptible to SARS-CoV-2 infection^{96,97}. Infection in this model primarily affects the upper respiratory tract^{96,97}, though the lower respiratory tract and gastrointestinal tract are implicated as well⁹⁵. Following infection, pathological lesions develop in the lungs; however, these features are milder than in human COVID-19 patients⁹⁸. Mild clinical symptoms including cough and fever may develop, while weight loss does not tend to occur⁹⁹.

1.3.4 Non-Human Primates

Non-human primates (NHPs), such as rhesus macaques or African green monkeys, offer the obvious advantage of their similarity in physiology to humans. NHPs are readily infected with SARS-CoV-2 and yield similar patterns of disease as do humans, including viral replication in the respiratory tract, inflammation alongside infiltration of immune cells into the lungs, and a neutralizing antibody response¹⁰⁰. This disease state recapitulates mild or moderate COVID-19^{101,102}. However, the use of NHPs as laboratory models is complicated by high cost in conjunction with limited availability and logistical challenges.

1.4 Therapeutics for COVID-19

Vaccination is widely recognized to be the most important component of severe COVID-19 prevention. However, as vaccines are prophylactic by nature, therapeutics fill an important role in treatment of infected patients at risk for progression to severe disease. COVID-19 therapeutics currently approved for use in Canada fall into one of 3 categories: nucleoside analogues, protease inhibitors, and monoclonal antibodies.

1.4.1 Nucleoside Analogues

Remdesivir (Veklury) is an intravenously administered agent with broad-spectrum antiviral activity. Upon entry into cells, it is metabolized into an ATP nucleoside analogue with higher affinity for the viral RdRp than ATP. In this capacity, the drug

interferes with viral RNA synthesis—remdesivir incorporation into nascent RNA leads to delayed-chain termination, which is thought to be the consequence of steric hindrance¹⁰³. While remdesivir was effective at inhibiting SARS-CoV-2 replication in cell culture^{104,105} and was shown to reduce clinical disease in rhesus macaques¹⁰⁶, its efficacy in real-world settings has remained contentious. The World Health Organization (WHO) Solidarity trial, which evaluated COVID-19 drug candidates in over 400 hospitals worldwide, found that remdesivir had no effect on mortality or hospitalization duration in ventilated patients, and exhibited only a small effect against death or initiation of ventilation in other hospitalized patients¹⁰⁷.

1.4.2 Protease Inhibitors

Nirmatrelvir and ritonavir (Paxlovid) is an orally administered drug specifically developed for treatment of COVID-19. Nirmatrelvir is an inhibitor of SARS-CoV-2 M^{pro} that covalently binds a cysteine residue responsible for the viral protease's catalytic activity¹⁰⁸. M^{pro} is essential for viral replication, cleaving the majority of nsps during the replication cycle⁸ and is highly sequence-specific, limiting collateral inhibition of host proteases by nirmatrelvir. In this drug mixture, the metabolic degradation of nirmatrelvir is slowed by ritonavir, which inhibits the metabolic enzyme CYP3A4¹⁰⁹. In a phase 2/3 clinical trial, Paxlovid treatment resulted in an 89% reduction over placebo in progression to severe COVID-19¹¹⁰. Accordingly, the drug is presently authorized for use in patients with mild-to-moderate COVID-19 that are at risk of developing severe COVID-19. Recently, case reports have emerged that detail a “rebound” of COVID-19 after completion of a Paxlovid treatment course. This phenomenon typically involves recurrence of COVID-19 symptoms and/or a positive COVID-19 test after resolution of symptoms or testing negative. While these reports are largely preliminary¹¹¹, the Centres for Disease Control and Prevention (CDC) has issued an advisory on the subject. Moreover, Paxlovid is contraindicated with a range of drugs that are metabolized by CYP3A4.

1.4.3 Monoclonal Antibodies

Monoclonal antibodies (mAbs) are antibodies derived from a single B cell clone, and thus have specificity for the same epitope. In general, the interaction between a mAb and a virus may inhibit the virus in several ways: i) by blocking the interaction between the virus and its cellular receptor, ii) by opsonization of the virus and subsequent phagocytosis, and iii) by marking infected cells for killing by effector cells or the complement system¹¹². Presently, there are four mAb-based therapies authorized in Canada: bamlanivimab, casirivimab/imdevimab, sotrovimab, and tixagevimab/cilgavimab. Each works by the same basic mechanism: the antibodies recognize and bind a specific epitope present on the RBD of the SARS-CoV-2 S protein, thereby neutralizing the virus and preventing the RBD from interacting with ACE2. Generally, clinical studies showed that mAb administration reduced the risk of COVID-19 patients requiring hospitalization¹¹³. However, the emergence and ubiquitous spread of the SARS-CoV-2 omicron variant has considerably weakened the case for mAb-based therapies. Largely, established mAbs are significantly less effective at neutralizing the omicron variant¹¹⁴, underscoring the risk in developing therapies that target specific viral epitopes, which may mutate. While bebtelovimab has been identified as an outlier that retains efficacy against certain omicron lineages¹¹⁵, this therapy is not currently approved for use in Canada.

1.5 BOLD-100

While the presently approved agents have each seen some level of success in preclinical and clinical studies, they are nonetheless limited in their applications by various factors. Accordingly, there remains a need for the discovery and testing of novel COVID-19 therapeutics. Although the process of drug discovery is time-consuming and resource-intensive, repurposing existing therapeutic agents with favourable safety profiles is a viable strategy for rapid entry into clinical trials and deployment. One such agent being repurposed is BOLD-100, a small ruthenium-based molecule currently in clinical development for the treatment of advanced cancers.

1.5.1 Ruthenium-based Drugs

Ruthenium (Ru)-based drugs came to scientific attention in the 1980s as compounds that were observed to preferentially localize in tumour tissue and exhibit lower toxicity¹¹⁶⁻¹¹⁸ than traditional platinum-based chemotherapeutics¹¹⁹. Depending on the compound, pharmacological activity may be ascribed to the metal centre and/or its ligands. While the ruthenate anion may itself interact with cellular targets, it may also simply act as a scaffold to carry bioactive ligands to a target site where they are released and exert their effects^{120,121}. Metal-based drugs act by a multitude of mechanisms, mainly involving interactions with DNA or various proteins such as enzymes and transcription factors¹²¹.

1.5.2 Overview of BOLD-100

BOLD-100 (sodium trans-[tetrachlorobis(1H-indazole)ruthenate(III)]dihydrate) was first produced as a derivative of an earlier ruthenium chemotherapeutic, KP1019 (indazole trans-[tetrachlorobis(1H-indazole)ruthenate(III)]). The major limiting factor for clinical applications of KP1019 was its poor solubility, which precluded determination of a maximum tolerated dose¹¹⁶. The development of KP1339 (a.k.a. NKP-1339, IT-139) addressed this complication by replacement of the indazolium counterion with sodium, thereby profoundly improving aqueous solubility¹²². BOLD-100 represents the same chemical compound as KP1339/IT-139, but is synthesized from KP1019 by a different pathway involving a cesium salt intermediate. This alternate synthesis route was developed to improve purity and scale in the manufacturing process. Collectively, these 3 compounds share the same ruthenium centre and overlapping chemistry, and are presently referred to as the “BOLD-100 family” of small molecules.

Structurally, BOLD-100 consists of a ruthenium centre to which four equatorial chloride ligands and two axial indazole ligands are attached¹²³. This octahedral complex carries a negative charge and is balanced with a sodium cation (Fig. 4).

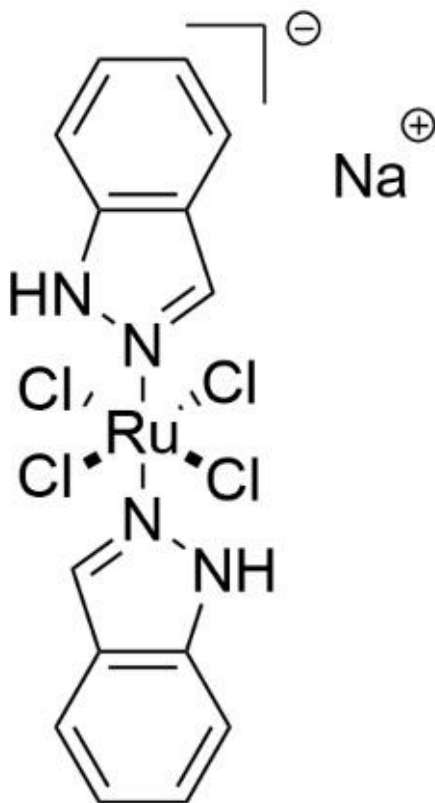


Figure 4: Chemical structure of BOLD-100 (sodium *trans*-[tetrachlorobis(1H-indazole)ruthenate(III)]dihydrate).

1.5.3 Properties of BOLD-100

For BOLD-100-family drugs, uptake in cell culture occurs rapidly, being completed within one hour of administration¹²⁴. Following uptake, BOLD-100 becomes distributed in both the cytosol and nucleus¹²⁵. In the cytosol, BOLD-100 is largely bound to one of two discrete fractions of protein complexes: low molecular-weight complexes of <40 kDa, and high molecular-weight complexes of >700 kDa¹²⁴.

Upon intravenous administration, BOLD-100 rapidly binds to human serum albumin (HSA)^{126–128}. Though other serum proteins such as transferrin are bound by BOLD-100, HSA appears to be the major binding target in the bloodstream¹²⁶. This interaction is initiated by coordinative bonding between the indazole ligands on BOLD-100 and

surface histidine residues on HSA¹²⁹. Following this rapid coordination event, ligand exchange between the indazoles and histidine occurs, as well as between the BOLD-100 chloride ligands and water molecules^{130,131}. This process results in the slow formation of covalent bonds between BOLD-100 and HSA. The propensity of BOLD-100 to bind HSA is thought to be a major contributing factor to its relatively extended half-life and preferential accumulation in tumour cells¹³². In murine models, BOLD-100 becomes systemically distributed upon administration, with highest concentrations in the lungs, liver, colon, kidneys, and thymus¹²⁷. As in the human context, the majority of drug is bound to serum albumin in plasma¹²⁷. In contrast to similar metal-based agents, BOLD-100 does not bind DNA as a major target¹³³.

1.5.4 Clinical Development of BOLD-100

In 2016, BOLD-100 underwent a Phase 1 open-label dose escalation study to evaluate safety and tolerability in patients with advanced solid tumours¹¹⁷. Patients were randomized into cohorts receiving escalating doses of intravenous BOLD-100. Overall, BOLD-100 treatment was well-tolerated—in general, treatment-emergent adverse events were gastrointestinal in nature and minimized upon antiemetic administration. Furthermore, no adverse trends were reported in terms of chemical or haematological abnormalities. Drug clearance exhibited a relationship with body size rather than body weight—for this reason, dosage was reported in terms of body size (mg/m^2). The maximum tolerated dose (MTD) was determined to be $625 \text{ mg}/\text{m}^2$, while the mean half-life was 113 hours (4.7 days). In this trial, BOLD-100 monotherapy demonstrated a modest antitumour effect; however, combination therapeutic strategies were identified as a more promising direction for future studies. To this end, BOLD-100 is currently being evaluated in a Phase 1b/2a clinical trial in combination with folinic acid, fluorouracil, and oxaliplatin (FOLFOX) for advanced gastrointestinal cancer¹³⁴.

1.5.5 Mechanistic Targets of BOLD-100

BOLD-100 exhibits a complex and multimodal mechanism of action, which has not yet been fully characterized. Prior to the COVID-19 pandemic, BOLD-100 had never been tested as an antiviral—accordingly, the existing body of literature focuses almost

exclusively on the drug's anticancer properties. In this context, the overall mechanism comprises several major components that collectively lead to the death of tumour cells.

1.5.5.1 The Unfolded Protein Response and *GRP78* Inhibition

A major focus of BOLD-100 research in oncology is the drug's ability to modulate the unfolded protein response (UPR) in stressed cells. A major component of the UPR that can be affected by BOLD-100 is 78 kDa glucose-regulated protein (*GRP78*), a key endoplasmic reticulum (ER) chaperone and master regulator of the UPR¹³⁵. When the ER undergoes stress due to increased protein synthesis and pressure on its folding capacity, the UPR becomes activated. This response consists of a series of complex pathways that act to relieve ER stress or induce apoptosis, depending on intensity and duration of the stimulus¹³⁵. Under normal physiological conditions, *GRP78* sequesters the ER signaling proteins inositol-requiring enzyme 1 (IRE1), PKR-like ER kinase (PERK), and activating transcription factor 6 (ATF6). Upon stress, *GRP78* dissociates from these proteins, activating their respective signaling pathways to restrict further protein synthesis and upregulate chaperone proteins that inhibit protein aggregation and increase folding capacity¹³⁵. If ER stress continues for an extended time, pro-apoptotic pathways are induced, causing cell death. In addition to its role in regulating the UPR, *GRP78* facilitates many critical ER processes, such as protein folding and regulation of calcium homeostasis¹³⁵.

GRP78 levels are highly upregulated during stress and disease, including in cancer and viral infection¹³⁶. In general, stress induction of *GRP78* is implicated in cellular prosurvival pathways and inhibition of apoptosis. In certain tumour cells, upregulation of *GRP78* is associated with drug resistance and metastasis¹³⁷. Of note, *GRP78* has previously been suggested as a promising target for antiviral therapeutics. Upon stress-induced upregulation, *GRP78* becomes localized throughout the cell, including in the cell membrane^{138,139}. In this context, literature supports that *GRP78* impacts multiple different aspects of the viral life cycle, including initial binding and infection of the host cell, and viral replication¹⁴⁰.

In the context of cellular stress, BOLD-100 inhibits the upregulation of GRP78, thereby depriving cancer cells of a crucial factor for growth¹⁴¹. This effect is time- and cell line-dependent and has potential to occur at both the transcriptional and post-transcriptional levels, depending on cell type. Of note, this effect does not appear to depend on the ruthenate moiety¹⁴¹.

1.5.5.2 Other Effects on the Cellular Stress Response

While BOLD-100 may suppress certain elements of the cellular stress response such as *GRP78*, it can also act as an inducer of the overall response. BOLD-100 treatment in a colon cancer spheroid model induced elements of an immunogenic cell death (ICD) signature, characterized by increased phosphorylation of PERK and EIF2 α —activation of this pathway attenuates translation and can promote apoptosis¹⁴². In the same study, BOLD-100 treatment also induced a marked increase in reactive oxygen species (ROS) production¹⁴². Production of ROS has previously been characterized as a major component of the drug's multimodal mechanism of action in oncology, and is linked to ER stress^{143,144}. Interestingly, BOLD-100 treatment induced ROS in human breast cancer cells at higher levels than did *tert*-butyl hydroperoxide, an established positive control for ROS induction¹⁴³. This effect accompanied cell cycle arrest of the treated cells in G2/M phase as well as downregulation of several key genes in the DNA damage response¹⁴³.

1.5.5.3 Cellular Protein Binding Targets

Given that BOLD-100 is unlikely to bind DNA as a major cellular target, its protein interactors are of particular interest. Recently, Neuditschko *et al* used a shotgun proteomics approach to determine probable protein targets of BOLD-100¹²⁵. Taking advantage of the known binding tendencies between BOLD-100 and HSA, the authors performed competitive and non-competitive pulldowns using BOLD-100:HSA adducts in HCT116 colon cancer cell lysates. By subtracting proteins that bound HSA in the absence of BOLD-100, they determined selective binding partners for BOLD-100. In total, 57 cellular proteins were identified as likely interactors of BOLD-100, which is lower than expected based on the interaction profiles of other metallodrugs¹²⁵. Interestingly, the most highly enriched interactor was GTF2I, a transcription factor implicated in several

cellular processes, including responses to ER stress and upregulation of GRP78– this interaction may contribute to the BOLD-100-induced downregulation of GRP78 observed in certain cell lines. Of additional interest, BOLD-100 interacted with several components of the large ribosomal subunit, indicating a potential role for interaction with ribosomes in the drug’s mechanism of action. Indeed, in this model, BOLD-100 (as measured by Ru accumulation) was mostly bound to a high molecular weight fraction of protein complexes, which is consistent with ribosome binding. Additionally, BOLD-100 treatment caused ribosomes to detach from the ER and form clusters of polyribosomes¹²⁵.

1.5.5.4 Antiviral Potential for BOLD-100

Previous research into Ru drugs as antimicrobials predominantly focused on their antibacterial or antiparasitic properties¹²⁰. However, the COVID-19 pandemic prompted a renewed effort to repurpose diverse classes of therapeutic agents for treatment of COVID-19. In this context, several metallodrugs, including ruthenium-based compounds, were evaluated for their antiviral potential. For instance, the BOLD-100 precursor KP1019 demonstrated anti-SARS-CoV-2 activity in Calu-3 human lung cancer cells¹⁴⁵. Other ruthenium drugs have shown promise in an antiviral context – several test compounds have been shown to inhibit replication of diverse viruses, such as human immunodeficiency virus type 1 (HIV-1)¹⁴⁶ and Polio virus¹⁴⁷.

1.6 Rationale, Hypothesis, and Objectives

The need for treatment for COVID-19 warrants expanded research into novel therapeutics approaches. BOLD-100, as a clinical stage investigational agent that inhibits a key factor for viral replication, is a promising option. The objective of this project was to characterize this potential inhibitor in SARS-CoV-2-infected tissue culture cells and infected animal models. We hypothesized that BOLD-100 inhibits SARS-CoV-2 replication and progression of COVID-19. To address this hypothesis, we proposed the following aims:

- i) Characterize the antiviral activity of BOLD-100 against SARS-CoV-2 in physiologically relevant cell lines

- ii) Characterize the antiviral activity of BOLD-100 in a hamster model of COVID-19
- iii) Evaluate the antiviral activity of BOLD-100 against additional viruses of public health concern

2 Chapter 2: Materials and Methods

2.1 Cell Culture

Vero E6 cells (for SARS-CoV-2 infection) and A549 cells (for HAdV-C5 infection) were purchased from ATCC.

HEK 293T-ACE2 cells (for SARS-CoV-2) infection were obtained from BEI Resources, NIAID, NIH.

HeLa-TZM-bl cells and HOS CD4⁺ CXCR4⁺ cells (for HIV-1 infection) were obtained from the NIH HIV Reagent Program, Division of AIDS, NIAID, NIH.

All cell lines were maintained in standard growth medium (Dulbecco's Modified Eagle's Medium (DMEM)), supplemented with 10% heat-inactivated Fetal Bovine Serum (FBS), 100 U/ml Penicillin and 100 µg/ml Streptomycin at 37°C with 5% carbon dioxide (CO₂). For *in vitro* experiments involving virus infections, virus was diluted in DMEM supplemented with 2% FBS, 100 U/ml penicillin and 100 µg/ml streptomycin.

2.2 Viruses

The following replication-competent SARS-CoV-2 isolates were acquired from BEI Resources, NIAID, NIH: 2019/nCoV/USA-WA-I/2020, hCoV-19/England/204820464/2020, hCoV-19/South Africa/KRISP-EC-K005321/2020, hCoV-19/USA/PHC658/2021.

The following reagent was obtained through the NIH HIV Reagent Program, Division of AIDS, NIAID, NIH: Human Immunodeficiency Virus Type 1 AD.MDR01, ARP-11700, contributed by Dr. Martin Markowitz and Dr. Hiroshi Mohri.

HAdV-C5 strain Adenoid 75 was purchased from ATCC.

2.3 Virus Propagation

2.3.1 SARS-CoV-2

SARS-CoV-2 was propagated and provided by the ImPaKT facility at Western University. Briefly, Vero E6 cells were grown to 70% confluency in T-150 cell culture flasks. Infectious SARS-CoV-2 (2×10^5 PFU) was diluted in 5 mL serum-free DMEM. The existing cell culture media was removed from the flask and SARS-CoV-2 containing media was added. The flask was incubated for 1 hour at 37°C and 5% CO₂ for 1 hour. The virus inoculum was then removed and 30 mL of DMEM + 2% FBS was added. The flask was incubated at 37°C and 5% CO₂ for 72 hours, after which the virus-containing supernatant was removed and centrifuged at $500 \times g$ for 10 min to pellet cellular debris. The supernatant was removed and aliquoted into cryovials for storage at -80 °C. Virus titre was determined by 50% tissue culture infectious dose (TCID₅₀) assay on Vero E6 cells¹⁴⁸. Specifically, 15000 Vero E6 cells were seeded in 96-well plates 24 hours prior to infection. On the day of infection, the cell culture medium was removed and the cells were washed 1x with PBS. Ten-fold serial dilutions of stock SARS-CoV-2 were prepared in DMEM + 2% FBS. Cells were infected in triplicate with 90 µL of either undiluted virus, one of the serial dilutions of virus, or media only as a negative control. Cells were incubated for 72 hours at 37°C with 5% CO₂ and visually evaluated for cytopathogenicity to determine infection. TCID₅₀/mL was calculated by the Reed-Muench method.

2.3.2 HIV-1 AD.MDR01

HIV-1 AD.MDR01 was propagated in U87.R5 cells. Briefly, U87.R5 cells were seeded in T-150 cell culture flasks. Once cells reached 80% confluency, the cell culture medium was removed. A 1 mL aliquot of stock virus was diluted in 30 mL DMEM + 2% FBS and added to the flask. Cells were incubated at 37°C with 5% CO₂ for 7 days. The virus-containing supernatant was harvested from the flask and centrifuged at $500 \times g$ for 10 minutes to pellet cell debris. The resulting supernatant was aliquoted into cryovials and stored at -80 °C. Virus titre was determined by TCID₅₀ assay on TZM-bl cells. Specifically, 15000 TZM-bl cells were seeded in 96-well plates 24 hours prior to infection. On the day of infection, the cell culture medium was removed. Ten-fold serial

dilutions of propagated HIV-1 AD.MDR01 were prepared in DMEM + 2% FBS. Cells were infected in triplicate with 90 μ L of either undiluted virus, one of the serial dilutions of virus, or media only as a negative control. Cells were incubated for 48 hours at 37°C with 5% CO₂ and infection in each well was determined using the Galacto-Star™ β -Galactosidase Reporter Gene Assay System (ThermoFisher). TCID₅₀/mL was calculated by the Reed-Muench method.

2.3.3 HAdV-C5

HAdV-C5 strain Adenoid 75 was propagated in HEK 293T cells. Briefly, HEK 293T cells were grown to 60% confluency in T-75 cell culture flasks. The cell culture media was removed and the cells were washed 1x with PBS before addition of HAdV-C5 diluted in 4 mL DMEM + 2% FBS (MOI = 1). Flasks were incubated at 37°C with 5% CO₂ with periodic rocking for 3 hours, after which 10 mL of DMEM + 10% FBS was added to each flask. Flasks were incubated at 37°C with 5% CO₂ for 72 hours, after which the contents were removed and centrifuged at 500 \times g for 10 min to pellet cells. The supernatant was discarded and cells were resuspended in sterile PBS (1 mL per T-75 flask). Resuspended cells were subjected to 3 freeze-thaw cycles to liberate virus, after which the virus-containing solution was centrifuged at 500 \times g for 10 min to pellet cellular debris. The supernatant was aliquoted into cryovials and stored at -80°C. Virus titre was determined by plaque assay on A549 cells (see “2.13 Adenovirus Infections & Plaque Assays”).

2.4 BOLD-100 Preparation

BOLD-100 drug substance powder was provided by Bold Therapeutics, Inc. For *in vitro* experiments, BOLD-100 powder was dissolved in dimethylsulfoxide (DMSO) to generate a stock solution and was further diluted in cell culture media for working solutions (final DMSO concentration always below 0.1%). For hamster experiments, BOLD-100 powder was dissolved in citrate-buffered saline (CBS) for intravenous (i.v.) injection.

2.5 SARS-CoV-2 Infections

Twenty-four hours prior to infection, 15 000 Vero E6 or 293T-ACE2 cells were seeded in 96-well plates. Previously described SARS-CoV-2 isolates (see “Viruses & Cell Culture”) were diluted in cell culture media and added to cells for 1 hour at 37°C with 5% CO₂ for adsorption of viral particles (Multiplicity of infection (MOI)= 0.001, 0.01, 0.05, or 0.1 depending on experiment). The MOI is defined as the ratio of infectious virus particles to the total number of cells. The virus inoculum was then removed and fresh media supplemented with BOLD-100 was added. Either 24 or 48 hours post-infection, cell lysates and/or virus-containing supernatants were harvested for downstream analysis. Specifically, plates containing cells were centrifuged at 500 × *g* for 10 min and virus-containing supernatants were removed. Cell lysates were prepared by resuspending the remaining cells in either radioimmunoprecipitation buffer (50 mM Tris-HCl (pH 7.4), 150 mM NaCl, 0.5% sodium deoxycholate, 0.5% sodium dodecyl sulfate (SDS))) for Western blot or RNA lysis buffer (ThermoFisher PureLink RNA Mini Kit #12183020) for RNA extraction.

2.6 Microscopy and Image Acquisition

Random brightfield images were obtained at 20x magnification using an EVOS M7000 imaging system (ThermoFisher Scientific).

2.7 Cell Viability Assays

2.7.1 CellTiter-Glo

For determination of cell viability by CellTiter-Glo viability assay (Promega), 15,000 Vero E6 cells were seeded in 96-well plates the day prior to BOLD-100 treatment and infection with SARS-CoV-2. Cells were infected with SARS-CoV-2 at MOI 0.01 or mock-infected with diluent alone for a 1-hour adsorption period, after which the inoculum was removed and fresh media supplemented with BOLD-100 was added. Seventy-two hours post-infection (h.p.i.), relative adenosine triphosphate (ATP) levels were measured in each well as a measure of cell viability according to manufacturer’s instructions.

2.7.2 Cell Counting Kit-8

For determination of cell viability by Cell Counting Kit-8 (CCK8) assay (Sigma), cells were seeded in 96-well plates (15000 cells/well) and incubated at 37°C & 5% CO₂ for 24 hours. Subsequently, cells were treated with varying concentrations of BOLD-100. Forty-eight hours post-treatment, relative cell viability was determined using CCK8 assay (Sigma) according to manufacturer's instructions. Absorbance values at 450 nm in wells containing BOLD-100-treated cells were corrected for background absorbance contributed by the cell culture medium and normalized to absorbance values in wells containing mock-treated cells to determine relative cell viability. The 50% cytotoxic concentration (CC₅₀) was calculated by nonlinear regression (Sigmoidal, 4PL, X is concentration) using Prism v9.3.1 (GraphPad).

2.8 Antibodies and Western Blotting

2.8.1 Primary Antibodies

Rabbit anti-GAPDH (1 mg/mL) was purchased from Sigma and diluted 1:20000 in Phosphate Buffered Saline-Tween (1.37 M NaCl, 27 mM KCl, 100 mM Na₂HPO₄, and 18 mM KH₂PO₄, 1% Tween) (PBS-T) prior to use. Mouse anti-SARS/SARS-CoV-2 Coronavirus Nucleocapsid Monoclonal Antibody (E16C) (0.1 mg/mL) was purchased from ThermoFisher Scientific and diluted 1:2000 in PBS-T prior to use.

2.8.2 Secondary Antibodies

IRDye® 800 CW goat anti-rabbit IgG (1 mg/mL) (1:20000 dilution in PBS-T) and IRDye® 680RD goat anti-mouse IgG (1 mg/mL) (1:20000 dilution in PBS-T) were purchased from LI-COR BioScience

2.8.3 Western Blotting

Cell lysates were mixed with 4x protein loading dye (40% glycerol, 240 mM Tris/HCl pH 6.8, 8% SDS, 0.04% bromophenol blue, and 5% betamercaptoethanol) in a 1:3 dye to sample ratio and heated at 95°C for 20 min to denature proteins. Twenty µL of each cell lysate sample and 0.7 µL of BLUeye Protein Ladder (FroggaBio) were loaded onto a 10% SDS-PAGE gel. The gel was submerged in 1x Protein Running Buffer (12 mM Tris

base, 96 mM glycine, and 2mM SDS in ddH₂O) and run at 90 V for 2 hours. Protein was transferred onto 0.2 µm Low Fluorescence Amersham Hybond Polyvinylidene difluoride (PVDF) membrane (GE Healthcare Life Sciences) by semi-dry transfer with Transfer Buffer (8mM Tris Base, 190 mM glycine, and 20% methanol in ddH₂O) for 90 min at 20 V. The PVDF membrane was incubated in 10 mL of a 50:50 solution of LI-COR Odyssey® Blocking Buffer and Phosphate Buffered Saline (PBS) (1.37 M NaCl, 27 mM KCl, 100 mM Na₂HPO₄, and 18 mM KH₂PO₄) for 60 min. The membrane was incubated overnight at 4°C with the primary antibodies rabbit anti-GAPDH (1:20 000 dilution) and mouse anti-SARS-CoV-2 N (1:2000 dilution). The membrane was washed 3x with PBS-T for 10 min and probed with the secondary antibodies IRdye® 800 CW goat anti-rabbit IgG (1:20000 dilution) and IRdye® 680RD goat anti-mouse IgG (1:20000 dilution). The membrane was washed 3x for 10 min in PBS-T, scanned using the LI-COR Odyssey machine (an infrared light scanner), and visualized with the Odyssey v3.0 software (LI-COR BioScience). Densitometric analysis was performed using ImageJ 1.53 g 64-bit software (NIH, USA).

2.9 RNA Extraction and Quantitative RT-PCR

Cell lysates and supernatants were prepared for RNA extraction as previously described (see “2.5 SARS-CoV-2 Infections”).

Total RNA was extracted using the PureLink RNA mini kit (Ambion, Life Technologies) according to manufacturer’s instructions, except in the case of the HIV-1 antiviral assay described in Fig.18. For this experiment, viral RNA was extracted using the MagMax-96 Viral RNA Isolation kit (Applied Biosystems, ThermoFisher) from infected cell supernatants according to manufacturer’s instructions.

Each quantitative RT-PCR (RT-qPCR) reaction consisted of 1-10 µL of sample RNA, 5 µL of TaqMan™ Fast Virus 1-Step Master Mix, 1 µL of gene-specific TaqMan™ Gene Expression Assays (20X), and ribonuclease-free water to bring the total reaction volume to 20 µL. Relative levels of RNA were measured by RT-qPCR using the QuantStudio5 qPCR machine (Applied Biosystems) under the following cycling conditions: 5 min at 50°C, 20 sec at 95°C and 40 cycles of 3 sec at 95°C and 30 sec at 60°C. TaqMan™ Fast

Virus 1-Step Master Mix permits RNA quantification by RT-qPCR without prior synthesis of complementary DNA in a separate reaction.

The following TaqMan™ Gene Expression Assays were used: SARS-CoV-2 N gene (Vi07918637_s1), HIV-1 LTR (Vi03453409_s1), GAPDH (Hs02786624_g1), TLR3 (Hs00152933_m1), and CXCL11 (Hs00171138_m1). Relative fold changes were calculated by the $2^{-\Delta\Delta Ct}$ method.

2.10 RNA Sequencing

All samples were sequenced at the London Regional Genomics Centre (Robarts Research Institute, London, Ontario, Canada) using the Illumina NextSeq 500 (Illumina Inc., San Diego, CA).

Total RNA samples were quantified using the NanoDrop (Thermo Fisher Scientific, Waltham, MA) and quality was assessed using the Agilent 2100 Bioanalyzer (Agilent Technologies Inc., Palo Alto, CA) and the RNA 6000 Nano kit (Caliper Life Sciences, Mountain View, CA). They were then processed using the Vazyme VAHTS Total RNA-seq (H/M/R) Library Prep Kit for Illumina (Vazyme, Nanjing, China) which includes ribosomal RNA (rRNA) reduction.

Briefly, samples were rRNA depleted, fragmented, cDNA was synthesized, indexed, cleaned-up and amplified via PCR. Libraries were then equimolar pooled into one library and size distribution was assessed on an Agilent High Sensitivity DNA Bioanalyzer chip, and quantitated using the Qubit 2.0 Fluorimeter (Thermo Fisher Scientific, Waltham, MA).

The library was sequenced on an Illumina NextSeq 500 as a 76 bp single end run, using one High Output v2 kit (75 cycles). Fastq data files were analyzed using Partek Flow (St. Louis, MO). After importation, data was aligned to the Homo sapiens hg19 genome using STAR 2.7.3a and annotated using Ensemble v100 after filtering for PCR duplicates. Features with less than 9 reads were filtered out, followed by normalization by CPM (Counts Per Million and add 0.0001). Fold change and p-values were determined using Partek Flow's Gene Specific Analysis (GSA). Filtered lists of genes changing ≥ 1.5 fold

and with a p-value of less than 0.05 were then analyzed for enriched Gene Ontology (GO) pathway terms.

2.11 *In Vivo* Experiments

2.11.1 Ethics Statement

All animal husbandry and experimentation was conducted in accordance with the guidelines set by the Canadian Council on Animal Care under Animal Use Protocols #2020-065 and #2021-003, which were approved by the Animal Care Committee at Western University.

2.11.2 Hamster Maintenance

4–6-week-old male Syrian hamsters were obtained from Envigo (Han Aura) or Charles River (LVG), pre-purchased with jugular vein catheterization. Hamsters were held for a 3-day acclimation period before any experimentation took place, and were individually housed in cages on a vented rack. Hamsters were monitored and weighed daily during experiment periods. Hamsters were placed under isoflurane anaesthesia for all procedures.

2.11.3 BOLD-100 Dose Escalation

Syrian hamsters (4–6 weeks old) were treated intravenously (i.v.) with vehicle (citrate-buffered saline) or BOLD-100 at doses of 5, 10, 12.5, 15, 30, 50, or 75 mg/kg. Hamsters were weighed and monitored daily for signs of distress or disease, and euthanized before the study endpoint if deemed to be in severe distress by institutional veterinary staff. Seven days post-treatment, hamsters were sacrificed and organ tissues were collected to evaluate any drug-induced pathology.

2.11.4 SARS-CoV-2 Infections and Organ Collection

Syrian hamsters (4–6 weeks old) were infected intranasally (i.n.) with 10^3 PFU SARS-CoV-2 (2019/nCoV/USA-WA-I/2020) (50 μ L/nare) and treated i.v. with vehicle (citrate-buffered saline) or BOLD-100 (15 mg/kg) either 24 hours before infection (Day -1), one hour before infection (Day 0), or 24 hours post-infection (Day +1). Hamsters were

sacrificed 4 days post-infection. The following organs were collected after sacrifice from each hamster: lungs, trachea, brain, nasal turbinates, heart, liver, and kidneys. Organs were either fixed overnight in 10% formalin for histopathologic analysis or stored in cold PBS immediately prior to determination of viral load by plaque assay.

2.11.5 SARS-CoV-2 Plaque Assays

Viral load in the lungs and trachea was determined by plaque assay. Briefly, the left lung lobe or whole trachea were mechanically homogenized with a bead mill homogenizer (Bullet Blender Tissue Homogenizer; Next Advance, Inc.) and 50 μ L homogenate was serially diluted 10-fold in cell culture media (DMEM + 2% FBS). Confluent monolayers of Vero E6 cells in 6-well plates were infected with 400 μ L of virus-containing media for one hour with plates rocked every 10 min. The virus inoculum was then removed and 3 mL of Avicel overlay was added (1:1 mixture of 2.4% Avicel (Sigma #435244) with plaque media (2x Minimal Essential Media (Gibco): 4% FBS, 200 U/mL penicillin, 200 μ g/mL streptomycin, 1% GlutaMAX (Gibco #35050061), 20 mM HEPES) Plates were incubated at 37C with 5% CO₂ for 3 days without disturbance. Cells were then fixed in 10% formaldehyde for 30 min, washed 1x with dH₂O and stained with 1% crystal violet for 5 min. Plates were washed again with dH₂O and allowed to dry before viral plaques in each well were counted. Plaque forming units (PFU) per mL of organ homogenate and PFU per collected organ were calculated.

2.11.6 Histopathological Analysis

For histopathological analysis, fixed organ tissues were sectioned and stained with hematoxylin and eosin (H&E). The stained tissue sections were visualized under a microscope and analyzed for pathological features by an expert veterinary pathologist at Western University.

2.12 HIV-1 Infections and Infectivity Assay

HeLa-TZM-bl cells were seeded in 96-well plates (20000 cells/well) 24 hours prior to infection. TZM-bl cells, a HeLa derivative, express CD4 and CCR5 co-receptors in addition to β -galactosidase and firefly luciferase under the control of a Tat-responsive

HIV-1 long terminal repeat promoter. This approach enables quantification of infectious virus in cell culture by measurement of β -galactosidase activity. On the day of infection, cells were infected with HIV-1 AD.MDR01 at MOI 0.05 and treated with or without varying concentrations of BOLD-100. At 48 hours post-infection, β -galactosidase activity was measured in cell lysates using the Galacto-Star™ β -Galactosidase Reporter Gene Assay System (ThermoFisher).

2.13 HAdV-C5 Infections and Plaque Assay

A549 cells were seeded in 12-well plates (2×10^5 cells/well) 24 hours prior to infection. Cells were washed 1x with PBS and infected with HAdV-C5 strain Adenoid 75 (ATCC VR-5) at MOI 1 for 1 hour. Virus-containing media was removed and replaced by fresh media supplemented with BOLD-100. At 48 hours post-infection cells were collected from each well and HAdV-C5 was harvested as previously described (see “2.3 Virus Propagation”). Viral titers were determined by plaque assay. Briefly, confluent monolayers of A549 cells were infected with 400 μ L of virus-containing media for one hour with plates rocked every 10 min. The virus inoculum was then removed and 3 mL of Avicel overlay was added (1:1 mixture of 2.4% Avicel with plaque media (2x MEM, 4% FBS, 200 U/mL penicillin, 200 μ g/mL streptomycin)). Plates were incubated for 5 days at 37 °C and 5% CO₂, and subsequently fixed and stained as previously described (see “2.11.5 SARS-CoV-2 Plaque Assays”).

2.14 Statistical Analysis

All *in vitro* experiments involved at least three biological replicates.

For comparison of viral read percentage in Fig. 9, an unpaired t-test was used.

For analysis of viral load in hamster lungs and trachea (Fig. 15), a Kruskal-Wallis test was used.

For analysis of changes in hamster weight (Fig. 16), a mixed-effects ANOVA followed by Tukey’s multiple comparisons was used .

For analysis of viral load following HAdV-C5 infection (Fig. 20), one-way ANOVA followed by Holm-Šídák multiple comparisons tests was used.

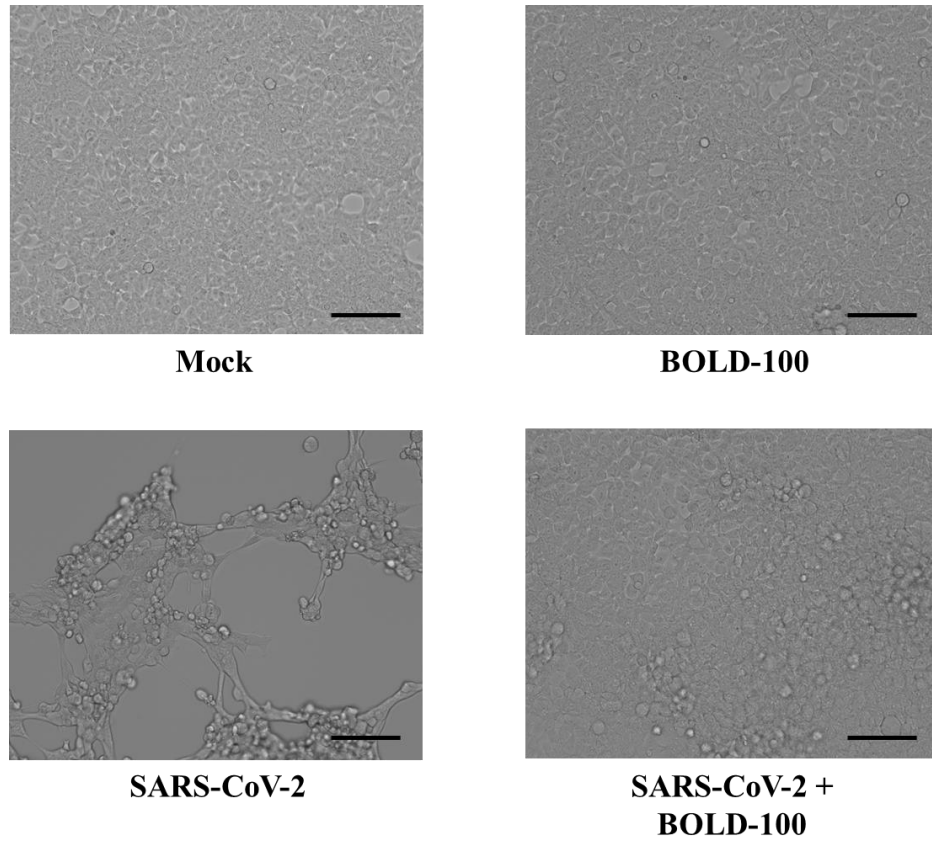
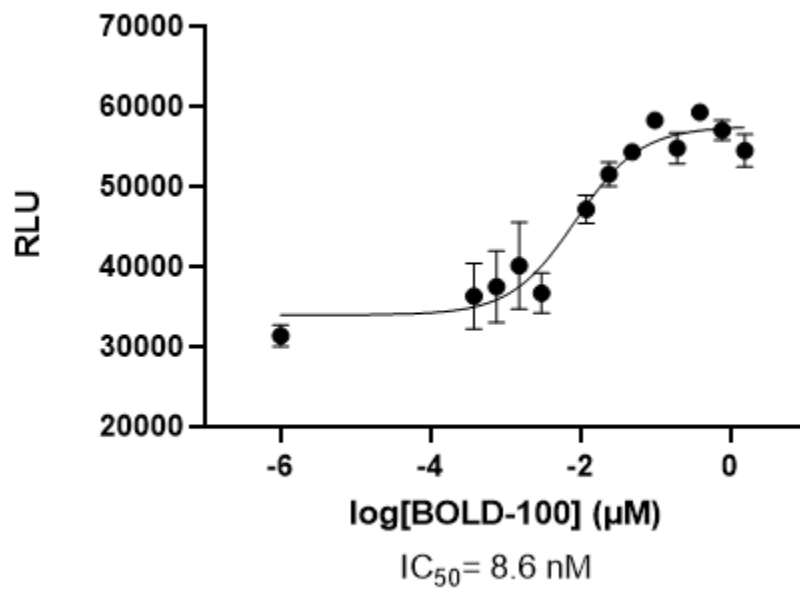
For antiviral assays, determination of the 50% inhibitory concentration (IC_{50}) was calculated by nonlinear regression (log[inhibitor] vs. response (three parameters)) using Prism v9.3.1 (GraphPad). For cytotoxicity assays, determination of the 50% cytotoxic concentration (CC_{50}) was calculated by nonlinear regression (Sigmoidal, 4PL, X is concentration) using Prism v9.3.1.

Prism v9.3.1 was used for all statistical analyses. P values less than 0.05 were deemed to be significant.

3 Chapter 3: Results

3.1 BOLD-100 Inhibits SARS-CoV-2-induced Cytopathic Effects

As an initial measure of antiviral activity, we evaluated the ability of BOLD-100 to inhibit cell death induced by SARS-CoV-2. Vero E6 cells were infected with SARS-CoV-2 at a multiplicity of infection (MOI) 0.01—a MOI which induces complete cytopathogenicity in this cell line at 72 hours post-infection in our experiments—and treated with varying concentrations of BOLD-100. At 72 hours post-infection, cell viability was examined relative to mock-treated cells. Representative brightfield microscopy images demonstrate the characteristic cytopathic effect caused by SARS-CoV-2 infection in Vero E6 cells and the protection afforded by BOLD-100 (Fig. 5A). To quantitatively assess the impact of BOLD-100 on cell survival following SARS-CoV-2 infection, we repeated this experiment and measured ATP levels in infected cells by CellTiter-Glo assay (Promega) as a surrogate measurement of viability. In this assay, the presence of ATP leads to production of luminescence by an engineered luciferase—the amount of relative light units (RLUs) produced in a well is proportional to the number of viable cells. As shown in Figure 5B, BOLD-100 exhibited a dose-dependent inhibition of SARS-CoV-2-induced cytopathic effects ($IC_{50} = 8.6 \text{ nM}$). In parallel, we used the same assay to measure the cytotoxicity of BOLD-100 in the absence of infection. At 72 hours post-treatment, cells treated with $\leq 100 \mu\text{M}$ BOLD-100 remained viable at similar levels to mock-treated cells. At $200 \mu\text{M}$ BOLD-100, approximately 51.9% of cells remained viable after 72 hours, while $\geq 400 \mu\text{M}$ BOLD-100 proved entirely cytotoxic at this timepoint (Fig. 5C). Thus, the inhibitory effects of BOLD-100 against SARS-CoV-2 occur well below the drug's toxic range. Taken together, these data show that BOLD-100 treatment protected cells from SARS-CoV-2 cytopathogenicity at nanomolar concentrations, indicating antiviral potential *in vitro*.

A**B**

C

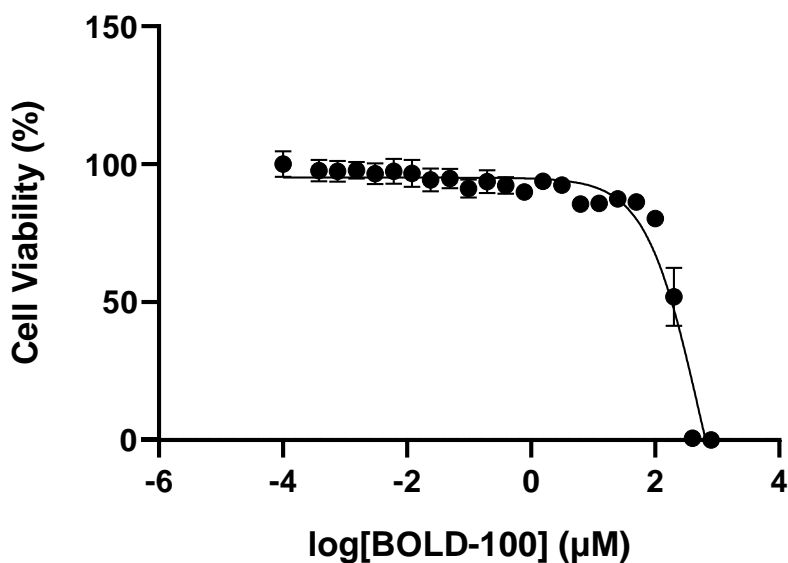


Figure 5: BOLD-100 inhibits SARS-CoV-2-induced cytopathic effects. Vero E6 cells were infected with SARS-CoV-2 (2019-nCoV/USA-WA-1/2020; “Wuhan isolate”) at MOI 0.01 and treated with varying concentrations of BOLD-100. **(A)** Representative images (20x magnification) of Vero E6 cells at 48 hours post-infection. When Vero E6 cells are infected with SARS-CoV-2, the cells lyse, break apart, and detach from the bottom of the plate. This physical change is termed cytopathic effects (CPE). Uninfected and untreated control cells are shown on the top left panel (Mock), uninfected cells treated with treated with 100 µM BOLD-100 (BOLD-100) are shown in the top right panel, untreated cells infected with SARS-CoV-2 are shown in the bottom left panel (SARS-CoV-2), and cells infected with SARS-CoV-2 and treated with treated with 100 µM BOLD-100 are shown in the bottom right panel (SARS-CoV-2 + BOLD-100). Scale bars represent 100 µM. **(B)** Relative cell viability levels were measured at 72 hours post-infection using Cell Titer Glo cell viability assay (Promega). Results are presented as mean \pm SEM of 4 independent experiments. RLU, relative light units. **(C)** Relative cell viability levels of uninfected cells treated with BOLD-100 at 72 hours post-treatment were measured using Cell Titer Glo cell viability assay. Results are presented as mean \pm SEM of 4 independent experiments.

3.2 BOLD-100 Cytotoxicity in 293T-ACE2 Cells

While Vero E6 is a practical cell line for propagation and antiviral assays with SARS-CoV-2, it is not human in origin. To strengthen the relevance of our data to future clinical applications, we chose to use human cells for subsequent experiments. We obtained human embryonic kidney 293T (HEK 293T) cells stably transduced with a lentiviral vector encoding ACE2, the receptor for SARS-CoV-2 entry. SARS-CoV-2 naturally exhibits renal tropism⁵¹⁻⁵³; therefore, the use of 293T-ACE2 cells as an infection model is justified. We sought to confirm that BOLD-100 would not induce undesirable cytotoxicity in these cells. We treated 293T-ACE2 cells with cell culture media containing varying concentrations of BOLD-100 or cell culture media with 0.1% DMSO as a mock-treated control. Forty-eight hours post-treatment, we measured relative cell viability at each BOLD-100 concentration by CCK8 assay. This analysis revealed that the 50% cytotoxic concentration (CC₅₀) of BOLD-100 in 293T-ACE2 cells is 365 μ M (Fig. 6).

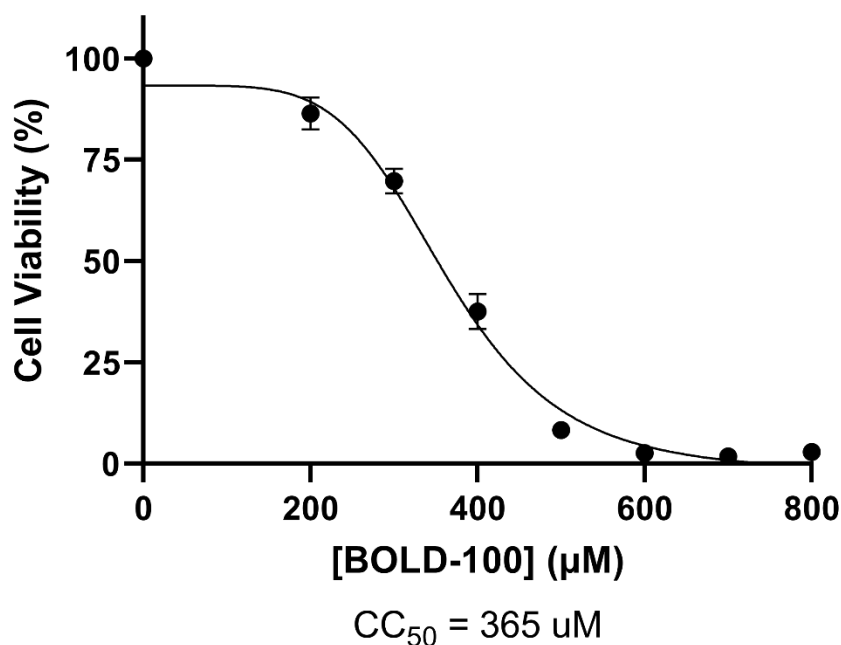


Figure 6: BOLD-100 cytotoxicity in 293T-ACE2 cells. 293T-ACE2 cells were seeded in 96-well plates (15000 cells/well) and incubated at 37°C with 5% CO₂ for 24 hours. Subsequently, cells were treated with varying concentrations of BOLD-100. Forty-eight hours post-treatment, relative cell viability was determined using CCK8 assay (Sigma) according to manufacturer's instructions. Absorbance values at 450 nm in wells containing BOLD-100-treated cells were corrected for background absorbance contributed by the cell culture medium and normalized to absorbance values in wells containing mock-treated cells to determine relative cell viability. Data represent mean ± SEM of 4 independent experiments. The 50% cytotoxic concentration (CC₅₀) was calculated by nonlinear regression (Sigmoidal, 4PL, X is concentration) using Prism v9.3.1 (GraphPad).

3.3 BOLD-100 Exhibits Dose-Dependent Inhibition of SARS-CoV-2

Given that BOLD-100 inhibited SARS-CoV-2-induced cytopathic effects, we next asked whether BOLD-100 treatment would inhibit SARS-CoV-2 replication in cell culture. Human 293T-ACE2 cells were infected with SARS-CoV-2 at MOI 0.001 for 1 hour and treated with varying concentrations of BOLD-100. At 48 hours post-infection, cell lysates were harvested and the levels of SARS-CoV-2 nucleocapsid (N) protein and RNA at each BOLD-100 concentration were measured to determine the effect of BOLD-100 on SARS-CoV-2 replication. Quantitative Western blot analysis using a monoclonal antibody directed towards N protein demonstrated that BOLD-100 treatment inhibits the intracellular accumulation of N protein in a dose-dependent manner (Fig. 7A). Likewise, RT-qPCR indicated a dose-dependent reduction of N RNA following BOLD-100 treatment ($IC_{50} = 40.5 \mu\text{M}$) (Fig. 7B). At the highest BOLD-100 concentration tested (200 μM), this effect corresponded to a 21.9-fold decrease in N protein and an 8.5-fold decrease in N RNA over the respective mock-treated controls. In concordance with our CPE protection assays, these inhibitory effects appeared at relatively non-toxic concentrations of BOLD-100. The selectivity index (SI), a measure of a drug's antiviral activity compared to its cellular toxicity, was calculated to be 9.01. Specifically, this parameter is defined as the ratio of IC_{50}/CC_{50} . Taken together, these data show that BOLD-100 inhibits the production of SARS-CoV-2 particles.

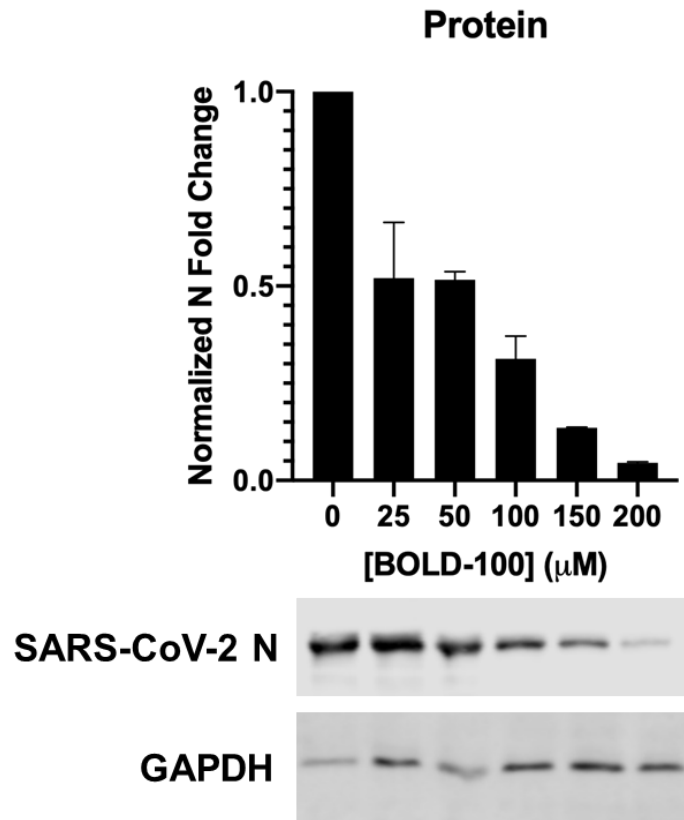
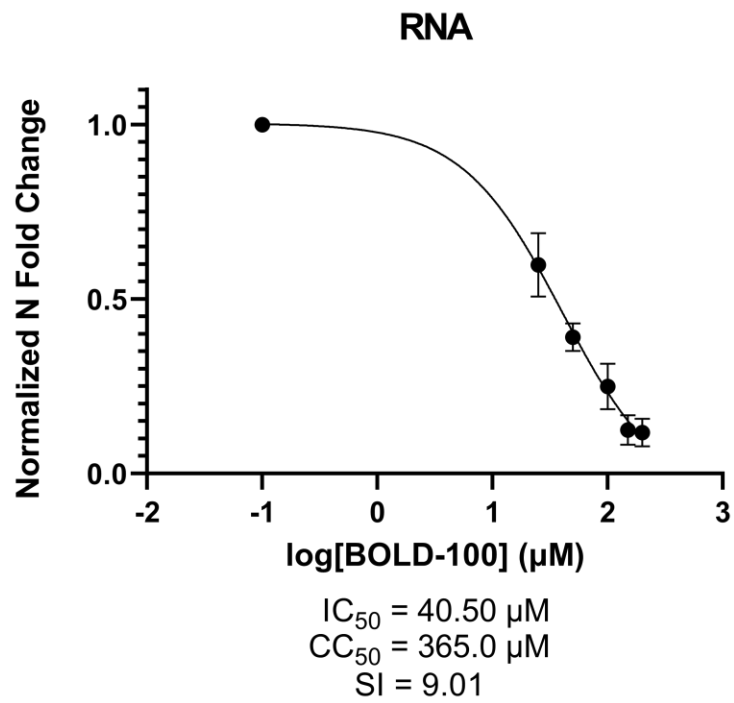
A**B**

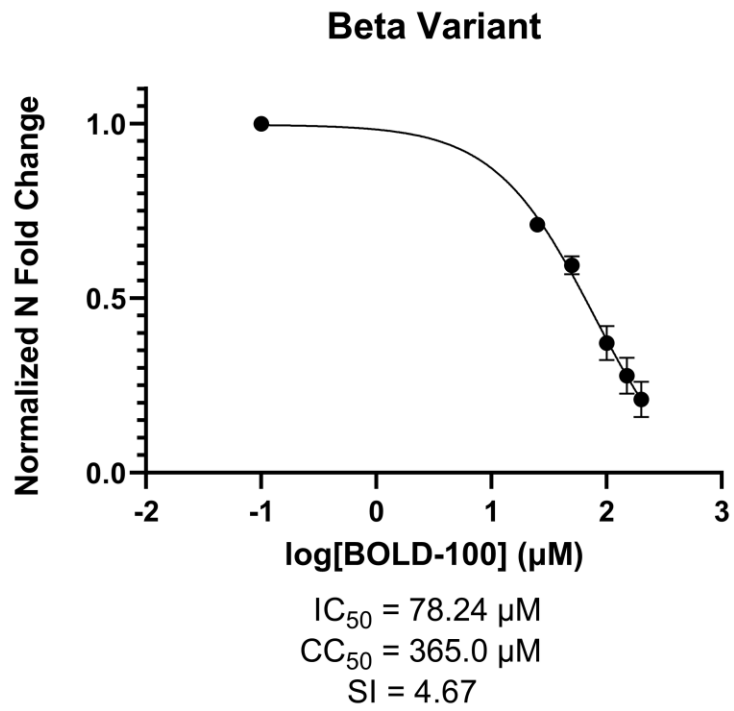
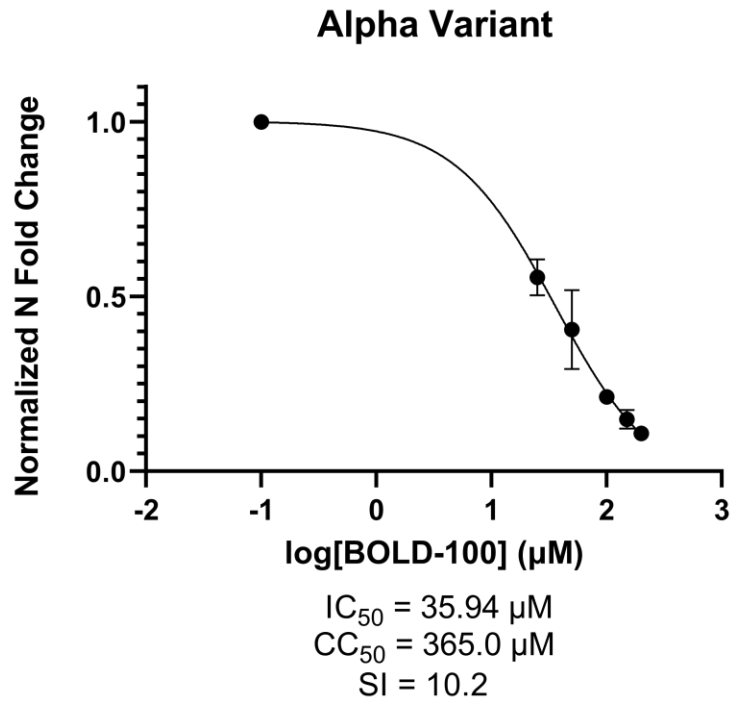
Figure 7: BOLD-100 inhibits intracellular accumulation of SARS-CoV-2 N protein and RNA. Human 293T-ACE2 cells were infected with SARS-CoV-2 (2019-nCoV/USA-WA-1/2020; “Wuhan isolate”) at MOI 0.001 and treated with varying concentrations of BOLD-100. (A) Expression of SARS-CoV-2 N protein was analyzed by separating cell lysates or clarified viral supernatants on SDS-PAGE gels followed by immunoblotting with anti-N antibodies. Band densities were quantified using ImageJ (NIH) and normalized to GAPDH as a loading control. Bars represent mean \pm SD of normalized fold change over mock. Representative Western blot of two independent experiments shown (B) Relative levels of SARS-CoV-2 N RNA were analyzed using quantitative RT-PCR and normalized to GAPDH as a loading control. Results are presented as mean \pm SEM of 3 independent experiments. IC₅₀ value was determined by nonlinear regression in Prism v9.3.1 (GraphPad).

3.4 BOLD-100 Inhibits SARS-CoV-2 Variants of Concern

As novel SARS-CoV-2 variants continued to emerge throughout 2021, we sought to confirm that BOLD-100 would retain antiviral efficacy in major variants of concern. To this end, we infected 293T-ACE2 cells with either the alpha, beta, or delta variant of SARS-CoV-2 and treated them with BOLD-100 as previously described (see 3.3 “BOLD-100 Exhibits Dose-Dependent Inhibition of SARS-CoV-2). We harvested cell lysates at 48 hours post-infection and measured SARS-CoV-2 *N* RNA levels with RT-qPCR. This analysis revealed that BOLD-100 inhibited the alpha variant at slightly lower concentrations than the ancestral strain ($IC_{50} = 35.94 \mu\text{M}$, $SI = 10.2$), while the delta variant was inhibited at concentrations slightly higher than the ancestral strain ($IC_{50} = 46.94 \mu\text{M}$, $SI = 7.78$). The IC_{50} for inhibition of the beta variant was elevated to the greatest extent among the variants tested ($IC_{50} = 78.24 \mu\text{M}$, $SI = 4.67$) (Fig. 8). The IC_{50} , CC_{50} , and corresponding SI values for BOLD-100 against each variant and the ancestral strain are described in **Table 1**. As predicted, BOLD-100 inhibited accumulation of viral RNA in cells infected with SARS-CoV-2 variants, at levels comparable to the ancestral strain for the alpha and delta variants, and at a reduced level for the beta variant.

Table 1: IC_{50} , CC_{50} , and SI values for BOLD-100 against SARS-CoV-2 variants of concern.

Variant	IC_{50} (μM)	CC_{50} (μM)	SI
Ancestral strain (“Wuhan”)	40.50	365.0	9.01
Alpha	35.94	365.0	10.2
Beta	78.24	365.0	4.67
Delta	46.94	365.0	7.78



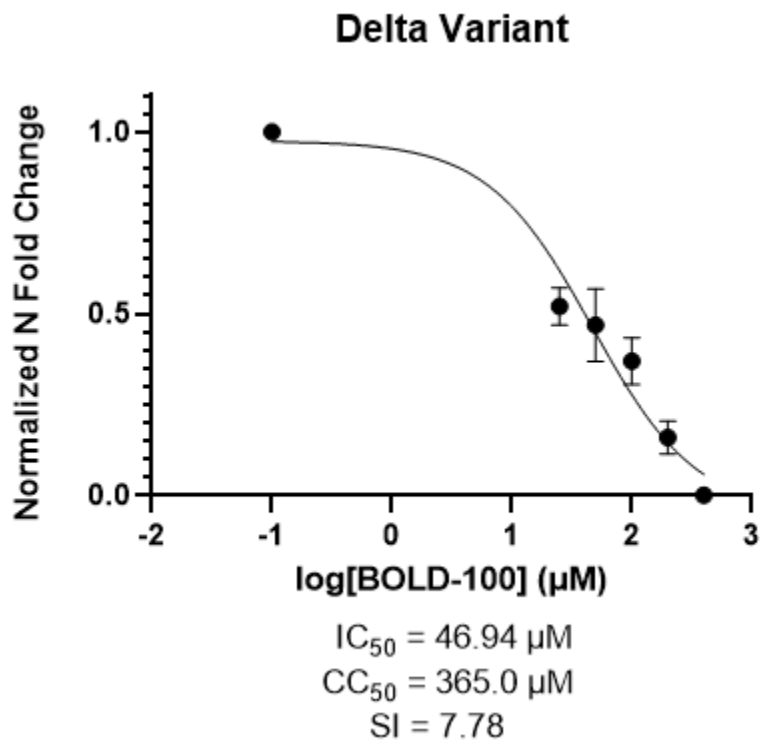


Figure 8: BOLD-100 inhibits SARS-CoV-2 variants of concern. 293T-ACE2 cells were infected with SARS-CoV-2 alpha variant, beta variant, or delta variant at MOI 0.001 for 1 hour before treatment with BOLD-100. Forty-eight hours post-infection, cell pellets were harvested. Relative levels of SARS-CoV-2 N RNA were determined by RT-qPCR and normalized to GAPDH as a loading control. Results are presented as mean \pm SEM of 3 independent experiments. IC_{50} values were determined by nonlinear regression in Prism v9.3.1 (GraphPad).

3.5 BOLD-100 Inhibits Changes in the Host Transcriptome Induced by SARS-CoV-2

As a novel antiviral therapeutic, the mechanism of action of BOLD-100 is not yet fully characterized. Previous research has suggested transcription factors as binding targets for BOLD-100; these interactions are hypothesized to contribute to drug-induced changes in gene expression¹²⁵. We sought to determine the effect of BOLD-100 treatment, SARS-CoV-2 infection, and the combination of both factors on the cellular transcriptome of 293T-ACE2 cells. Briefly, cells were mock-infected or infected with SARS-CoV-2 (MOI = 0.05) in the presence or absence of BOLD-100 (100 μ M) and incubated for 24 hours. Total RNA was then extracted from cell lysates and messenger RNA was analyzed using an RNA Sequencing approach.

We first examined the proportion of reads aligned to the SARS-CoV-2 genome under each condition to estimate viral load (Fig. 9). As expected, uninfected cells did not yield reads aligned to the SARS-CoV-2 genome. In SARS-CoV-2-infected cells, 74.2% of the total reads detected mapped to the SARS-CoV-2 genome. Interestingly, SARS-CoV-2-infected cells that were subsequently treated with BOLD-100 exhibited a marked decrease in the proportion of viral reads detected, which fell to 16.3%. These data concur with our previous findings that BOLD-100 inhibits the replication of SARS-CoV-2 in 293T-ACE2 cells.

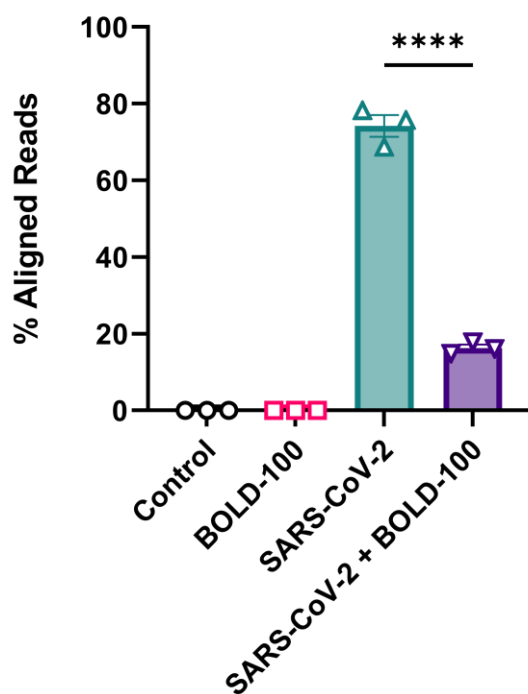
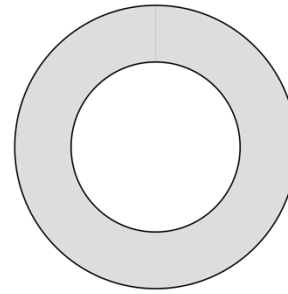
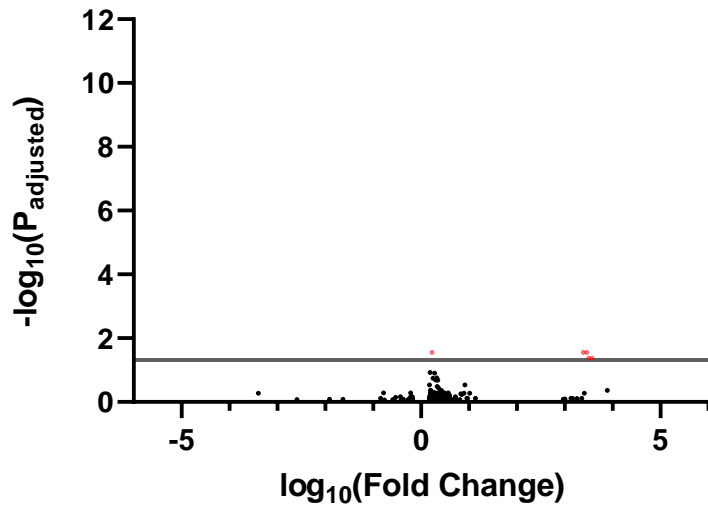


Figure 9: Proportion of SARS-CoV-2-aligned reads following SARS-CoV-2 infection and BOLD-100 treatment. 293T-ACE2 cells were infected with SARS-CoV-2 at MOI 0.05 or mock-infected for 24 hours. For cells treated with BOLD-100, 100 μ M BOLD-100 was supplemented in cell culture media. Total RNA was extracted from cells, processed for RNA sequencing, and sequenced. Sequencing reads were aligned to either the human genome or SARS-CoV-2 genome. The percentage of virus-aligned reads over total reads was calculated and is shown as mean \pm SEM. Data are representative of 3 independent experiments. ****, $P < 0.0001$ (unpaired t-test).

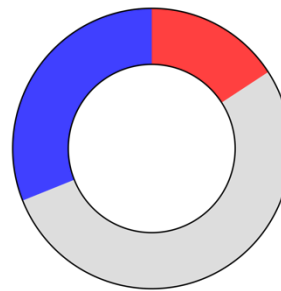
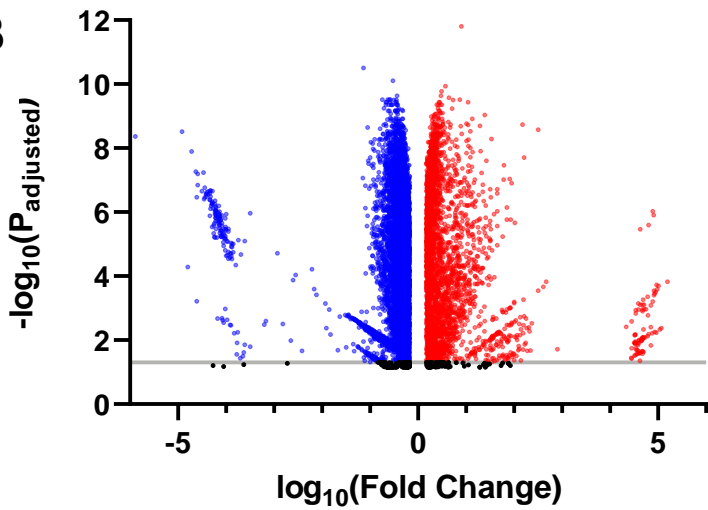
To determine the specific transcriptional effects of BOLD-100 treatment and SARS-CoV-2 infections on 293T-ACE2 cells, we performed differential gene analysis. Here, we defined genes as differentially expressed compared to control (mock-treated and mock-infected cells) if the magnitude of fold change was greater than 1.5 and if the P-value adjusted for false discovery rate was less than 0.05. This analysis indicated that BOLD-100 treatment alone does not drastically alter the cellular transcriptome, with only 0.03% of total genes detected being differentially expressed compared to the untreated control. In stark contrast, SARS-CoV-2 infection induced massive changes in the cellular transcriptome, with 46.87% of total genes detected being differentially expressed. However, in cells infected with SARS-CoV-2 and treated with BOLD-100, the percentage of genes differentially expressed was drastically reduced to 1.02% (Fig. 10).

For cells treated with BOLD-100 in the absence of SARS-CoV-2 infection, the sole genes that met the applied cutoffs of P-adjusted ≥ 0.05 and $|\text{Fold Change}| \geq 1.5$ were, in order of magnitude of upregulation, *DHRS2*, *ZNF439*, *KIAA1755*, *CABP4*, and *RP11-433J8.1*. Owing to the sheer number of genes implicated, it is a complex undertaking to capture a wide picture of the genes most strongly affected by SARS-CoV-2 infection alone. Among the genes with the highest magnitude of upregulation after infection were *ZNF334*, *FUT6*, *KLRK1*, *IRGM*, *FCAMR*, *PPP1R1B*, *GPR111*, *CABP4*, and *PIGR*. Conversely, among the genes most downregulated by SARS-CoV-2 infection were *PDF*, *HBQ1*, *LMP3*, and *SPINK2*. Differentially expressed genes in cells treated with BOLD-100 and infected with SARS-CoV-2 were largely shared with those observed in cells infected with SARS-CoV-2 alone. While no protein-coding genes were downregulated to a large extent, several were highly upregulated, including *GOLGA6B*, *FUT6*, *KLRK1*, *FCAMR*, *CABP4*, and *LTA*. Of interest, *CABP4* was significantly upregulated by BOLD-100 treatment alone, SARS-CoV-2 infection alone, and the combination of the two. A list of the top 50 differentially expressed genes under each condition may be found in **Appendix A**.

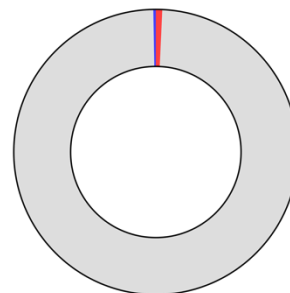
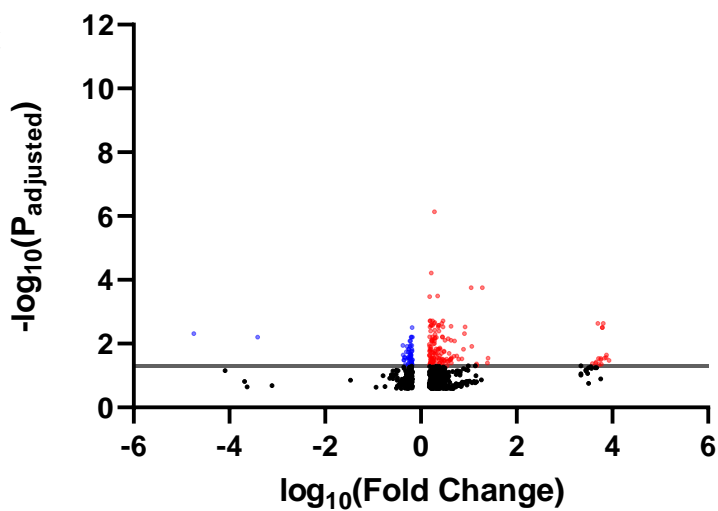
We then analyzed enriched Gene Ontology (GO) terms under each condition to obtain a broader picture of which key cellular pathways were impacted by SARS-CoV-2 infection and BOLD-100 treatment. GO is a classification system that groups genes by their general and specific functions. For this analysis, to obtain a broader picture of the cellular pathways impacted by BOLD-100, we chose a less stringent cutoff of $|\text{Fold Change}| \geq 1.5$ and unadjusted P-value < 0.05 . Among the high-level GO terms most highly enriched by SARS-CoV-2 infection at the biological process level was “immune system process” (Fig. 11A). Within this category, SARS-CoV-2 infection enriched terms related to leukocyte migration and activation, as well as the broader immune response (Fig. 11B). To explore the specific impact of infection and drug treatment on these gene categories, we analyzed expression of genes involved in the Type 1 IFN response, cytokine signalling, and chemotaxis. Consistent with previous reports in human primary bronchial epithelial cells⁶⁶, gene enrichment analyses illustrate a generally diminished IFN-I signaling biology for SARS-CoV-2 overall, though certain IFN-induced factors were nonetheless highly upregulated. Several key IFN-induced host restriction factors including *BST2*/tetherin, interferon-induced transmembrane proteins (IFITMs), and other antiviral genes such as *IFI6* and *IFIT1* were downregulated by SARS-CoV-2. Strikingly, expression of these genes was restored to control levels in the presence of BOLD-100 (Fig. 12A). Likewise, various cytokines and chemokines involved in the immune response were downregulated by SARS-CoV-2 infection, including *CXCL12* and *CXCL16*, which activate and attract leukocytes respectively, and the pro-inflammatory cytokine *MIF* (Fig. 12B). However, the converse pattern was also observed in some cases, in which pro-immune cytokines and effector genes such as *CXCL11*, *IL16*, *GBP2*, *TNFSF11*, and *LTA* were strongly upregulated by SARS-CoV-2 infection—as before, BOLD-100 treatment restored expression of these genes to baseline levels. As expected based on our previous analyses, BOLD-100 treatment in the absence of virus did not transcriptionally regulate these factors. Taken together, BOLD-100 inhibits replication of SARS-CoV-2, which accompanies disruption of virus-induced transcriptional changes in physiologically relevant areas.

BOLD-100**A**

■ Upregulated (0.03%)
■ Unaffected (99.97%)
■ Downregulated (0.00%)

SARS-CoV-2**B**

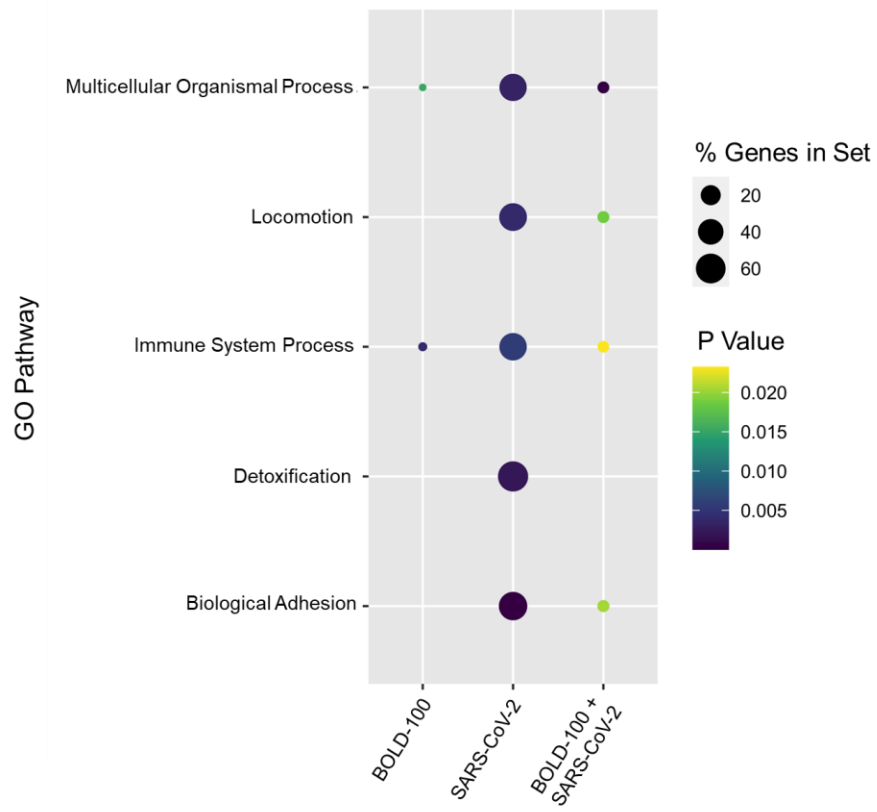
■ Upregulated (15.81%)
■ Unaffected (53.13%)
■ Downregulated (31.06%)

BOLD-100 + SARS-CoV-2**C**

■ Upregulated (0.73%)
■ Unaffected (98.98%)
■ Downregulated (0.29%)

Figure 10: Transcriptional profile of 293T-ACE2 cells following BOLD-100 treatment and/or SARS-CoV-2 infection. 293T-ACE2 cells were infected with SARS-CoV-2 at MOI 0.05 or mock-infected for 24 hours. For cells treated with BOLD-100, 100 μ M BOLD-100 was supplemented in cell culture media. Total RNA was extracted from cells, processed for RNA sequencing, and sequenced. Gene read counts for each treatment were normalized by the counts per million method. Data were compared to mock-treated and mock-infected control cells for **(A)** cells treated with BOLD-100 and mock-infected, **(B)** cells infected with SARS-CoV-2 and mock-treated, and **(C)** cells treated with BOLD-100 and infected with SARS-CoV-2. Differentially expressed genes (p-adjusted < 0.05) with absolute fold change ≥ 1.5 are indicated in blue (downregulated genes) and red (upregulated genes). Horizontal line illustrates threshold where p-adjusted = 0.05. Pie charts represent proportion of upregulated and downregulated genes (P <0.05) under each condition. Data are representative of 3 independent experiments.

A



B

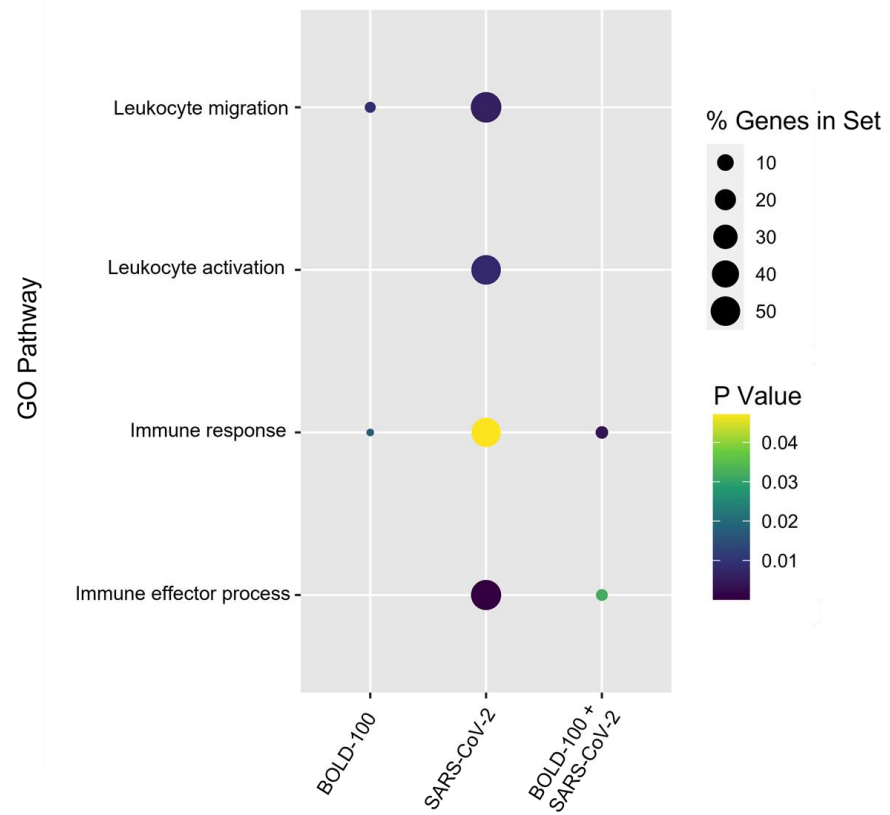


Figure 11: Dotplot visualization of enriched GO terms following SARS-CoV-2 infection and/or BOLD-100 treatment in 293T-ACE2 cells. 293T-ACE2 cells were infected with SARS-CoV-2 at MOI 0.05 or mock-infected for 24 hours. For cells treated with BOLD-100, 100 μ M BOLD-100 was supplemented in cell culture media. Total RNA was extracted from cells, processed for RNA sequencing, and sequenced. Gene read counts for each treatment were normalized by the counts per million method. Genes with absolute fold change ≥ 1.5 and $P < 0.05$ compared to mock-treated and mock-infected cells were included. Data were analyzed for GO terms significantly enriched by SARS-CoV-2 infection (**A**) at the biological processes level (GO:0008150) and (**B**) under the “immune system process” category (GO:0002376). Data are representative of 3 independent experiments.

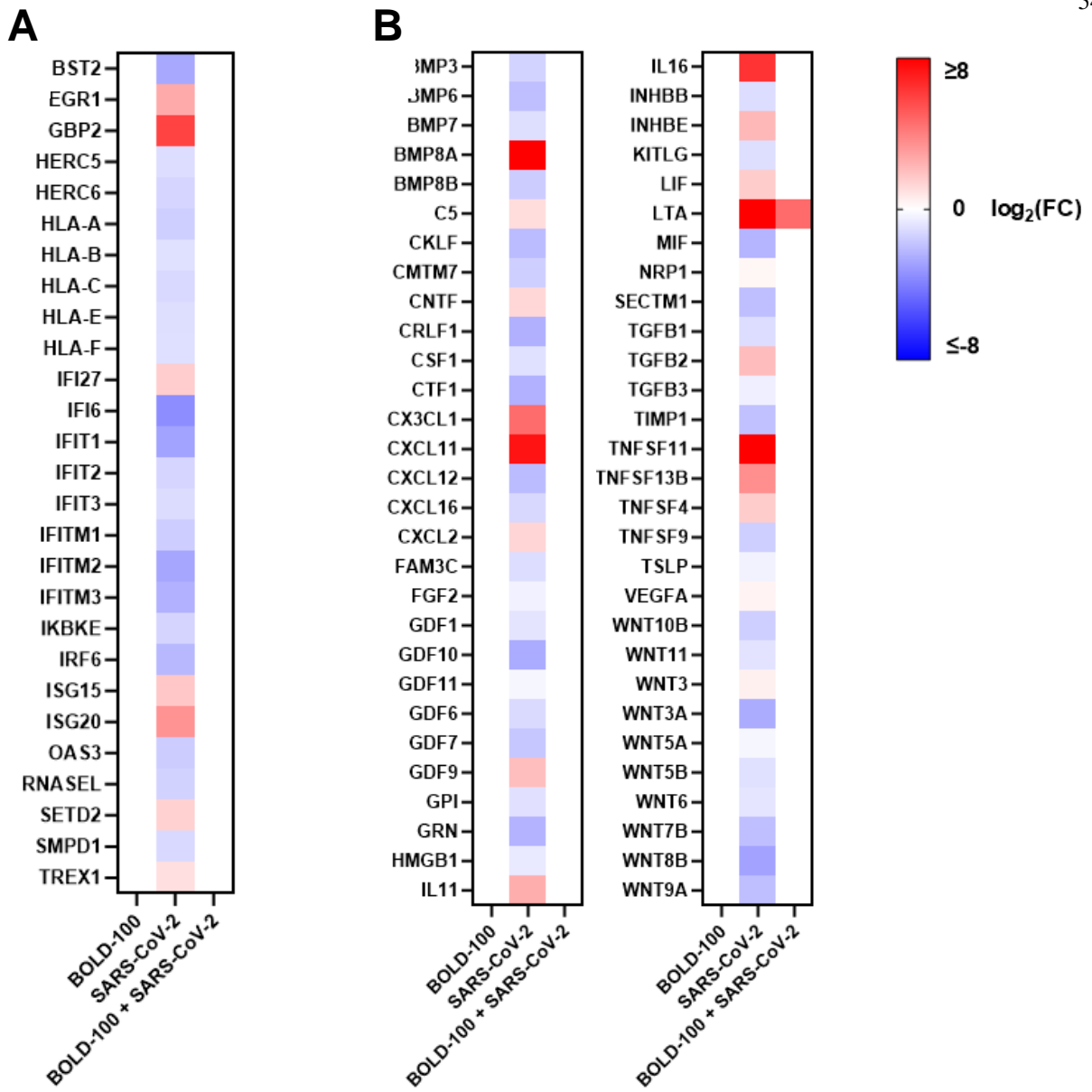


Figure 12: Heat maps of differentially expressed genes following SARS-CoV-2 infection and/or BOLD-100 treatment in 293T-ACE2 cells. 293T-ACE2 cells were infected with SARS-CoV-2 at MOI 0.05 or mock-infected for 24 hours. For cells treated with BOLD-100, 100 μM BOLD-100 was supplemented in cell culture media. Total RNA was extracted from cells, processed for RNA sequencing, and sequenced. Gene read counts for each treatment were normalized by the counts per million method. Genes with absolute fold change ≥ 1.5 and $P < 0.05$ compared to mock-treated and mock-infected cells were included. Heat maps depict DEGs induced by SARS-CoV-2 infection under the GO datasets for (A) response to type I interferon (GO:0034340) and (B) cytokine activity and chemokine activity (GO:0005125, GO:0008009). Legend depicts the \log_2 -transformed fold change of DEGs, with upregulated genes shown in red and downregulated genes shown in blue. Data are representative of 3 independent experiments.

3.6 Determining the Maximum Tolerated Dose of BOLD-100 in Syrian Hamsters

To inform BOLD-100 dosage in subsequent experiments, we conducted a dose-escalation study to determine the maximum tolerated dose (MTD) of BOLD-100 in hamsters. The following doses were evaluated: 0 mg/kg (citrate-buffered saline vehicle alone), 5 mg/kg, 10 mg/kg, 12.5 mg/kg, 15 mg/kg, 30 mg/kg, 50 mg/kg, and 75 mg/kg. An upper limit of 75 mg/kg was selected based on prior studies of BOLD-100 in mice performed by Bold Therapeutics, Inc.

BOLD-100 was determined to be toxic in hamsters at doses of 30 mg/kg and above. Hamsters treated at 30 mg/kg, 50 mg/kg, and 75 mg/kg either succumbed to drug toxicity or were euthanized due to clinical decline within 48 hours of administration. None of the hamsters exhibited signs of fever or infection, and the vehicle-treated hamster remained healthy over the course of the study (Fig. 13A). Histopathological analysis revealed acute renal injury characterized by obstructive nephropathy. Renal lesions consisted of diffuse tubular ectasia with proteinosis and multifocal cortical renal mineralization (Fig. 13B). With the exception of one hamster in the 75 mg/kg cohort—which exhibited necrotizing enteropathy—no drug-related lesions were identified in any hamsters for the intestines, heart, pancreas, lung, liver, and adrenal gland.

Hamsters treated with BOLD-100 at doses of 15 mg/kg and below remained healthy for 7 days post-treatment, after which the study concluded. There was no observable drug-induced toxicity or weight loss, and histopathologic analysis did not identify any drug-related lesions in organ tissues (Fig. 13C). Thus, the MTD of BOLD-100 in Syrian hamsters was determined to be 15 mg/kg.

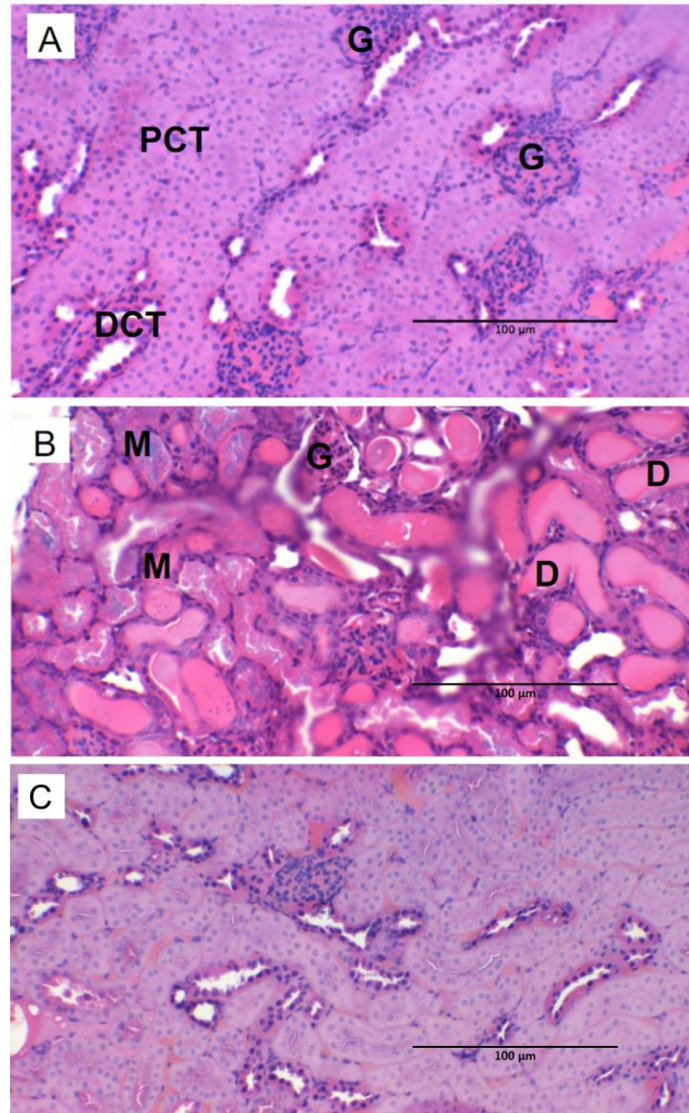


Figure 13: Normal expected renal features compared to abnormal kidney, cortex, H&E 20x objective. (A) Kidney of mock-treated hamster appears normal: glomeruli (G), proximal collecting tubule (PCT), distal collecting tubule (DCT). (B). Representative image of abnormalities observed in hamsters treated with 30, 50 or 75 mg/kg BOLD-100. Image shows kidney section from a hamster treated with 50 mg/kg BOLD-100. Affected kidneys characterized by dilated tubules filled with proteinaceous material (D) and mineralization (M). Glomeruli (G) are compressed. (C) Representative renal cortex of hamsters treated with 5, 10, 12.5, or 15 mg/kg. Image shows kidney section from a hamster treated with 10 mg/kg BOLD-100. Renal tubules, ducts, and glomeruli have no apparent abnormalities. Scale bars in all panels represent 100 µm.

3.7 Establishment of a Syrian Hamster Model of COVID-19

To establish our hamster model of COVID-19, we conducted a pilot study to i) confirm the infectious dose of SARS-CoV-2 required to induce clinical disease, ii) verify the presence of infectious virus and pathological features in lung tissue, and iii) evaluate the potential for compounding toxicity between SARS-CoV-2 infection and BOLD-100 treatment.

Four 4-6-week-old male Syrian hamsters were infected intranasally with 1×10^3 PFU SARS-CoV-2—of these hamsters, 3 were treated intravenously with 10 mg/kg BOLD-100, while one hamster received citrate-buffered saline vehicle alone as an untreated control. One hamster from the drug-treated group was euthanized on Day 2, 4, and 6 post-infection to monitor viral load in the lungs at each time point. The mock-treated control hamster was euthanized on Day 6 post-infection. Hamsters were weighed daily until sacrifice, after which viral load and pathological features in the lungs were determined by plaque assay. Robust viral replication was detected in the lungs of infected animals, with highest titres detected on Day 2 post-infection, and declining thereafter (Fig. 14A). However, given our small sample size, we elected to sacrifice hamsters in further experiments on Day 4 post-infection, which is more widely supported in the literature to be the peak of viral replication in this model^{81,85,87}. Weight loss was minimal, limiting its use as a parameter to assess clinical disease (Fig. 14B). Histological analysis confirmed the presence of pulmonary lesions at each timepoint post-infection, consistent with acute injury. These lesions were generally characterized by congestion or bronchiolar epithelial cell blebbing and sloughing with inflammatory cells (Fig. 14C).

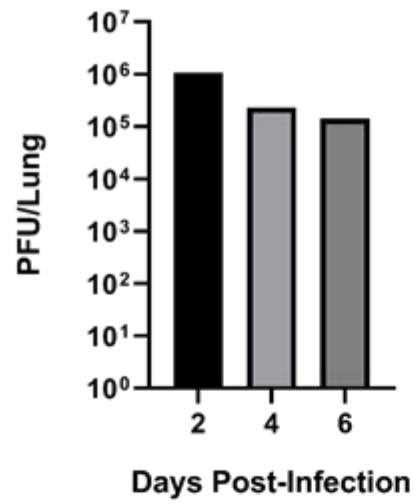
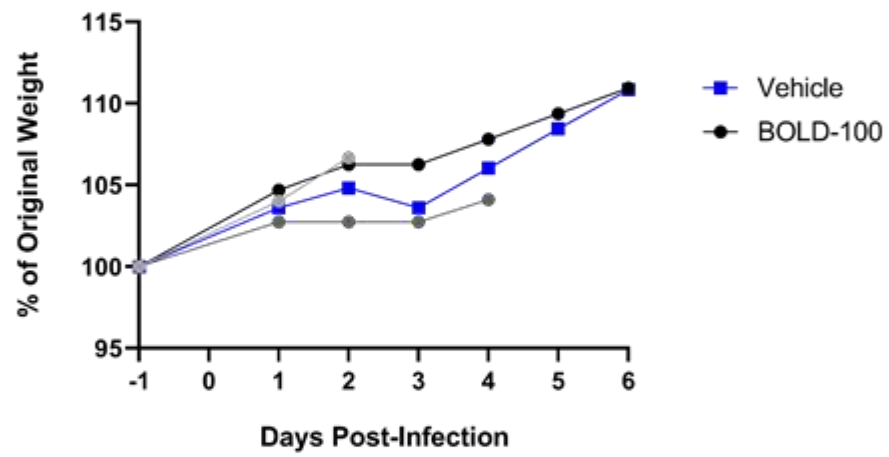
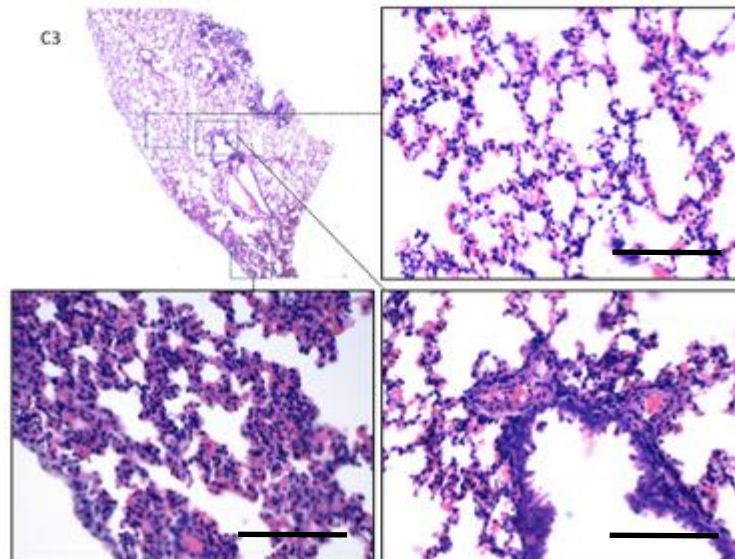
A**B****C**

Figure 14: Establishment of a Syrian hamster model of COVID-19. Four Syrian hamsters were infected intranasally with 1×10^3 PFU SARS-CoV-2. One hour prior to infection, hamsters were treated with 10 mg/kg BOLD-100 or vehicle alone. One drug-treated hamster was euthanized on Day 2, 4, and 6 post-infection. **(A)** Viral load in left lung lobe was determined by plaque assay. Each bar represents data from one hamster. **(B)** Change in weight for all hamsters over duration of study. Each connected set of points represents one hamster. **(C)** Representative image of H&E-stained lung sections from infected and drug-treated hamsters. Top left image was captured at 4x magnification, while zoomed-in sections were captured at 40x magnification. Image depicts bronchiolar epithelial blebbing and sloughing with few intraalveolar inflammatory infiltrates. Scale bars represent 100 μm .

3.8 Determining the Ability of BOLD-100 to Inhibit COVID-19 Progression in a Syrian Hamster Model

Subsequently, we evaluated the ability of BOLD-100 to inhibit viral replication and ameliorate clinical disease in our hamster model of COVID-19. Hamsters were infected intranasally with 10^3 PFU SARS-CoV-2 and treated intravenously with vehicle alone or 15 mg/kg BOLD-100 either 24 hours prior to infection (Day -1), one hour prior to infection (Day 0), or 24 hours post-infection (Day +1) This approach permitted us to examine whether BOLD-100 would need to be biologically distributed before infection to exert antiviral effects, and whether it would inhibit viral replication when administered post-infection, which is a more clinically relevant scenario. The BOLD-100 MTD of 15 mg/kg was chosen as the experimental dose to maximize drug effect. On Day 4 post-infection, lungs and trachea were harvested for determination of viral load and histopathology.

Compared to vehicle-treated controls, hamsters treated with BOLD-100 24 hours prior to infection exhibited a 0.61-log_{10} decrease in median lung viral load and a 0.78-log_{10} increase in median trachea viral load. Comparatively, hamsters treated with BOLD-100 1 hour prior to infection demonstrated a 0.30-log_{10} and 0.53-log_{10} reduction in median viral load for lungs and trachea respectively (Fig. 15). Conversely, hamsters treated with BOLD-100 24 hours post-infection exhibited a median increase in viral load in both organs, corresponding to a 0.63-log_{10} and 1.47-log_{10} increase in the lungs and trachea respectively. However, none of these differences were statistically significant (Kruskal-Wallis test, $P > 0.05$). Taken together, infectious viral titre in the lungs and trachea did not significantly decrease between vehicle- and drug-treated hamsters in all treatment groups, irrespective of time of drug administration.

Across all treatment groups, clinical signs of disease such as lethargy and respiratory distress were minimal and little-to-no weight loss was observed (Fig. 16). At time of sacrifice, all hamsters save one, which was in the Day +1 treatment group, had gained weight compared to baseline on the day of infection. Overall, there were no significant differences in weight loss between treatment groups at any timepoint throughout the

study (Mixed-effects ANOVA and Tukey's multiple comparisons tests, $P > 0.05$) (Fig. 16).

The major pathological changes in hamster lungs following SARS-CoV-2 infection are well characterized in the literature, often involving inflammation of the bronchioles and luminal infiltration of immune cells and cellular debris. We asked whether BOLD-100 treatment at the previously indicated timepoints would ameliorate these pathological features in our Syrian hamster model. The pulmonary lesions that we observed generally reflected a mild-to-moderate bronchiolitis with exudate involving aggregates of cellular debris, degenerate cells, and red blood cells alongside diffuse peribronchiolar inflammatory cell infiltrates, including lymphocytes, neutrophils, and few plasma cells. These lesions affected 2/3 of hamsters in each drug treatment group and in the control group. The remaining hamster in each treatment group did not exhibit significant lesions in pulmonary tissue. Thus, there was no relative difference in abundance of pathological features between mock-treated and BOLD-100-treated hamsters, irrespective of the time of drug administration (Table 2, Fig. 17). While the observed pathological features were relatively consistent among affected animals, one hamster in the Day -1 treatment group exhibited locally extensive intra-alveolar hemorrhage, a feature that was absent in other animals. A complete list of histopathological features in the lungs of each hamster is described in **Table 2**. Across the control and drug-treated groups, no hamsters exhibited pathological lesions in kidneys, heart, spleen, adrenal gland, esophagus, thyroid, and pancreas. Pathological differences in trachea tissue were unable to be compared due to complications in tissue processing and slide preparation. Overall, histologic analysis of organ tissues did not support a role for BOLD-100 in improving pathological features of disease.

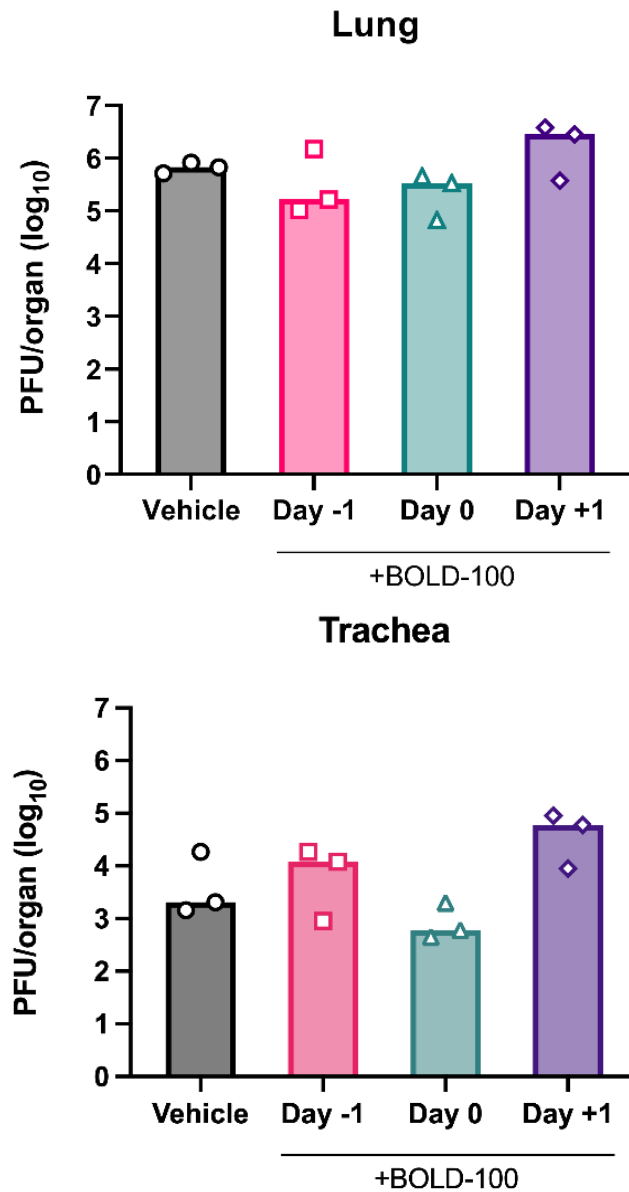


Figure 15: Viral load in lungs and trachea in hamsters treated with BOLD-100 and infected with SARS-CoV-2. Syrian hamsters were infected with 1×10^3 PFU SARS-CoV-2 and treated with vehicle or BOLD-100 (15 mg/kg) either 24 hours before infection (Day -1), one hour before infection (Day 0), or 24 hours post-infection (Day +1). Hamsters were euthanized 4 days post-infection. Viral load in left lung lobe or whole trachea was determined by plaque assay. Results are presented as plaque forming units per organ in lungs and trachea in each animal (N = 3 per treatment group). Bars represent median per treatment group. No significant differences detected between groups for lungs or trachea (Kruskal-Wallis test, $P > 0.05$)

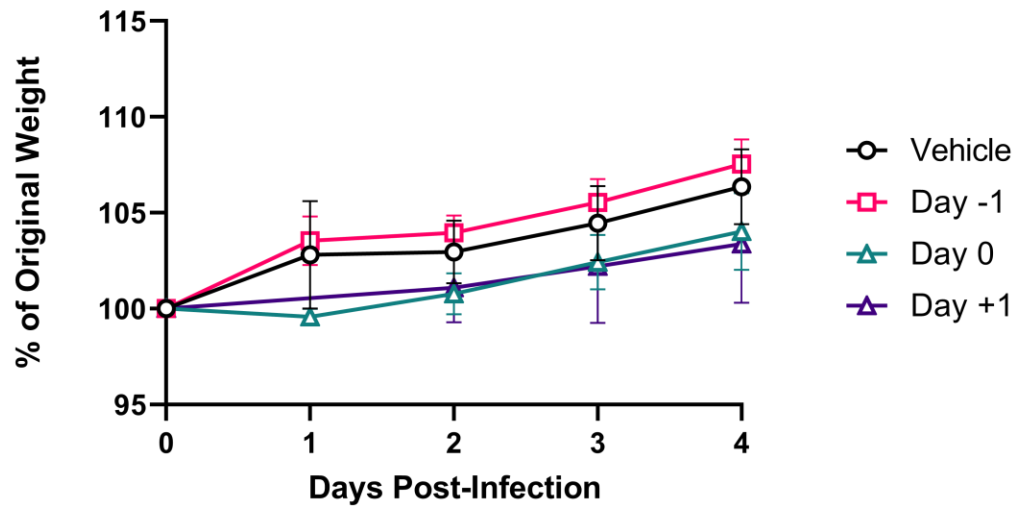


Figure 16: Change in weight in hamsters treated with BOLD-100 and infected with SARS-CoV-2. Hamsters in Figure 15 were weighed daily until euthanasia. Results are presented as percentage of original weight, as measured on the day of infection. Mean \pm SEM is shown (N = 3 hamsters per treatment group). No significant difference in weight change between groups at any study timepoint (Mixed-effects ANOVA followed by Tukey's multiple comparisons test, $P > 0.05$).

Table 2: Histopathological features detected in the lungs of Syrian hamsters infected with SARS-CoV-2 in the presence and absence of BOLD-100 treatment.

Treatment Group	Hamster #	Pathological Observations in Lung
Vehicle	1	Bronchiolar lumina contain small aggregates of red blood cells (hemorrhage), cellular debris, and scant fibrin. There is occasional bronchial epithelial cell necrosis with rare intracytoplasmic viral inclusion bodies.
	2	Few bronchiolar lumina contain small aggregates of cellular debris, degenerate cells, and red blood cells. There are diffuse peribronchiolar inflammatory cell infiltrates, which include lymphocytes, neutrophils, and few plasma cells.
	3	No significant lesions.
BOLD-100 Day -1	4	Partial bronchiole contains aggregates of cells, largely degenerate, mixed with red blood cells and small amounts of fibrin.
	5	No significant lesions.
	6	Few bronchiolar lumina contain small aggregates of cellular debris, degenerate cells, and red blood cells. There are diffuse peribronchiolar inflammatory cell infiltrates, which include lymphocytes, neutrophils, and few plasma cells.
BOLD-100 Day 0	7	Locally extensive intra-alveolar hemorrhage. Alveoli are filled with blood. Due to absence of reactive changes, blood represent hemorrhage peri- or post-mortem. Intra-alveolar macrophages are few.
	8	Alveolar septae are closely apposed with minimal distinction interrupted by narrow angular clefts (atelectasis or artifact). Angular spaces are more prominent along the tissue periphery. There is increased cellularity within alveolar septae. There are multiple cellular degenerate aggregates mixed with red blood cells within bronchiolar lumen.
	9	No significant lesions.
BOLD-100 Day +1	10	Bronchiolar lumina contain small aggregates of cellular debris, degenerate cells, and red blood cells.

		There is occasional single cell necrosis within the mucosal epithelium. There are diffuse peribronchiolar inflammatory cell infiltrates, which include lymphocytes, neutrophils, and few plasma cells.
	11	Bronchiolar lumina contain small aggregates of cellular debris, extravasated red blood cells, occasionally associated with epithelium. There are a few epithelial cell necroses. There are diffuse peribronchiolar inflammatory cell infiltrates, which include lymphocytes, neutrophils, and few plasma cells.
	12	No significant lesions.

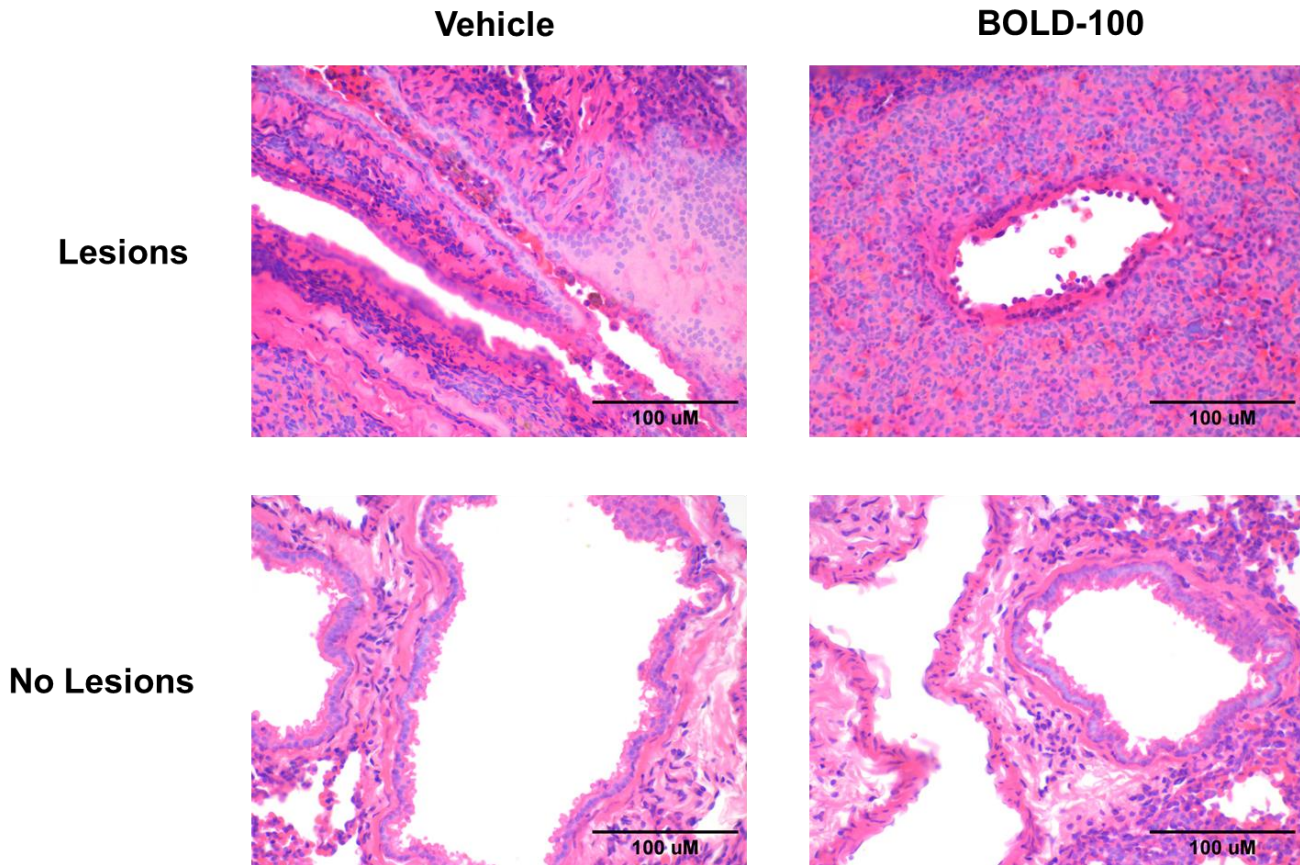


Figure 17: Representative lung sections from hamsters infected with SARS-CoV-2, H&E, 40x objective. Images illustrate bronchiolitis with intraluminal exudate (“Lesions”), which was present in 75% of hamsters in both vehicle and drug-treated groups. Images of lung sections with no pathological features (“No Lesions”), which represent the remaining hamster in each treatment group, are shown for comparison. Images representing drug treatment (BOLD-100) are characteristic of all drug-treated groups (Day -1, Day 0, Day +1). Scale bars represent 100 μm.

3.9 Antiviral Activity of BOLD-100 in Additional Viral Infection Models

We then asked whether the antiviral activity of BOLD-100 was specific to SARS-CoV-2, or whether the drug would inhibit additional viruses of public health concern. To this end, we tested BOLD-100 in cell culture models of Human Immunodeficiency virus type 1 (HIV-1) and Human Adenovirus type 5 (HAdV-C5).

3.9.1 BOLD-100 Inhibits HIV-1 Replication

Human Immunodeficiency virus 1 (HIV-1) is a retrovirus that is the causative agent of the Acquired Immunodeficiency Syndrome (AIDS) epidemic. HIV-1 infects CD4⁺ T cells among other immune cells, leading to the depletion of these cells and a subsequent deficiency in cellular immunity^{149,150}. As an initial measure of the potential of BOLD-100 as an antiviral against HIV-1, we evaluated its ability to inhibit viral replication *in vitro*. We infected HOS CD4⁺ CXCR4⁺ cells — a human osteosarcoma cell line that overexpresses CD4 and CXCR4 as an HIV-1 receptor and co-receptor respectively — with replication-competent HIV-1 R9 for 48 hours in the presence and absence of BOLD-100 treatment. Subsequently, we quantified the relative abundance of viral particles released into the supernatant by RT-qPCR. As expected, cells infected with HIV-1 R9 in the absence of BOLD-100 treatment readily released HIV-1 particles into the supernatant. In contrast, cells treated with increasing concentrations of BOLD-100 up to 100 μ M released substantially less viral particles in a dose-dependent manner. Linear regression analysis revealed an IC₅₀ value of 8.912 μ M (Fig. 18A). Concurrently, we measured the cytotoxicity of BOLD-100 treatment alone in HOS CD4⁺ CXCR4⁺ cells by CCK8 assay (Fig. 18B) (CC₅₀ = 347.9 μ M, SI = 39.0).

Cells infected with HIV-1 produce both infectious and non-infectious viral particles^{151,152}. We asked whether BOLD-100 would inhibit the production of infectious virus, and whether it holds potential against drug-resistant strains of HIV-1. We infected TZM-bl cells with HIV-1 AD.MDR01, a subtype B clone associated with rapid disease progression and resistance to existing HIV therapeutics. TZM-bl cells, a HeLa derivative, express CD4 and CCR5 co-receptors in addition to β -galactosidase and firefly luciferase

under the control of a Tat-responsive HIV-1 long terminal repeat promoter. When these cells are infected with HIV-1, the incoming Tat protein activates expression from the LTR-containing reporter construct. This approach enables quantification of infectivity in cell culture by measurement of β -galactosidase activity. Cells were infected in the presence of BOLD-100 for 48 hours, after which β -galactosidase activity was measured. BOLD-100 treatment inhibited infectious virus production in a dose-dependent manner (Fig. 19A) ($IC_{50} = 29.68 \mu M$). In parallel, we measured the cytotoxicity of BOLD-100 treatment alone in TZM-bl cells (Fig. 19B) ($CC_{50} = 235.6 \mu M$, $SI = 7.94$).

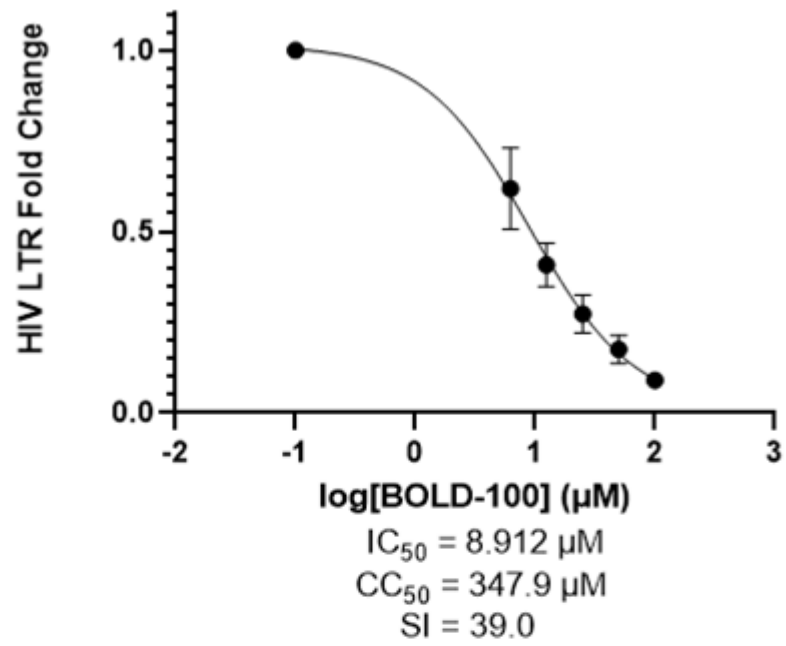
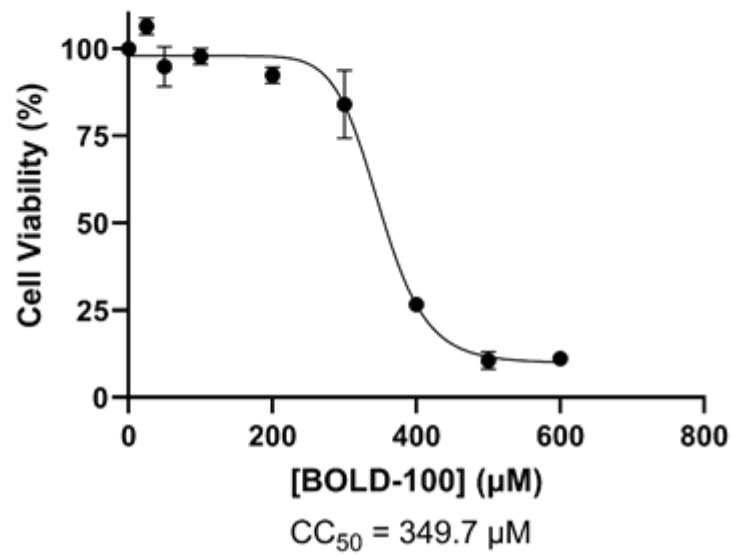
A**B**

Figure 18: BOLD-100 inhibits production of HIV-1 viral particles in a dose-dependent manner. (A) Human HOS CD4⁺ CXCR5⁺ were infected with replication-competent HIV-1 R9 at MOI = 0.2 for 1 hour. Subsequently, cells were treated with varying concentrations of BOLD-100 and incubated for 48 hours. Virus-containing supernatants were collected from infected cells and analyzed for levels of the HIV-1 (LTR) using quantitative RT-PCR. IC₅₀ was calculated by nonlinear regression (log[inhibitor] vs. response (three parameters)) using Prism v9.3.1 (GraphPad). Data are presented as mean ± SEM of fold change over diluent-treated controls, and are representative of 4 independent experiments (B) Cytotoxicity: Uninfected HOS CD4⁺ CXCR4⁺ cells were treated with varying concentrations of BOLD-100. Forty-eight hours post-treatment, relative cell viability was determined using CCK8 assay (Sigma) according to manufacturer's instructions. Data represent mean ± SEM of 4 independent experiments. CC₅₀ was calculated by nonlinear regression (Sigmoidal, 4PL, X is concentration) using Prism v9.3.1 (GraphPad).

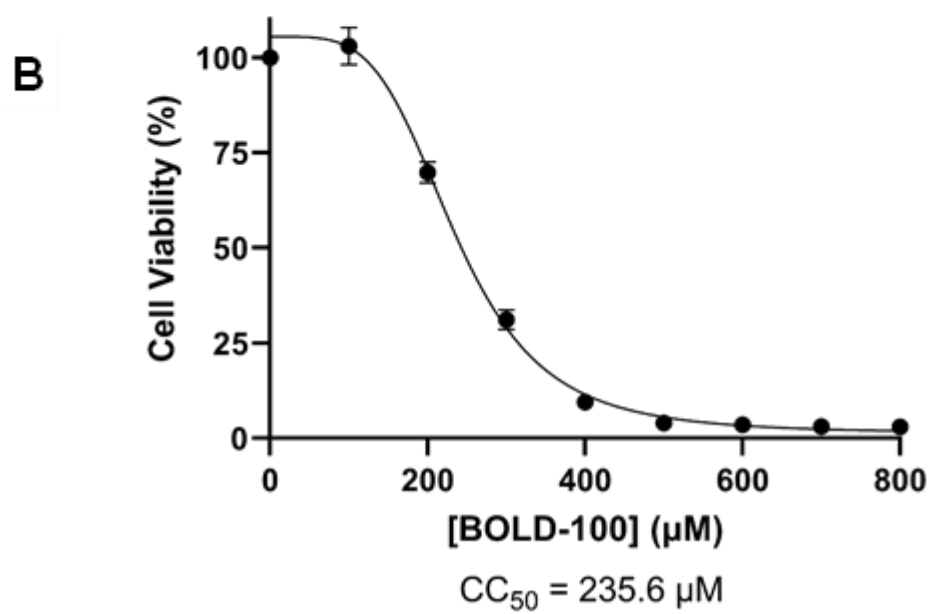
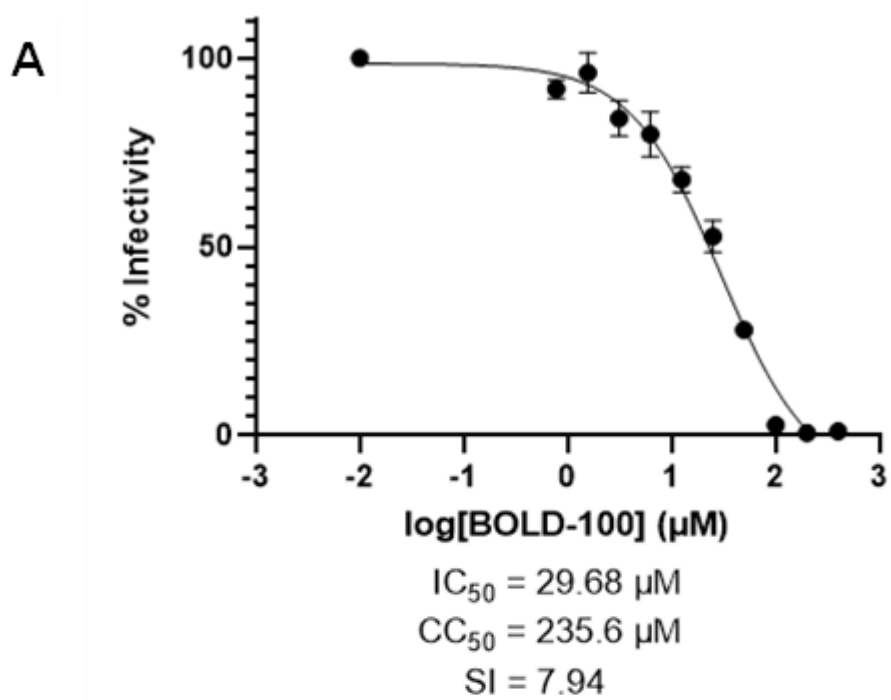
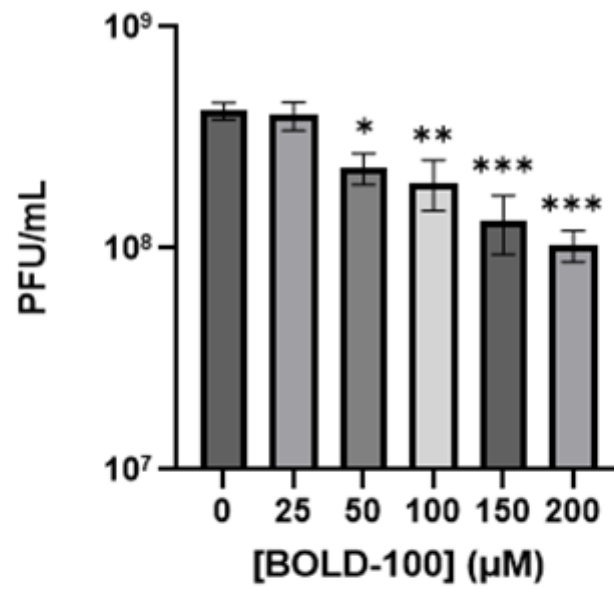


Figure 19: BOLD-100 inhibits replication of infectious HIV-1 in a dose-dependent manner. (A) TZM-bl cells were infected with HIV-1 strain AD.MDR01 (MOI = 0.05) and treated with or without varying concentrations of BOLD-100. This MOI permits robust detection of infection after 48 hours. At 48 hours post-infection, β -galactosidase activity was measured in cell lysates using the Galacto-Star™ β -Galactosidase Reporter Gene Assay System (ThermoFisher). Results are presented as mean \pm SEM of 4 independent experiments. IC₅₀ was calculated by nonlinear regression (log[inhibitor] vs. response (three parameters)) using Prism v9.3.1 (GraphPad). (B) Cytotoxicity: Uninfected HeLa-TZM-bl cells were treated with varying concentrations of BOLD-100. Forty-eight hours post-treatment, relative cell viability was determined using CCK8 assay (Sigma) according to manufacturer's instructions. Data represent mean \pm SEM of 4 independent experiments. CC₅₀ was calculated by nonlinear regression (Sigmoidal, 4PL, X is concentration) using Prism v9.3.1 (GraphPad).

3.9.2 BOLD-100 Inhibits HAdV-C5 Replication

Adenoviruses are non-enveloped viruses with double-stranded DNA genomes that infect a wide range of vertebrates. Depending on species and type, human adenoviruses have various tropisms—most commonly, the respiratory tract, gut, and eye are targeted¹⁵³. Human adenovirus serotype 5 (HAdV-C5) belongs to Species C, which are mainly associated with respiratory disease¹⁵³. We asked whether BOLD-100 would inhibit the production of infectious HAdV-C5 in cell culture. A549 human lung carcinoma cells were infected with HAdV-C5 at MOI = 1 and treated with or without varying concentrations of BOLD-100. At 48 hours post-infection, cells were harvested and viral titres were determined by plaque assay. BOLD-100 treatment yielded a dose-dependent inhibition of HAdV-C5 replication, with a statistically significant reduction in viral load detected at concentrations of 50 μ M BOLD-100 and above ($P < 0.001$, One-way ANOVA & Holm-Šidák's multiple comparisons test) (Fig. 20A). At 200 μ M BOLD-100, this effect corresponded to a 0.6- \log_{10} reduction in viral titre. The CC_{50} of BOLD-100 alone in A549 cells under assay conditions was 396.4 μ M (Fig. 20B).

A



B

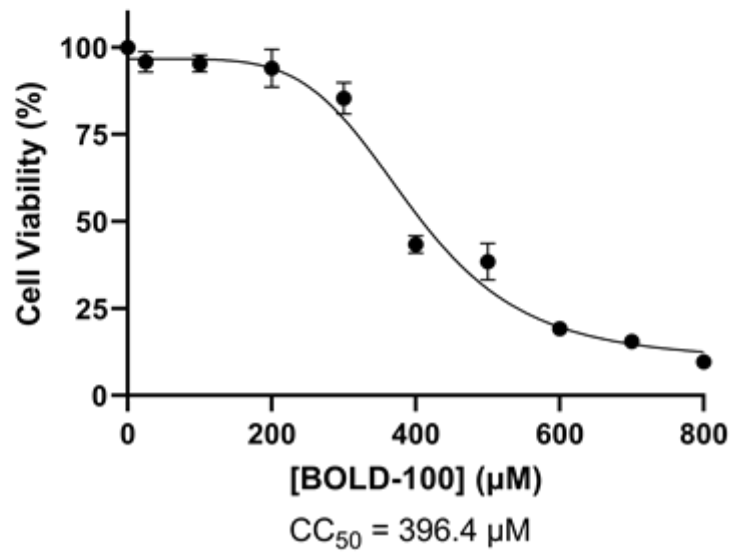


Figure 20: Inhibition of infectious HAdV-C5 by BOLD-100. (A) A549 cells in 12-well plates were infected with HAdV-C5 (MOI 1) for 1 hour. Following adsorption period, the virus inoculum was removed and fresh media containing BOLD-100 was added. Forty-eight hours post-infection, cells were collected from each well, resuspended in PBS, and subjected to 3 freeze-thaw cycles to liberate virus. Harvested virus was quantified by plaque assay on A549 cells. Data are presented as mean \pm SEM. One-way ANOVA followed by Holm-Šídák's multiple comparisons tests. *, $P < 0.05$. **, $P < 0.01$. ***, $P < 0.001$; $n = 4$. Statistical differences are indicated relative to infected cells treated with diluent alone. (B) Cytotoxicity: Uninfected A549 cells were treated with varying concentrations of BOLD-100. Forty-eight hours post-treatment, relative cell viability was determined using CCK8 assay (Sigma) according to manufacturer's instructions. Data represent mean \pm SEM of 4 independent experiments. CC_{50} was calculated by nonlinear regression (Sigmoidal, 4PL, X is concentration) using Prism v9.3.1 (GraphPad).

4 Chapter 4: Discussion

The COVID-19 pandemic prompted an unprecedented effort to discover and repurpose therapeutics for treatment of COVID-19. In this study, we identify BOLD-100 as a novel antiviral agent that inhibits SARS-CoV-2 replication in addition to virus-induced cytopathogenicity and transcriptional effects. BOLD-100 retained antiviral efficacy in major SARS-CoV-2 variants of concern. We determined the MTD of BOLD-100 in Syrian hamsters to be 15 mg/kg, and established a hamster model to evaluate the therapeutic potential of BOLD-100 against COVID-19. Intravenous BOLD-100 treatment did not significantly ameliorate viral load or lung pathology in infected hamsters, irrespective of time of administration. Finally, we determined that BOLD-100 inhibits replication of HIV-1 and HAdV-C5, indicating potential for broad-spectrum antiviral activity.

The cytopathic effects (CPE) induced by SARS-CoV-2 infection in various cell lines are mainly attributable to apoptosis of infected cells and formation of syncytia by the interaction of viral S protein with receptors on adjacent cells^{16,154}. Because any compound that inhibits one or more stages of the viral life cycle—such as entry, genome replication, or egress—will affect the virus's overall ability to replicate and infect new target cells, inhibition of CPE is generally a feature of drugs with anti-SARS-CoV-2 activity. Indeed, CPE inhibition is a widely used parameter for large-scale screening of drugs for antiviral potential against SARS-CoV-2^{155–157}. In our study, it is interesting that the concentration of BOLD-100 required to inhibit CPE (Fig. 5A) is orders of magnitude less than concentrations that appreciably restrict the production of viral particles. It must first be noted that these experiments were performed in different cell lines—the CPE protection assay was conducted using Vero E6 cells, while the antiviral replication assays were conducted using 293T-ACE2 cells. Though both lines consist of kidney epithelial cells, Vero E6 originate from African green monkeys, while 293T cells are human in origin. However, cell type-specific effects notwithstanding, there are potential biological explanations for the discrepancy in IC₅₀ values between our assays. For instance, BOLD-100 may inhibit signaling cascades triggered early in the viral lifecycle that lead to apoptosis. By preventing the amplification of signaling before it reaches critical levels, a

comparatively lower dose may be required to exert therapeutic effects. This explanation would correspond with the drastically reduced transcriptional response we observed in infected cells treated with BOLD-100.

We determined that alongside inhibition of CPE, BOLD-100 inhibited the production of SARS-CoV-2 particles (Fig. 7) at concentrations well below the drug's cytotoxic range (Fig. 6). These experiments did not strictly measure production of infectious virus, but rather the total amount of virus produced, which may comprise both infectious and non-infectious particles. As a surrogate measure of viral replication, we evaluated the reduction in SARS-CoV-2 N protein and RNA levels caused by BOLD-100 treatment in infected cells. We chose to measure *N* because it is highly abundant¹⁵⁸ and is a critical factor for production of infectious virions owing to its role in packaging the viral genome⁵. Moreover, molecular tools such as antibodies and probes for qPCR are common and readily available for this gene. While it would be informative to specifically determine the reduction in infectious SARS-CoV-2 caused by BOLD-100 treatment, it is reasonable to infer that infectious virus is inhibited, given the dramatic reduction in viral protein and RNA observed. To determine the magnitude of inhibition, the antiviral assays described herein could be repeated and infectious viral load in cell supernatants could be determined by plaque assay or TCID₅₀ titration.

We observed that BOLD-100 retained antiviral activity against major SARS-CoV-2 variants of concern; the alpha and delta variants were inhibited at comparable drug levels to the ancestral strain, while the beta variant was less susceptible to BOLD-100 treatment (Fig. 8). Because it is unknown whether BOLD-100 directly interacts with viral proteins, it is difficult to predict how mutations in specific genes will impact the drug's efficacy. Nevertheless, the reduced efficacy of BOLD-100 against the SARS-CoV-2 beta variant as opposed to the ancestral strain may be due to key mutations present in the beta variant that improve replication and/or entry³⁷. Indeed, the beta variant has exhibited increased potential for entry, replication, and pathogenesis in animal models compared to earlier strains⁴¹. While this variant's enhanced replicative capabilities may contribute to the diminished effect of BOLD-100, it is unsurprising that the drug still retains a measure of efficacy against the virus. Various non-antibody-based therapeutics have consistently

retained activity against major variants of concern^{105,159}, though relative efficacies have been reported to vary slightly¹⁶⁰.

RNA Sequencing analysis revealed that SARS-CoV-2 induces a dramatic effect on the overall cellular transcriptional response, which is counteracted by BOLD-100 treatment (Fig. 10). Similar to previous studies^{66,68,69}, our results indicate an imbalanced host response to SARS-CoV-2 infection alone, in which certain IFN-induced and immune-related genes are upregulated by infection, whereas other important factors are downregulated (Fig. 11, Fig. 12).

BOLD-100 exhibited little effect on the host transcriptional profile in the absence of SARS-CoV-2 infection, while in the presence of infection, it drastically altered virus-induced transcriptional effects. Based on the parameters of our analysis, only 5 genes were differentially expressed compared to control after BOLD-100 treatment in the absence of SARS-CoV-2 infection: *DHRS2*, *ZNF439*, *KIAA1755*, *CABP4*, and *RP11-433J8.1*. *DHR2* encodes a dehydrogenase that reduces dicarbonyl compounds¹⁶¹, while *ZNF439* encodes a potential transcription factor, *KIAA1755* encodes a protein of unknown function, and *CABP4* regulates calcium and neurotransmitter levels in photoreceptor synaptic terminals¹⁶². Overall, none of the genes upregulated by BOLD-100 treatment alone exhibit obvious roles for inhibition of SARS-CoV-2.

Among the genes highly downregulated by SARS-CoV-2 infection in the absence of BOLD-100 were key players in the innate immune response. For instance, *BST2* encodes tetherin, an IFN-induced restriction factor that inhibits egress of enveloped viruses such as SARS-CoV-2¹⁶³. The antiviral proteins *IFITM1*, *IFITM2*, and *IFITM2* were also downregulated by SARS-COV-2. IFITMs have previously been shown to restrict syncytia induced by SARS-CoV-2¹⁶⁴ and other coronaviruses; the rescue of these genes by BOLD-100 treatment may contribute to the inhibition of CPE that we previously observed. *IFIT1* encodes a protein that binds viral single-stranded RNA and recruits other IFN-induced factors¹⁶⁵, while *IFI6* encodes a factor that inhibits entry of Hepatitis C virus¹⁶⁶. An especially relevant gene that was highly downregulated by SARS-CoV-2 was *TLR3*—this gene encodes a pattern recognition receptor that recognizes double-stranded

RNA, a key viral PAMP produced during the SARS-CoV-2 replication cycle, and activates antiviral signaling pathways¹⁶⁷. Overall, the propensity of BOLD-100 to inhibit SARS-CoV-2-induced transcriptional changes may partially alleviate dysregulation of the innate immune response. Moreover, the mechanism by which this effect occurs remains unknown. It may be that inhibition of the SARS-CoV-2 life cycle by BOLD-100 restricts replication at levels such that strong virus-induced signaling is unable to occur.

Nevertheless, while the transcriptional signature of SARS-CoV-2 infection was largely reversed by BOLD-100 treatment, a significant level of viral reads was still observed—after infection and drug treatment, approximately 16% of the reads detected were SARS-CoV-2 in origin (Fig. 9). Alternatively, BOLD-100 may inhibit transcription factors that become upregulated only during situations of cellular stress such as infection; as such, BOLD-100 treatment in the absence of infection would not induce overt transcriptional effects. An enhanced understanding of the steps in the viral lifecycle that are targeted by BOLD-100 would improve interpretation of these data. To this end, time-of-addition experiments in which BOLD-100 is added to SARS-CoV-2 infected cells at key timepoints in the viral life cycle would be informative.

It is possible that BOLD-100 acts to inhibit SARS-CoV-2 entry by the endosomal pathway—in this situation, the virus could become internalized into target cells but would be unable to undergo fusion at the endosomal membrane and release its genome into the cytoplasm for replication and transcription of viral proteins. In 293T-ACE2 cells, viral entry largely occurs by this route⁶. Inhibitors of SARS-CoV-2 endosomal entry generally work by inhibiting the host cathepsin proteases that facilitate fusion between the viral envelope and endosomal membrane¹⁶⁸. Cathepsins may be directly inhibited by saturation of their active site with inhibitors that mimic substrates, or they may be indirectly inhibited by therapeutics that raise pH levels in the endosome, such as chloroquine^{6,169}. Because these cathepsin proteases require low pH for optimal activity, endosomal acidification inhibitors prevent key cleavage steps in the viral life cycle¹⁷⁰. To determine whether BOLD-100 inhibits SARS-CoV-2 membrane fusion in endosomes, future studies could infect cells with fluorescent SARS-CoV-2 and treat them with BOLD-100. Subsequently, the cellular distribution of virus could be assessed, and

immunofluorescent probes directed against key endosomal markers could be analyzed for co-localization with SARS-CoV-2.

Another potential mechanism by which BOLD-100 inhibits SARS-CoV-2 replication is by directly interfering with the function of one or more viral proteins. BOLD-100 has been predicted to localize to ribosomal proteins as a major target in HCT116 colon carcinoma cells¹²⁵. In this niche, it is possible that the drug interferes with binding of ribosomes by SARS-CoV-2 nsp1, an interaction that promotes translation of viral mRNAs^{24,25,171}. To explore this hypothesis, a co-immunoprecipitation experiment similar to that described in *Neuditschko et. al.*¹²⁵ could be conducted to determine whether BOLD-100 interacts with any SARS-CoV-2 proteins. However, this explanation does not account for the wider-spectrum antiviral activity of BOLD-100 that we observed against evolutionarily diverse viruses. Broad-spectrum antivirals that specifically target viruses rather than host factors largely fall into the category of nucleoside analogues that interfere with viral nucleic acid synthesis¹⁷². A more likely explanation is that BOLD-100 targets host factors — for instance, binding of BOLD-100 to ribosomes could potentially lead to a general attenuation of translation. To explore this possibility, global translation levels in the presence of BOLD-100 could be determined by puromycylation assay or a similar technique in which nascent polypeptides are labelled with a reporter molecule that can subsequently be quantified. Additionally, while cellular protein binding targets for BOLD-100 have been previously profiled in colon carcinoma cells¹²⁵, it would be informative to repeat these experiments in cell lines that are more physiologically relevant for SARS-CoV-2 infection. Determining protein binding targets in both the presence and absence of infection could more definitively discern elements of the mechanism of action of BOLD-100.

It is interesting that among immune-related genes, *LTA* retained high expression after infection even in the presence of BOLD-100 (Fig. 12B). This gene encodes lymphotoxin- α (also known as tumor necrosis factor- β), a secreted cytokine that mediates inflammatory and antiviral responses¹⁷³. We observed a similar pattern in the case of *KLRK1* and *FCAMR*, which were induced by SARS-CoV-2 infection and remained highly expressed after BOLD-100 treatment (Appendix A). *KLRK1* encodes NKG2D—

an activating receptor for natural killer cells and other cytotoxic cells—that recognizes “induced-self” peptides presented by virus-infected cells¹⁷⁴. *FCAMR* encodes an Fc receptor that binds immunoglobulin M and immunoglobulin A and is predicted to contribute to adaptive immune responses^{175,176}. Overall, though BOLD-100 generally reversed changes in immune-related genes induced by SARS-CoV-2, it is intriguing that certain genes important in the *in vivo* immune response are still highly expressed.

For our RNA sequencing experiments, we elected to infect cells at an MOI of 0.05 and evaluate the cellular transcriptome at 24 hours post-infection to remain consistent with similar studies reported in the literature⁶⁶. While cost concerns prevented us from evaluating additional timepoints, the cellular response to SARS-CoV-2 is highly dynamic over the course of an infection⁶⁸. Thus, our results only provide a limited picture of transcriptional changes over the entire viral life cycle and the corresponding effects of BOLD-100. We had originally intended to conduct this experiment in human lung A549-ACE2 cells, but were unable to induce robust SARS-CoV-2 infection in this cell line. While a lung cell line would have provided the most physiologically relevant results for our study, 293T-ACE2 cells are still relevant owing to renal tropism of SARS-CoV-2. Nevertheless, the characteristics of the cellular transcriptome following SARS-CoV-2 infection are variable between cell lines¹⁷⁷, and data from one cell type should not be generalized to others. These RNA sequencing experiments were performed after completion of our RT-qPCR -based antiviral assays, in which we measured inhibition of SARS-CoV-2 48 hours post-infection (Fig. 7). It would be informative to directly measure viral inhibition by RT-qPCR at 24 hours post-infection as well, given the strong effect we observed by RNA sequencing.

Since BOLD-100 had never been tested in hamsters prior to this study, we first needed to determine its toxicity profile to inform dosage in our hamster model of SARS-CoV-2 infection. We determined the MTD of BOLD-100 in Syrian hamsters to be 15 mg/kg—while this value was lower than expected based on previous studies in other rodent models¹²⁷, it is not unprecedented for compounds to exhibit highly variable toxicity among rodent species¹⁷⁸. Because no toxicity was detected in histopathologic analyses and hamsters did not exhibit signs of disease at 15 mg/kg (Fig. 13C), this value also

represents the No Observed Adverse Effect Level (NOAEL), the greatest dose of a drug that produces no adverse effects in a population. Generally speaking, the MTD should be higher than the NOAEL, since low-grade adverse effects may be considered acceptable in a drug at doses that are deemed tolerable. If we were to repeat our dose-escalation experiments in hamsters, focusing on the range of 15-30 mg/kg, we would likely obtain more accurate values for both the MTD and NOAEL.

The profound renal toxicity observed coupled with a comparative lack of pathology in liver sections indicates that BOLD-100 may primarily accumulate in the kidneys in hamsters. If true, this would stand in contrast to the drug's biodistribution in mice, in which it accumulates to a higher degree in the liver than in the kidneys. Such a discrepancy may account for the higher toxicity overall of BOLD-100 in hamsters. Quantification of BOLD-100 in hamster organs and tissues would provide important insight into its biodistribution in this model. In future studies, Ru accumulation in each organ in Syrian hamsters should be determined by inductively coupled plasma mass spectrometry or an equivalent method to definitively characterize the drug's biodistribution. This approach would also establish the degree to which BOLD-100 accumulates in hamster lungs, where it would be relevant for inhibition of SARS-CoV-2 replication. In this study, BOLD-100 was administered intravenously to remain consistent with dosing in human clinical trials. If bioavailability in the respiratory tract is determined to be poor, a more targeted approach such as an inhaled route of administration may be warranted. This approach has previously been used to improve bioavailability of other antivirals. For instance, the influenza neuraminidase inhibitor zanamivir is administered in a dry powder format for inhalation, owing to its poor bioavailability by the oral route^{179,180}.

The results of our animal studies, while considerably limited by the number of hamsters we were able to include, do not indicate that BOLD-100 monotherapy noticeably ameliorates viral load or disease progression in our Syrian hamster model of COVID-19. None of the observed differences in median viral load in lungs or trachea reached statistical significance, which was somewhat expected given the overall variability between live animal readouts and the small number of hamsters (n=3) in each treatment

group. Nonetheless, any observed reductions in viral load were relatively modest in magnitude (Fig. 15). Moreover, hamsters treated with BOLD-100 24 hours post-infection exhibited a median increase in viral load in both lungs and trachea. While a larger-scale study would need to be conducted to confirm these trends, they raise questions about the clinical applicability of BOLD-100 in COVID-19 patients, since antivirals are generally administered after the onset of disease. These results concur with a similar study conducted by collaborators with BOLD Therapeutics. In this study, hamsters were challenged with the alpha variant of SARS-CoV-2 and treated with either intravenous or intraperitoneal BOLD-100 at a range of timepoints. Similarly, no significant differences in lung viral load were detected between vehicle-treated control hamsters and those treated with BOLD-100, irrespective of time or route of administration (private communication, Dr. Tran, National Research Council of Canada). Likewise, BOLD-100 was recently tested in the K18-hACE2 mouse model of COVID-19, which is characterized by severe clinical disease and weight loss¹⁸¹. This study did not evaluate viral load or histopathological features, but rather the effect of BOLD-100 on mean survival time following SARS-CoV-2 infection; mice were euthanized upon reaching 20% weight loss. In this model, intravenous BOLD-100 did not confer a protective effect, though intraperitoneal BOLD-100 appeared to provide a small survival benefit of 1-2 days (private communication, Dr. Aguilar-Carreno, Cornell University).

Our animal studies were limited by several factors—as previously stated, our small sample size, which was restricted by cost, was the principal impediment. Moreover, our study exclusively made use of male hamsters, which was largely a consequence of our small overall sample size. Male and female hamsters differ biologically in terms of the response to SARS-CoV-2 infection—in general, males exhibit more severe clinical disease and impaired viral clearance compared to females. Future studies with larger cohorts of hamsters should incorporate equal numbers of males and females to more comprehensively assess drug effects. Likewise, we used juvenile hamsters of 4–6 weeks old to remain consistent with the majority of studies reported in the literature^{83,85,86}. As previously discussed, aged hamsters exhibit more severe clinical disease than do juvenile hamsters⁸⁴. Owing to the absence of overt clinical signs of disease in our experiments, we were unable to determine whether BOLD-100 reduced symptoms such as weight loss and

respiratory difficulties. Since these features are present in aged hamsters infected with SARS-CoV-2⁸⁴, it may be interesting to use older hamsters in future experiments to assess the role of BOLD-100 in ameliorating clinical disease in this model. Furthermore, we reported viral load in the left lung lobe or trachea for each animal. Ideally, this value would be reported in terms of viral load per gram of organ tissue. However, we were unable to import a scale with sufficient precision into the BSL-3 facility in time to properly weigh organ tissues before homogenization. The lack of normalization of viral load data based on organ weight may account for some of the observed differences. However, other studies evaluating BOLD-100 in COVID-19 hamster models did normalize their data by organ weight, and yet did not observe a significant protective effect.

For histopathological analysis, we compiled all findings and summaries provided by an expert pathologist, and assessed the relative abundance of lesions to evaluate the effect of BOLD-100 (Table 2, Fig. 17). We chose this approach as an initial measure for our pilot study alongside our viral load data to determine whether BOLD-100 would improve lung pathology; if a probable effect was observed, more quantitative measures would be used in larger-scale studies with increased sample sizes that allow us to reach statistical significance. A more robust method would be to first generate a list of pathologic features, such as congestion, bronchiolitis, and intra-alveolar hemorrhage, that have been previously reported in the literature for this model. Subsequently, an expert pathologist could assign each image a score based on the abundance of such features. Histopathology scores between treatment groups could then be compared and statistically analyzed to more quantitatively determine the role of BOLD-100 in modulating lung pathology. Alternatively, immunohistochemistry and image analysis could be used to determine the impact of BOLD-100 treatment on the accumulation of viral antigen in the lungs and other organs. Additionally, any future *in vivo* experiments should incorporate additional readouts to obtain a more complete understanding of the impact of BOLD-100 on viral replication. For instance, viral RNA shedding in the upper respiratory tract and/or feces could be determined by RT-qPCR.

We determined that the antiviral activity of BOLD-100 was not specific to SARS-CoV-2 and that the drug also inhibits HIV-1 (Fig. 18) and HAdV-C5 (Fig. 19). Though the antiviral mechanism of BOLD-100 remains largely uncharacterized, it is encouraging that it inhibits evolutionarily divergent viruses with distinct characteristics. For both viruses, we specifically determined that infectious virion production was restricted in a dose-dependent manner. We cannot directly compare the antiviral potency of BOLD-100 between these viruses, as we used different methodology for each. In the case of HAdV-C5, we tested increasing concentrations of BOLD-100 up to 200 μM , at which we observed only a modest 0.6- \log_{10} reduction in viral load. Given that the CC_{50} of BOLD-100 in A549 cells was calculated to be 396.4 μM , it may be worthwhile to evaluate concentrations of BOLD-100 higher than 200 μM against HAdV-C5. Additionally, evaluation of BOLD-100 against a wider panel of diverse viruses will provide further insight into its utility as a broad-acting antiviral. Identification of the viruses that BOLD-100 does or does not inhibit may also help elucidate the specific factors or pathways targeted by the drug mechanistically.

In oncology, a promising avenue for BOLD-100 is its use in combination with existing chemotherapeutics to which resistance has developed. The potential of BOLD-100 in this context is partially due to its ability to downregulate *GRP78*, a factor associated with therapeutic resistance^{182,183}. This effect is cell-line dependent and not ubiquitous—for example, BOLD-100 does not affect *GRP78* levels in HEK 293T cells¹⁴¹, which were used for most experiments in this study. However, *GRP78* has been repeatedly shown to be an important factor for the replication and/or cellular entry of diverse viruses. Accordingly, it may be worthwhile to evaluate BOLD-100 in combination with existing antivirals to take advantage of possible synergisms and determine its potential to alleviate drug resistance.

In sum, we have described the antiviral potential of the ruthenium-based small molecule BOLD-100 against SARS-CoV-2 and other viruses. We used a variety of molecular techniques to show that SARS-CoV-2 replication and cytopathic effects are inhibited in a dose-dependent manner by BOLD-100. Moreover, we showed that BOLD-100 largely reverses the transcriptional signature of SARS-CoV-2 infection in cell culture. We

evaluated the effects of the drug in a hamster model of COVID-19, finding that intravenous BOLD-100 does not significantly ameliorate viral load or clinical disease. However, this model may benefit from an altered route of drug administration. Finally, we determined that BOLD-100 inhibits the production of infectious HIV-1 and HAdV-C5. Overall, though refinements are required to our animal model, it is encouraging to see a clinical-stage chemotherapeutic with potential for broad-spectrum antiviral activity. Identification of novel antiviral therapeutics will be critical for use in vulnerable patients and to alleviate the burden of current and future pandemics.

References

1. Hu, B., Guo, H., Zhou, P. & Shi, Z.-L. Characteristics of SARS-CoV-2 and COVID-19. *Nat. Rev. Microbiol.* **19**, 141–154 (2020) doi:10.1038/s41579-020-00459-7.
2. Coronaviridae Study Group of the International Committee on Taxonomy of Viruses. The species Severe acute respiratory syndrome-related coronavirus: classifying 2019-nCoV and naming it SARS-CoV-2. *Nat. Microbiol.* **5**, 536–544 (2020).
3. Chen, Y., Liu, Q. & Guo, D. Emerging coronaviruses: Genome structure, replication, and pathogenesis. *J. Med. Virol.* **92**, 418–423 (2020).
4. Zhou, P. *et al.* A pneumonia outbreak associated with a new coronavirus of probable bat origin. *Nature* **579**, 270–273 (2020).
5. Fehr, A. R. & Perlman, S. Coronaviruses: An Overview of Their Replication and Pathogenesis. *Coronaviruses* **1282**, 1–23 (2015).
6. Ou, X. *et al.* Characterization of spike glycoprotein of SARS-CoV-2 on virus entry and its immune cross-reactivity with SARS-CoV. *Nat. Commun.* **11**, 1620 (2020).
7. Rastogi, M., Pandey, N., Shukla, A. & Singh, S. K. SARS coronavirus 2: from genome to infectome. *Respir. Res.* **21**, 318 (2020).
8. V'kovski, P., Kratzel, A., Steiner, S., Stalder, H. & Thiel, V. Coronavirus biology and replication: implications for SARS-CoV-2. *Nat. Rev. Microbiol.* **19**, 155–170 (2020) doi:10.1038/s41579-020-00468-6.
9. Robson, F. *et al.* Coronavirus RNA Proofreading: Molecular Basis and Therapeutic Targeting. *Mol. Cell* **79**, 710–727 (2020).
10. Jungreis, I., Sealfon, R. & Kellis, M. SARS-CoV-2 gene content and COVID-19 mutation impact by comparing 44 Sarbecovirus genomes. *Nat. Commun.* **12**, 2642 (2021).
11. Redondo, N., Zaldívar-López, S., Garrido, J. J. & Montoya, M. SARS-CoV-2 Accessory Proteins in Viral Pathogenesis: Knowns and Unknowns. *Front. Immunol.* **12**, 708264 (2021).
12. Michel, C. J., Mayer, C., Poch, O. & Thompson, J. D. Characterization of accessory genes in coronavirus genomes. *Virol. J.* **17**, 131 (2020).
13. SARS-CoV-2 Orf6 hijacks Nup98 to block STAT nuclear import and antagonize interferon signaling. *PNAS* **117**, 28344–28354 (2020).

14. Timilsina, U., Umthong, S., Ivey, E. B., Waxman, B. & Stavrou, S. SARS-CoV-2 ORF7a potently inhibits the antiviral effect of the host factor SERINC5. *Nat. Commun.* **13**, 2935 (2022).
15. Zhang, Q. *et al.* Molecular mechanism of interaction between SARS-CoV-2 and host cells and interventional therapy. *Signal Transduct. Target. Ther.* **6**, 1–19 (2021).
16. Rajah, M. M., Bernier, A., Buchrieser, J. & Schwartz, O. The Mechanism and Consequences of SARS-CoV-2 Spike-Mediated Fusion and Syncytia Formation. *J. Mol. Biol.* **434**, 167280 (2022).
17. Tang, T., Bidon, M., Jaimes, J. A., Whittaker, G. R. & Daniel, S. Coronavirus membrane fusion mechanism offers a potential target for antiviral development. *Antiviral Res.* **178**, 104792 (2020).
18. Papa, G. *et al.* Furin cleavage of SARS-CoV-2 Spike promotes but is not essential for infection and cell-cell fusion. *PLOS Pathog.* **17**, e1009246 (2021).
19. Wu, Y. & Zhao, S. Furin cleavage sites naturally occur in coronaviruses. *Stem Cell Res.* **50**, 102115 (2021).
20. Peacock, T. P. *et al.* The furin cleavage site in the SARS-CoV-2 spike protein is required for transmission in ferrets. *Nat. Microbiol.* **6**, 899–909 (2021).
21. Johnson, B. A. *et al.* Loss of furin cleavage site attenuates SARS-CoV-2 pathogenesis. *Nature* **591**, 293–299 (2021).
22. Pohl, M. O. *et al.* SARS-CoV-2 variants reveal features critical for replication in primary human cells. *PLOS Biol.* **19**, e3001006 (2021).
23. Bujanic, L. *et al.* The key features of SARS-CoV-2 leader and NSP1 required for viral escape of NSP1-mediated repression. *RNA* **28**, 766–779 (2022).
24. Thoms, M. *et al.* Structural basis for translational shutdown and immune evasion by the Nsp1 protein of SARS-CoV-2. *Science* **369**, 1249–1255 (2020).
25. Vora, S. M. *et al.* Targeting stem-loop 1 of the SARS-CoV-2 5' UTR to suppress viral translation and Nsp1 evasion. *Proc. Natl. Acad. Sci.* **119**, e21117198119 (2022).
26. Plante, J. A. *et al.* Spike mutation D614G alters SARS-CoV-2 fitness. *Nature* **592**, 116–121 (2021).
27. Cochin, M. *et al.* The SARS-CoV-2 Alpha variant exhibits comparable fitness to the D614G strain in a Syrian hamster model. *Commun. Biol.* **5**, 1–8 (2022).
28. Tao, K. *et al.* The biological and clinical significance of emerging SARS-CoV-2 variants. *Nat. Rev. Genet.* **22**, 757–773 (2021).

29. Khateeb, J., Li, Y. & Zhang, H. Emerging SARS-CoV-2 variants of concern and potential intervention approaches. *Crit. Care* **25**, 244 (2021).
30. Davies, N. G. *et al.* Estimated transmissibility and impact of SARS-CoV-2 lineage B.1.1.7 in England. *Science* **372**, eabg3055 (2021).
31. Volz, E. *et al.* Assessing transmissibility of SARS-CoV-2 lineage B.1.1.7 in England. *Nature* **593**, 266–269 (2021).
32. Challen, R. *et al.* Risk of mortality in patients infected with SARS-CoV-2 variant of concern 202012/1: matched cohort study. *The BMJ* **372**, n579 (2021).
33. CMMID COVID-19 Working Group *et al.* Increased mortality in community-tested cases of SARS-CoV-2 lineage B.1.1.7. *Nature* **593**, 270–274 (2021).
34. Graham, M. S. *et al.* Changes in symptomatology, reinfection, and transmissibility associated with the SARS-CoV-2 variant B.1.1.7: an ecological study. *Lancet Public Health* **6**, e335–e345 (2021).
35. Wang, P. *et al.* Antibody resistance of SARS-CoV-2 variants B.1.351 and B.1.1.7. *Nature* **593**, 130–135 (2021).
36. Muik, A. *et al.* Neutralization of SARS-CoV-2 lineage B.1.1.7 pseudovirus by BNT162b2 vaccine-elicited human sera. *Science* **371**, 1152–1153 (2021).
37. Tegally, H. *et al.* Detection of a SARS-CoV-2 variant of concern in South Africa. *Nature* **592**, 438–443 (2021).
38. Luan, B., Wang, H. & Huynh, T. Enhanced binding of the N501Y-mutated SARS-CoV-2 spike protein to the human ACE2 receptor: insights from molecular dynamics simulations. *Febs Lett.* **595**, 1454–1461 (2021).
39. Boehm, E. *et al.* Novel SARS-CoV-2 variants: the pandemics within the pandemic. *Clin. Microbiol. Infect.* **27**, 1109–1117 (2021).
40. Zhou, D. *et al.* Evidence of escape of SARS-CoV-2 variant B.1.351 from natural and vaccine-induced sera. *Cell* **184**, 2348–2361.e6 (2021).
41. Pyke, A. T. *et al.* Replication Kinetics of B.1.351 and B.1.1.7 SARS-CoV-2 Variants of Concern Including Assessment of a B.1.1.7 Mutant Carrying a Defective ORF7a Gene. *Viruses* **13**, 1087 (2021).
42. Garcia-Beltran, W. F. *et al.* Multiple SARS-CoV-2 variants escape neutralization by vaccine-induced humoral immunity. *Cell* **184**, 2372–2383.e9 (2021).
43. Li, Q. *et al.* SARS-CoV-2 501Y.V2 variants lack higher infectivity but do have immune escape. *Cell* **184**, 2362–2371.e9 (2021).

44. Hirabara, S. M. *et al.* SARS-COV-2 Variants: Differences and Potential of Immune Evasion. *Front. Cell. Infect. Microbiol.* **11**, 781429 (2022).
45. Cherian, S. *et al.* SARS-CoV-2 Spike Mutations, L452R, T478K, E484Q and P681R, in the Second Wave of COVID-19 in Maharashtra, India. *Microorganisms* **9**, 1542 (2021).
46. Liu, C. *et al.* Reduced neutralization of SARS-CoV-2 B.1.617 by vaccine and convalescent serum. *Cell* **184**, 4220–4236.e13 (2021).
47. Ong, S. W. X. *et al.* Clinical and Virological Features of Severe Acute Respiratory Syndrome Coronavirus 2 (SARS-CoV-2) Variants of Concern: A Retrospective Cohort Study Comparing B.1.1.7 (Alpha), B.1.351 (Beta), and B.1.617.2 (Delta). *Clin. Infect. Dis. Off. Publ. Infect. Dis. Soc. Am.* **75**, e1128–e1136 (2022).
48. Liu, Y. & Rocklöv, J. The reproductive number of the Delta variant of SARS-CoV-2 is far higher compared to the ancestral SARS-CoV-2 virus. *J. Travel Med.* **28**, taab124 (2021).
49. Sheikh, A., McMenamin, J., Taylor, B. & Robertson, C. SARS-CoV-2 Delta VOC in Scotland: demographics, risk of hospital admission, and vaccine effectiveness. *The Lancet* **397**, 2461–2462 (2021).
50. Chen, N. *et al.* Epidemiological and clinical characteristics of 99 cases of 2019 novel coronavirus pneumonia in Wuhan, China: a descriptive study. *The Lancet* **395**, 507–513 (2020).
51. Puelles, V. G. *et al.* Multiorgan and Renal Tropism of SARS-CoV-2. *N. Engl. J. Med.* **383**, 590–592 (2020).
52. Jansen, J. *et al.* SARS-CoV-2 infects the human kidney and drives fibrosis in kidney organoids. *Cell Stem Cell* **29**, 217–231 (2021).
53. Gabarre, P. *et al.* Acute kidney injury in critically ill patients with COVID-19. *Intensive Care Med.* **46**, 1339–1348 (2020).
54. Dolhnikoff, M. *et al.* SARS-CoV-2 in cardiac tissue of a child with COVID-19-related multisystem inflammatory syndrome. *Lancet Child Adolesc. Health* **4**, 790–794 (2020).
55. Li, M.-Y., Li, L., Zhang, Y. & Wang, X.-S. Expression of the SARS-CoV-2 cell receptor gene ACE2 in a wide variety of human tissues. *Infect. Dis. Poverty* **9**, 45 (2020).
56. Gupta, A. *et al.* Extrapulmonary manifestations of COVID-19. *Nat. Med.* **26**, 1017–1032 (2020).

57. Paterson, R. W. *et al.* The emerging spectrum of COVID-19 neurology: clinical, radiological and laboratory findings. *Brain* **143**, 3104–3120 (2020).
58. Nalbandian, A. *et al.* Post-acute COVID-19 syndrome. *Nat. Med.* **27**, 601–615 (2021).
59. Cevik, M., Kuppalli, K., Kindrachuk, J. & Peiris, M. Virology, transmission, and pathogenesis of SARS-CoV-2. *BMJ* **371**, m3862 (2020).
60. Park, M., Cook, A. R., Lim, J. T., Sun, Y. & Dickens, B. L. A Systematic Review of COVID-19 Epidemiology Based on Current Evidence. *J. Clin. Med.* **9**, 967 (2020).
61. Petersen, E. *et al.* Comparing SARS-CoV-2 with SARS-CoV and influenza pandemics. *Lancet Infect. Dis.* **20**, e238–e244 (2020).
62. Hui, K. P. Y. *et al.* Tropism, replication competence, and innate immune responses of the coronavirus SARS-CoV-2 in human respiratory tract and conjunctiva: an analysis in ex-vivo and in-vitro cultures. *Lancet Respir. Med.* **8**, 687–695 (2020).
63. Lazear, H. M., Schoggins, J. W. & Diamond, M. S. Shared and Distinct Functions of Type I and Type III Interferons. *Immunity* **50**, 907–923 (2019).
64. Mesev, E. V., LeDesma, R. A. & Ploss, A. Decoding type I and III interferon signalling during viral infection. *Nat. Microbiol.* **4**, 914–924 (2019).
65. Kim, Y.-M. & Shin, E.-C. Type I and III interferon responses in SARS-CoV-2 infection. *Exp. Mol. Med.* **53**, 750–760 (2021).
66. Blanco-Melo, D. *et al.* Imbalanced Host Response to SARS-CoV-2 Drives Development of COVID-19. *Cell* **181**, 1036-1045.e9 (2020).
67. Butler, D. *et al.* Shotgun transcriptome, spatial omics, and isothermal profiling of SARS-CoV-2 infection reveals unique host responses, viral diversification, and drug interactions. *Nat. Commun.* **12**, 1660 (2021).
68. Lieberman, N. A. P. *et al.* In vivo antiviral host transcriptional response to SARS-CoV-2 by viral load, sex, and age. *PLOS Biol.* **18**, e3000849 (2020).
69. Hoagland, D. A. *et al.* Leveraging the antiviral type I interferon system as a first line of defense against SARS-CoV-2 pathogenicity. *Immunity* **54**, 557-570.e5 (2021).
70. Liao, M. *et al.* Single-cell landscape of bronchoalveolar immune cells in patients with COVID-19. *Nat. Med.* **26**, 842–844 (2020).
71. Lucas, C. *et al.* Longitudinal analyses reveal immunological misfiring in severe COVID-19. *Nature* **584**, 463–469 (2020).

72. Seth, R. B., Sun, L. & Chen, Z. J. Antiviral innate immunity pathways. *Cell Res.* **16**, 141–147 (2006).
73. Muñoz-Fontela, C. *et al.* Animal models for COVID-19. *Nature* **586**, 509–515 (2020).
74. Wan, Y., Shang, J., Graham, R., Baric, R. S. & Li, F. Receptor Recognition by the Novel Coronavirus from Wuhan: an Analysis Based on Decade-Long Structural Studies of SARS Coronavirus. *J. Virol.* **94**, e00127-20 (2020).
75. Shou, S. *et al.* Animal Models for COVID-19: Hamsters, Mouse, Ferret, Mink, Tree Shrew, and Non-human Primates. *Front. Microbiol.* **12**, 626553 (2021).
76. Dinnon, K. H. *et al.* A mouse-adapted model of SARS-CoV-2 to test COVID-19 countermeasures. *Nature* **586**, 560–566 (2020).
77. Hassan, A. O. *et al.* A SARS-CoV-2 Infection Model in Mice Demonstrates Protection by Neutralizing Antibodies. *Cell* **182**, 744-753.e4 (2020).
78. Yinda, C. K. *et al.* K18-hACE2 mice develop respiratory disease resembling severe COVID-19. *PLOS Pathog.* **17**, e1009195 (2021).
79. Dong, W. *et al.* The K18-Human ACE2 Transgenic Mouse Model Recapitulates Non-severe and Severe COVID-19 in Response to an Infectious Dose of the SARS-CoV-2 Virus. *J. Virol.* **96**, e00964-21 (2022).
80. Chan, J. F.-W. *et al.* Simulation of the clinical and pathological manifestations of Coronavirus Disease 2019 (COVID-19) in golden Syrian hamster model: implications for disease pathogenesis and transmissibility. *Clin. Infect. Dis.* **71**, 2428–2446 (2020).
81. Rosenke, K. *et al.* Defining the Syrian hamster as a highly susceptible preclinical model for SARS-CoV-2 infection. *Emerg. Microbes Infect.* **9**, 2673–2684 (2020).
82. Francis, M. E. *et al.* SARS-CoV-2 infection in the Syrian hamster model causes inflammation as well as type I interferon dysregulation in both respiratory and non-respiratory tissues including the heart and kidney. *PLOS Pathog.* **17**, e1009705 (2021).
83. Gruber, A. D., Firsching, T. C., Trimpert, J. & Dietert, K. Hamster models of COVID-19 pneumonia reviewed: How human can they be? *Vet. Pathol.* **59**, 528–545 (2022).
84. Imai, M. *et al.* Syrian hamsters as a small animal model for SARS-CoV-2 infection and countermeasure development. *Proc. Natl. Acad. Sci.* **117**, 16587–16595 (2020).

85. Kaptein, S. J. F. *et al.* Favipiravir at high doses has potent antiviral activity in SARS-CoV-2–infected hamsters, whereas hydroxychloroquine lacks activity. *Proc. Natl. Acad. Sci.* **117**, 26955–26965 (2020).
86. Foo, C. S. *et al.* Ivermectin Does Not Protect against SARS-CoV-2 Infection in the Syrian Hamster Model. *Microorganisms* **10**, 633 (2022).
87. Rosenke, K. *et al.* Orally delivered MK-4482 inhibits SARS-CoV-2 replication in the Syrian hamster model. *Nat. Commun.* **12**, 2295 (2021).
88. Parekh, M., Donuru, A., Balasubramanya, R. & Kapur, S. Review of the Chest CT Differential Diagnosis of Ground-Glass Opacities in the COVID Era. *Radiology* **297**, E289–E302 (2020).
89. Dhakal, S. *et al.* Sex Differences in Lung Imaging and SARS-CoV-2 Antibody Responses in a COVID-19 Golden Syrian Hamster Model. *mBio* **12**, e0097421 (2021).
90. Osterrieder, N. *et al.* Age-Dependent Progression of SARS-CoV-2 Infection in Syrian Hamsters. *Viruses* **12**, 779 (2020).
91. Selvaraj, P. *et al.* SARS-CoV-2 infection induces protective immunity and limits transmission in Syrian hamsters. *Life Sci. Alliance* **4**, e202000886 (2021).
92. Boudewijns, R. *et al.* STAT2 signaling restricts viral dissemination but drives severe pneumonia in SARS-CoV-2 infected hamsters. *Nat. Commun.* **11**, 5838 (2020).
93. Nouailles, G. *et al.* Temporal omics analysis in Syrian hamsters unravel cellular effector responses to moderate COVID-19. *Nat. Commun.* **12**, 4869 (2021).
94. Tanni, S. E. *et al.* Pulmonary fibrosis secondary to COVID-19: a narrative review. *Expert Rev. Respir. Med.* **15**, 791–803 (2021).
95. Kim, Y.-I. *et al.* Infection and Rapid Transmission of SARS-CoV-2 in Ferrets. *Cell Host Microbe* **27**, 704-709.e2 (2020).
96. Ryan, K. A. *et al.* Dose-dependent response to infection with SARS-CoV-2 in the ferret model and evidence of protective immunity. *Nat. Commun.* **12**, 81 (2021).
97. Shi, J. *et al.* Susceptibility of ferrets, cats, dogs, and other domesticated animals to SARS–coronavirus 2. *Science* **368**, 1016–1020 (2020).
98. Ryan, K. A. *et al.* Dose-dependent response to infection with SARS-CoV-2 in the ferret model and evidence of protective immunity. *Nat. Commun.* **12**, 81 (2021).
99. Animal models for COVID-19 | Nature. <https://www.nature.com/articles/s41586-020-2787-6>.

100. Woolsey, C. *et al.* Establishment of an African green monkey model for COVID-19 and protection against re-infection. *Nat. Immunol.* **22**, 86–98 (2021).
101. Zheng, H. *et al.* Virulence and pathogenesis of SARS-CoV-2 infection in rhesus macaques: A nonhuman primate model of COVID-19 progression. *PLoS Pathog.* **16**, e1008949 (2020).
102. Rockx, B. *et al.* Comparative pathogenesis of COVID-19, MERS, and SARS in a nonhuman primate model. *Science* **368**, 1012–1015 (2020).
103. Warren, T. K. *et al.* Therapeutic efficacy of the small molecule GS-5734 against Ebola virus in rhesus monkeys. *Nature* **531**, 381–385 (2016).
104. Wang, M. *et al.* Remdesivir and chloroquine effectively inhibit the recently emerged novel coronavirus (2019-nCoV) in vitro. *Cell Res.* **30**, 269–271 (2020).
105. Vangeel, L. *et al.* Remdesivir, Molnupiravir and Nirmatrelvir remain active against SARS-CoV-2 Omicron and other variants of concern. *Antiviral Res.* **198**, 105252 (2022).
106. Williamson, B. N. *et al.* Clinical benefit of remdesivir in rhesus macaques infected with SARS-CoV-2. *Nature* **585**, 273–276 (2020).
107. Remdesivir and three other drugs for hospitalised patients with COVID-19: final results of the WHO Solidarity randomised trial and updated meta-analyses. *The Lancet* **399**, 1941–1953 (2022).
108. Owen, D. R. *et al.* An oral SARS-CoV-2 Mpro inhibitor clinical candidate for the treatment of COVID-19. *Science* **374**, 1586–1593 (2021).
109. Rock, B. M., Hengel, S. M., Rock, D. A., Wienkers, L. C. & Kunze, K. L. Characterization of ritonavir-mediated inactivation of cytochrome P450 3A4. *Mol. Pharmacol.* **86**, 665–674 (2014).
110. Hammond, J. *et al.* Oral Nirmatrelvir for High-Risk, Nonhospitalized Adults with Covid-19. *N. Engl. J. Med.* **386**, 1397–1408 (2022).
111. Wang, L. *et al.* COVID-19 rebound after Paxlovid and Molnupiravir during January-June 2022. *medRxiv* 2022.06.21.22276724 (2022)
112. Taylor, P. C. *et al.* Neutralizing monoclonal antibodies for treatment of COVID-19. *Nat. Rev. Immunol.* **21**, 382–393 (2021).
113. Chen, P. *et al.* SARS-CoV-2 Neutralizing Antibody LY-CoV555 in Outpatients with Covid-19. *N. Engl. J. Med.* **384**, 229–237 (2021).
114. Yamasoba, D. *et al.* Neutralisation sensitivity of SARS-CoV-2 omicron subvariants to therapeutic monoclonal antibodies. *Lancet Infect. Dis.* **22**, 942–943 (2022).

115. Hentzien, M., Autran, B., Piroth, L., Yazdanpanah, Y. & Calmy, A. A monoclonal antibody stands out against omicron subvariants: a call to action for a wider access to bebtelovimab. *Lancet Infect. Dis.* **22**, P1278 (2022).
116. Hartinger, C. G. *et al.* KP1019, a new redox-active anticancer agent--preclinical development and results of a clinical phase I study in tumor patients. *Chem. Biodivers.* **5**, 2140–2155 (2008).
117. Burris, H. A. *et al.* Safety and activity of IT-139, a ruthenium-based compound, in patients with advanced solid tumours: a first-in-human, open-label, dose-escalation phase I study with expansion cohort. *ESMO Open* **1**, e000154 (2016).
118. Keppler, B. K. *et al.* New Ruthenium Complexes for the Treatment of Cancer. in *Ruthenium and Other Non-Platinum Metal Complexes in Cancer Chemotherapy* (eds. Baulieu, E. *et al.*) 41–69 (Springer, 1989). doi:10.1007/978-3-642-74760-1_3.
119. Bruijninx, P. C. A. & Sadler, P. J. New trends for metal complexes with anticancer activity. *Curr. Opin. Chem. Biol.* **12**, 197–206 (2008).
120. Munteanu, A.-C. & Uivarosi, V. Ruthenium Complexes in the Fight against Pathogenic Microorganisms. An Extensive Review. *Pharmaceutics* **13**, 874 (2021).
121. Lee, S. Y., Kim, C. Y. & Nam, T.-G. Ruthenium Complexes as Anticancer Agents: A Brief History and Perspectives. *Drug Des. Devel. Ther.* **14**, 5375–5392 (2020).
122. Peti, W., Pieper, T., Sommer, M., Keppler, B. K. & Giester, G. Synthesis of Tumor-Inhibiting Complex Salts Containing the Anion trans-Tetrachlorobis(indazole)ruthenate(III) and Crystal Structure of the Tetraphenylphosphonium Salt. *Eur. J. Inorg. Chem.* **1999**, 1551–1555 (1999).
123. Alessio, E. & Messori, L. NAMI-A and KP1019/1339, Two Iconic Ruthenium Anticancer Drug Candidates Face-to-Face: A Case Story in Medicinal Inorganic Chemistry. *Mol. Basel Switz.* **24**, E1995 (2019).
124. Heffeter, P. *et al.* Intracellular protein binding patterns of the anticancer ruthenium drugs KP1019 and KP1339. *JBIC J. Biol. Inorg. Chem.* **15**, 737–748 (2010).
125. Neuditschko, B. *et al.* Interaction with Ribosomal Proteins Accompanies Stress Induction of the Anticancer Metallodrug BOLD-100/KP1339 in the Endoplasmic Reticulum. *Angew. Chem. Int. Ed.* **60**, 5063–5068 (2021).
126. Two dimensional separation schemes for investigation of the interaction of an anticancer ruthenium(III) compound with plasma proteins. *J. Anal. Chem.* **20**, 856 (2005).
127. Bytzek, A. K., Koellensperger, G., Keppler, B. K. & G. Hartinger, C. Biodistribution of the novel anticancer drug sodium trans-[tetrachloridobis(1H-

- indazole)ruthenate(III)] KP-1339/IT139 in nude BALB/c mice and implications on its mode of action. *J. Inorg. Biochem.* **160**, 250–255 (2016).
128. Lentz, F. *et al.* Pharmacokinetics of a novel anticancer ruthenium complex (KP1019, FFC14A) in a phase I dose-escalation study. *Anticancer. Drugs* **20**, 97–103 (2009).
 129. Chang, S. W. *et al.* CF₃ Derivatives of the Anticancer Ru(III) Complexes KP1019, NKP-1339, and Their Imidazole and Pyridine Analogues Show Enhanced Lipophilicity, Albumin Interactions, and Cytotoxicity. *Inorg. Chem.* **55**, 4850–4863 (2016).
 130. Bijelic, A., Theiner, S., Keppler, B. K. & Rompel, A. X-ray Structure Analysis of Indazolium trans-[Tetrachlorobis(1H-indazole)ruthenate(III)] (KP1019) Bound to Human Serum Albumin Reveals Two Ruthenium Binding Sites and Provides Insights into the Drug Binding Mechanism. *J. Med. Chem.* **59**, 5894–5903 (2016).
 131. Cetinbas, N., Webb, M. I., Dubland, J. A. & Walsby, C. J. Serum-protein interactions with anticancer Ru(III) complexes KP1019 and KP418 characterized by EPR. *JBIC J. Biol. Inorg. Chem.* **15**, 131–145 (2010).
 132. Spada, A., Emami, J., Tuszynski, J. A. & Lavasanifar, A. The Uniqueness of Albumin as a Carrier in Nanodrug Delivery. *Mol. Pharm.* **18**, 1862–1894 (2021).
 133. Groessl, M., Tsybin, Y. O., Hartinger, C. G., Keppler, B. K. & Dyson, P. J. Ruthenium versus platinum: interactions of anticancer metallodrugs with duplex oligonucleotides characterised by electrospray ionisation mass spectrometry. *J. Biol. Inorg. Chem. JBIC Publ. Soc. Biol. Inorg. Chem.* **15**, 677–688 (2010).
 134. Bold Therapeutics, Inc. *A Phase 1b Dose Escalation Study of BOLD-100 in Combination With FOLFOX Chemotherapy in Patients With Advanced Solid Tumours*. <https://clinicaltrials.gov/ct2/show/NCT04421820> (2022).
 135. Wang, M., Wey, S., Zhang, Y., Ye, R. & Lee, A. S. Role of the Unfolded Protein Response Regulator GRP78/BiP in Development, Cancer, and Neurological Disorders. *Antioxid. Redox Signal.* **11**, 2307–2316 (2009).
 136. Ibrahim, I. M., Abdelmalek, D. H. & Elfiky, A. A. GRP78: A cell's response to stress. *Life Sci.* **226**, 156–163 (2019).
 137. Lizardo, M. M. *et al.* Upregulation of Glucose-Regulated Protein 78 in Metastatic Cancer Cells Is Necessary for Lung Metastasis Progression. *Neoplasia* **18**, 699–710 (2016).
 138. Zhang, Y., Liu, R., Ni, M., Gill, P. & Lee, A. S. Cell Surface Relocalization of the Endoplasmic Reticulum Chaperone and Unfolded Protein Response Regulator GRP78/BiP. *J. Biol. Chem.* **285**, 15065–15075 (2010).

139. Tsai, Y.-L. *et al.* Characterization and Mechanism of Stress-induced Translocation of 78-Kilodalton Glucose-regulated Protein (GRP78) to the Cell Surface. *J. Biol. Chem.* **290**, 8049–8064 (2015).
140. Ha, D. P., Van Krieken, R., Carlos, A. J. & Lee, A. S. The stress-inducible molecular chaperone GRP78 as potential therapeutic target for coronavirus infection. *J. Infect.* **81**, 452–482 (2020).
141. Bakewell, S. J. *et al.* Suppression of stress induction of the 78-kilodalton glucose regulated protein (GRP78) in cancer by IT-139, an anti-tumor ruthenium small molecule inhibitor. *Oncotarget* **9**, 29698–29714 (2018).
142. Wernitznig, D. *et al.* First-in-class ruthenium anticancer drug (KP1339/IT-139) induces an immunogenic cell death signature in colorectal spheroids in vitro†. *Metallomics* **11**, 1044–1048 (2019).
143. Bakewell, S. *et al.* Inhibition of DNA Repair Pathways and Induction of ROS Are Potential Mechanisms of Action of the Small Molecule Inhibitor BOLD-100 in Breast Cancer. *Cancers* **12**, 2647 (2020).
144. Flocke, L. S., Trondl, R., Jakupec, M. A. & Keppler, B. K. Molecular mode of action of NKP-1339 - a clinically investigated ruthenium-based drug - involves ER- and ROS-related effects in colon carcinoma cell lines. *Invest. New Drugs* **34**, 261–268 (2016).
145. Cirri, D. *et al.* In Vitro Anti-SARS-CoV-2 Activity of Selected Metal Compounds and Potential Molecular Basis for Their Actions Based on Computational Study. *Biomolecules* **11**, 1858 (2021).
146. Luedtke, N. W. *et al.* Eilatin Ru(II) complexes display anti-HIV activity and enantiomeric diversity in the binding of RNA. *Chembiochem Eur. J. Chem. Biol.* **3**, 766–771 (2002).
147. Allardyce, C. S., Dyson, P. J., Ellis, D. J., Salter, P. A. & Scopelliti, R. Synthesis and characterisation of some water soluble ruthenium(II)–arene complexes and an investigation of their antibiotic and antiviral properties. *J. Organomet. Chem.* **668**, 35–42 (2003).
148. Bullen, C. K., Davis, S. L. & Looney, M. M. Quantification of Infectious SARS-CoV-2 by the 50% Tissue Culture Infectious Dose Endpoint Dilution Assay. *Methods Mol. Biol. Clifton NJ* **2452**, 131–146 (2022).
149. Deeks, S. G., Overbaugh, J., Phillips, A. & Buchbinder, S. HIV infection. *Nat. Rev. Dis. Primer* **1**, 1–22 (2015).
150. Swanstrom, R. & Coffin, J. HIV-1 Pathogenesis: The Virus. *Cold Spring Harb. Perspect. Med.* **2**, a007443 (2012).

151. Bourinbaiar, A. S. The ratio of defective HIV-1 particles to replication-competent infectious virions. *Acta Virol.* **38**, 59–61 (1994).
152. Fisher, K. *et al.* Plasma-Derived HIV-1 Virions Contain Considerable Levels of Defective Genomes. *J. Virol.* **96**, e02011-21 (2022).
153. Ghebremedhin, B. Human adenovirus: Viral pathogen with increasing importance. *Eur. J. Microbiol. Immunol.* **4**, 26–33 (2014).
154. Zhu, N. *et al.* Morphogenesis and cytopathic effect of SARS-CoV-2 infection in human airway epithelial cells. *Nat. Commun.* **11**, 3910 (2020).
155. Chen, C. Z. *et al.* Drug Repurposing Screen for Compounds Inhibiting the Cytopathic Effect of SARS-CoV-2. *Front. Pharmacol.* **11**, 592737 (2021).
156. Gorshkov, K. *et al.* The SARS-CoV-2 Cytopathic Effect Is Blocked by Lysosome Alkalinizing Small Molecules. *ACS Infect. Dis.* **7**, 1389–1408 (2021).
157. Cheng, Y.-W. *et al.* Furin Inhibitors Block SARS-CoV-2 Spike Protein Cleavage to Suppress Virus Production and Cytopathic Effects. *Cell Rep.* **33**, 108254 (2020).
158. Cubuk, J. *et al.* The SARS-CoV-2 nucleocapsid protein is dynamic, disordered, and phase separates with RNA. *Nat. Commun.* **12**, 1936 (2021).
159. Fan, Y. *et al.* SARS-CoV-2 Omicron variant: recent progress and future perspectives. *Signal Transduct. Target. Ther.* **7**, 1–11 (2022).
160. Takashita, E. *et al.* Efficacy of Antibodies and Antiviral Drugs against Omicron BA.2.12.1, BA.4, and BA.5 Subvariants. *N. Engl. J. Med.* **387**, 468–470 (2022).
161. Shafqat, N. *et al.* Hep27, a member of the short-chain dehydrogenase/reductase family, is an NADPH-dependent dicarbonyl reductase expressed in vascular endothelial tissue. *Cell. Mol. Life Sci. CMLS* **63**, 1205–1213 (2006).
162. Haeseleer, F. *et al.* Essential role of Ca²⁺-binding protein 4, a Cav1.4 channel regulator, in photoreceptor synaptic function. *Nat. Neurosci.* **7**, 1079–1087 (2004).
163. Neil, S. J. D. The Antiviral Activities of Tetherin. in *Intrinsic Immunity* (ed. Cullen, B. R.) 67–104 (Springer, 2013).
164. Rajah, M. M. *et al.* SARS-CoV-2 Alpha, Beta, and Delta variants display enhanced Spike-mediated syncytia formation. *EMBO J.* **40**, e108944 (2021).
165. Pichlmair, A. *et al.* IFIT1 is an antiviral protein that recognizes 5'-triphosphate RNA. *Nat. Immunol.* **12**, 624–630 (2011).

166. Sajid, M. *et al.* The Functional and Antiviral Activity of Interferon Alpha-Inducible IFI6 Against Hepatitis B Virus Replication and Gene Expression. *Front. Immunol.* **12**, 634937 (2021).
167. Bortolotti, D. *et al.* TLR3 and TLR7 RNA Sensor Activation during SARS-CoV-2 Infection. *Microorganisms* **9**, 1820 (2021).
168. Chitsike, L. & Duerksen-Hughes, P. Keep out! SARS-CoV-2 entry inhibitors: their role and utility as COVID-19 therapeutics. *Viol. J.* **18**, 154 (2021).
169. Zhao, H. *et al.* Cross-linking peptide and repurposed drugs inhibit both entry pathways of SARS-CoV-2. *Nat. Commun.* **12**, 1517 (2021).
170. Nabavi, S. F. *et al.* Rationale for Effective Prophylaxis Against COVID-19 Through Simultaneous Blockade of Both Endosomal and Non-Endosomal SARS-CoV-2 Entry into Host Cell. *Clin. Transl. Sci.* **14**, 431–433 (2021).
171. Tidu, A. *et al.* The viral protein NSP1 acts as a ribosome gatekeeper for shutting down host translation and fostering SARS-CoV-2 translation. *RNA* **27**, 253–264 (2021).
172. Geraghty, R. J., Aliota, M. T. & Bonnac, L. F. Broad-Spectrum Antiviral Strategies and Nucleoside Analogues. *Viruses* **13**, 667 (2021).
173. Messer, G., Weiss, E. H. & Baeuerle, P. A. Tumor necrosis factor β (TNF- β) induces binding of the NF- κ B transcription factor to a high-affinity κ B element in the TNF- β promoter. *Cytokine* **2**, 389–397 (1990).
174. Raulet, D. H. Roles of the NKG2D immunoreceptor and its ligands. *Nat. Rev. Immunol.* **3**, 781–790 (2003).
175. Shibuya, A. *et al.* Fc alpha/mu receptor mediates endocytosis of IgM-coated microbes. *Nat. Immunol.* **1**, 441–446 (2000).
176. McDonald, K. J., Cameron, A. J. M., Allen, J. M. & Jardine, A. G. Expression of Fc alpha/mu receptor by human mesangial cells: a candidate receptor for immune complex deposition in IgA nephropathy. *Biochem. Biophys. Res. Commun.* **290**, 438–442 (2002).
177. Cao, Y. *et al.* Comprehensive Comparison of RNA-Seq Data of SARS-CoV-2, SARS-CoV and MERS-CoV Infections: Alternative Entry Routes and Innate Immune Responses. *Front. Immunol.* **12**, 656433 (2021).
178. Kransler, K. M., McGarrigle, B. P. & Olson, J. R. Comparative developmental toxicity of 2,3,7,8-tetrachlorodibenzo-p-dioxin in the hamster, rat and guinea pig. *Toxicology* **229**, 214–225 (2007).

179. Cass, L. M. R., Efthymiopoulos, C. & Bye, A. Pharmacokinetics of Zanamivir After Intravenous, Oral, Inhaled or Intranasal Administration to Healthy Volunteers. *Clin. Pharmacokinet.* **36**, 1–11 (1999).
180. Boivin, G. *et al.* Rapid antiviral effect of inhaled zanamivir in the treatment of naturally occurring influenza in otherwise healthy adults. *J. Infect. Dis.* **181**, 1471–1474 (2000).
181. Winkler, E. S. *et al.* SARS-CoV-2 infection of human ACE2-transgenic mice causes severe lung inflammation and impaired function. *Nat. Immunol.* **21**, 1327–1335 (2020).
182. Fernandez, P. M. *et al.* Overexpression of the glucose-regulated stress gene GRP78 in malignant but not benign human breast lesions. *Breast Cancer Res. Treat.* **59**, 15–26 (2000).
183. Scriven, P. *et al.* Activation and clinical significance of the unfolded protein response in breast cancer. *Br. J. Cancer* **101**, 1692–1698 (2009).

Appendix A

Appendix A: Top 30 most upregulated and downregulated genes for each treatment group in RNA Sequencing analysis

This Appendix describes the top 30 most upregulated and downregulated genes identified for each treatment group in RNA Sequencing analysis (Fig. 10). Genes were filtered based on cutoffs of $|\text{Fold Change}| \geq 1.5$ and $P\text{-adjusted} \geq 0.05$.

BOLD-100

For cells treated with BOLD-100 in the absence of SARS-CoV-2, only 5 genes were identified as differentially expressed based on the cutoffs applied. All of these genes were upregulated compared to control; none were downregulated.

Upregulated Genes:

Rank	Gene	$\log_{10}(\text{Fold Change})$	$-\log_{10}(P_{\text{adjusted}})$
1	RP11-433J8.1	3.57	1.37
2	ZNF439	3.50	1.37
3	KIAA1755	3.46	1.55
4	CABP4	3.39	1.55
5	DHRS2	0.23	1.55

SARS-CoV-2

Upregulated Genes:

Rank	Gene	$\log_{10}(\text{Fold Change})$	$-\log_{10}(P_{\text{adjusted}})$
1	VAC14-AS1	5.2	3.82
2	ZNF334	5.07	2.37
3	RP11-998D10.5	5.04	2.34
4	FUT6	5.01	3.69
5	KLRK1	4.98	3.58

6	LHFPL3-AS1	4.97	3.72
7	IRGM	4.96	2.23
8	FCAMR	4.95	3.5
9	C1orf141	4.93	2.26
10	AP001331.1	4.93	3.45
11	GOLGA6B	4.92	3.4
12	PPP1R1B	4.92	3.54
13	KIAA1755	4.91	5.9
14	GPR111	4.89	3.2
15	CABP4	4.89	6.02
16	SLC30A8	4.88	2.21
17	RP11-353N4.5	4.85	1.83
18	RP11-328C8.4	4.85	2.4
19	RP11-467L20.10	4.85	3.08
20	RP11-863K10.2	4.8	2.18
21	RP11-433J8.1	4.8	5.59
22	PIGR	4.79	2.77
23	ZG16B	4.78	2.12
24	HSH2D	4.78	3.35
25	KLRC1	4.75	2.96
26	PYY	4.73	2.09
27	AC139100.3	4.71	2.96
28	TNFSF11	4.71	3.1
29	RP11-750H9.5	4.7	1.63
30	GPR26	4.7	2.06

Downregulated Genes:

Rank	Gene	$\log_{10}(\text{Fold Change})$	$-\log_{10}(\text{P}_{\text{adjusted}})$
1	RN7SL5P	-5.89	8.37
2	PDF	-4.92	8.52
3	GS1-184P14.2	-4.8	4.28
4	RPS26P8	-4.72	7.89
5	HBQ1	-4.63	7.26
6	RP11-349N19.2	-4.61	6.46
7	RPS26P31	-4.61	3.21
8	PRDX2P4	-4.59	7.19
9	H3F3BP1	-4.59	6.84
10	RP11-680G24.4	-4.5	6.65

11	RP13-444K19.1	-4.47	7.23
12	MTX1P1	-4.46	6.4
13	IDSP1	-4.44	6.76
14	EEF1A1P4	-4.44	6.45
15	COX11P1	-4.42	6.56
16	LMO3	-4.41	6.56
17	SPINK2	-4.41	6.48
18	FTH1P20	-4.4	6.62
19	VWA5A	-4.37	6.64
20	AC005884.1	-4.37	6.55
21	SLC25A5P2	-4.34	6.58
22	HSPB1P1	-4.34	6.38
23	RP11-475I24.1	-4.34	6.38
24	CTA-963H5.5	-4.34	5.88
25	ATP5G1P4	-4.33	6.66
26	PTGES	-4.32	6.67
27	MAOB	-4.32	6.48
28	CLPSL2	-4.32	6.1
29	CACNG5	-4.31	6.2
30	TMSB4XP8	-4.29	6.32

BOLD-100 + SARS-CoV-2

Upregulated Genes:

Rank	Gene	log₁₀(Fold Change)	-log₁₀(P_{adjusted})
1	GOLGA6B	3.93	1.47
2	LHFPL3-AS1	3.88	1.64
3	FUT6	3.87	1.56
4	KLRK1	3.84	1.54
5	KIAA1755	3.81	2.63
6	ZNF439	3.79	2.51
7	RP11-433J8.1	3.79	2.51
8	IFNA22P	3.77	1.35
9	PPP1R1B	3.76	1.53
10	FCAMR	3.76	1.49
11	GPR111	3.72	1.34
12	VAC14-AS1	3.71	1.53
13	CABP4	3.70	2.63
14	WEE2	3.66	1.42

15	RP11-498C9.16	3.65	1.38
16	AP001331.1	3.58	1.37
17	LTA	1.40	1.54
18	FAM230A	1.39	1.39
19	RP11-1220K2.2	1.28	3.76
20	FAM71F1	1.16	1.31
21	GGTLC3	1.16	1.36
22	RP11-196G18.3	1.06	1.91
23	MGAM	1.05	3.76
24	KIAA1683	0.92	2.52
25	CASS4	0.91	2.31
26	CD200R1	0.89	1.82
27	ZNF658B	0.86	1.52
28	MOBP	0.79	1.51
29	TG	0.75	1.61
30	ANKRD26P1	0.70	2.09

Downregulated Genes:

Rank	Gene	log₁₀(Fold Change)	-log₁₀(P_{adjusted})
1	GS1-184P14.2	-4.74	2.31
2	RP11-426L16.9	-3.41	2.20
3	RPL41P1	-0.38	1.94
4	RAB1C	-0.37	1.64
5	GRM4	-0.36	1.48
6	RPS15AP24	-0.35	1.48
7	AC074212.5	-0.34	1.57
8	CTD-2287O16.5	-0.33	1.55
9	LUC7L2	-0.32	1.34
10	SNRPF1	-0.30	1.74
11	PPP1R1A	-0.29	1.91
12	MT-ATP6	-0.27	1.56
13	SPOCK1	-0.27	1.34
14	MT-CO2	-0.27	1.73
15	MT-ND4	-0.26	1.56
16	PTP4A3	-0.26	1.38
17	MT-ND5	-0.26	1.82
18	HMG1P38	-0.25	1.50
19	MT-ND4L	-0.25	1.82

20	RP13-516M14.1	-0.25	1.53
21	TENM4	-0.23	2.09
22	YBX1P10	-0.23	1.56
23	MT-ND1	-0.23	1.42
24	IGFBP5	-0.23	1.91
25	ADRA2C	-0.23	1.52
26	ACTA2	-0.22	1.69
27	MT-CO3	-0.22	1.67
28	YBX1P1	-0.22	2.08
29	HMG2P5	-0.22	1.54
30	ATP1B2	-0.21	1.95

Appendix B

Appendix B: Copyright permissions for Figs. 1–3.

Fig. 1 is “licensed under a Creative Commons Attribution 4.0 International License, which permits use, sharing, adaptation, distribution and reproduction in any medium or format, as long as you give appropriate credit to the original author(s) and the source”.

The Creative Commons license may be viewed here:

<https://creativecommons.org/licenses/by/4.0/>

Fig. 2 and Fig. 3:

My Orders

My Orders							
Orders	Billing History	Payable Invoices					
SEARCH							
<input type="radio"/> Order Number: <input type="text"/>							
<input checked="" type="radio"/> Date Range: From <input type="text" value="28-Jul-2022"/> To <input type="text" value="28-Oct-2022"/> <input type="button" value="Go"/>							
View: <input checked="" type="checkbox"/> All <input checked="" type="checkbox"/> Saved Quotes <input checked="" type="checkbox"/> Response Required <input checked="" type="checkbox"/> Pending <input checked="" type="checkbox"/> Completed <input checked="" type="checkbox"/> Canceled <input checked="" type="checkbox"/> Denied <input checked="" type="checkbox"/> Credited							
Results: 1-2 of 2							
Date	Article Title	Publication	Type Of Use	Price	Status	Expiration Date	Order Number
26-Oct-2022	Antiviral innate immunity pathways	Cell Research	Thesis/Dissertation	0.00 CS	Completed <input checked="" type="checkbox"/>		5416550903691
25-Oct-2022	Coronavirus biology and replication: implications for SARS-CoV-2	Nature Reviews Microbiology	Thesis/Dissertation	0.00 \$	Completed <input checked="" type="checkbox"/>		5416030272135

Curriculum Vitae – Daniel Labach

ACADEMIC HISTORY:

Master of Science (M.Sc.) 2020–2022
 Microbiology and Immunology
 The University of Western Ontario, London, ON

Bachelor of Medical Sciences (B.MSc.) 2016–2020
 Microbiology and Immunology
 The University of Western Ontario, London, ON

PUBLICATIONS:

Paparisto E, Hunt NR, **Labach DS**, Coleman MD, Di Gravio EJ, Dodge MJ, Friesen NJ, Côté M, Müller A, Hoenen T, and Barr SD. Interferon-Induced HERC5 Inhibits Ebola Virus Particle Production and Is Antagonized by Ebola Glycoprotein. *Cells*. 10(9):2399. doi: 10.3390/cells10092399.

PATENTS:

McAllister ER, Pankovich J, Bazett M, Barr SD, **Labach D**. Antiviral ruthenate(iii) therapeutics. WO/2021/195763A1

HONOURS & AWARDS:

Canada Graduate Scholarship-Masters (CIHR) (\$17 500)	2021
Ontario Graduate Scholarship (\$15 000) (<i>declined</i>)	2021
Mitacs Accelerate Fellowship (\$30 000)	2021
RGE Murray Scholarship, Western University (\$10 000)	2020
FW Luney Entrance Scholarship, Western University (\$2 000)	2020
Western University Continuing Admission Scholarship (\$10 000)	2016–2020
Dean’s Honour Roll, Western University	2016–2020